AFML-TR-75-172

FG

THE CRYSTAL GROWTH AND APPLICATION OF SULFOSALT MATERIALS

376670

WESTINGHOUSE ELECTRIC CORPORATION
RESEARCH LABORATORIES
PITTSBURGH, PENNSYLVANIA 15235

NOVEMBER 1975

TECHNICAL REPORT AFML-TR-75-172
FINAL REPORT FOR PERIOD 1 JANUARY 1974 – 30 JUNE 1975

PREPARED FOR
ADVANCED RESEARCH PROJECTS AGENCY
1400 WILSON BOULEVARD
ARLINGTON, VIRGINIA 22209

AIR FORCE MATERIALS LABORATORY
AIR FORCE WRIGHT AERONAUTICAL LABORATORIES
Air Force Systems Command
Wright-Patterson Air Force Base, Ohio 45433

NOTICE

When Government drawings, specifications, or other data are used for any purpose other than in connection with a definitely related Government procurement operation, the United States Government thereby incurs no responsibility nor any obligation whatsoever; and the fact that the government may have formulated, furnished, or in any way supplied the said drawings, specifications, or other data, is not to be regarded by implication or otherwise as in any manner licensing the holder or any other person or corporation, or conveying any rights or permission to manufacture, use, or sell any patented invention that may in any way be related thereto.

This final report was submitted by Westinghouse Electric Corporation Research Laboratories, Pittsburgh, PA 15235 under Contract F33615-72-C-1976, job order number 20710001, with the Air Force Materials Laboratory, Wright-Patterson Air Force Base, OH 45433. V. L. Donlan, AFML /LPJ was the laboratory project monitor.

Particular recognition is due Dr. R. H. Hopkins for his contributions to the theoretical discussion of crystal growth problems. Substantial contributions to the acousto-optic filter studies were made by M. Gottlieb and J. J. Conroy. The technical assistance of R. P. Storrick, W. E. Gaida, J. T. Veligdan, and S. J. Pieseski was invaluable.

This report has been reviewed by the Information Office (IO) and is releasable to the National Technical Information Service (NTIS). At NTIS, it will be available to the general public, including foreign nations.

This technical report has been reviewed and approved for publication.

Vincent L. Donlan
VINCENT L. DONLAN
Project Monitor

FOR THE COMMANDER

Paul W. Elder
MAJ. PAUL W. ELDER
Chief, Laser Hardened Materials Branch
Air Force Materials Laboratory

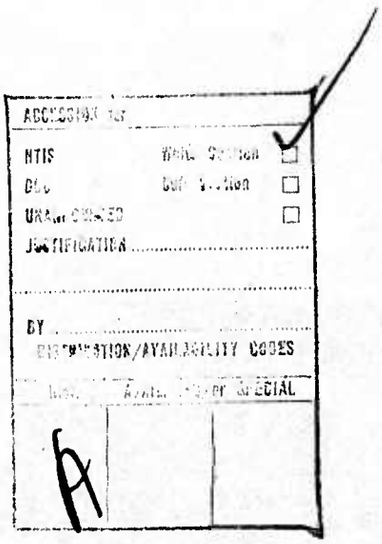

Copies of this report should not be returned unless return is required by security considerations, contractual obligations, or notice on a specific document.

AIR FORCE - 22 MARCH 1976 - 150

UNCLASSIFIED
SECURITY CLASSIFICATION OF THIS PAGE (When Date Entered)

REPORT DOCUMENTATION PAGE

READ INSTRUCTIONS BEFORE COMPLETING FORM

1. REPORT NUMBER: AFML-TR-75-172
2. GOVT ACCESSION NO.:
3. RECIPIENT'S CATALOG NUMBER:
4. TITLE (and Subtitle): THE CRYSTAL GROWTH AND APPLICATION OF SULFOSALT MATERIALS
5. TYPE OF REPORT & PERIOD COVERED: Final Report, 1 Jan 1974 – 30 Jun 1975
6. PERFORMING ORG. REPORT NUMBER: 75-9C4-PHASD-R1
7. AUTHOR(s): G. W. Roland, J. D. Feichtner, M. Rubenstein, W. E. Kramer
8. CONTRACT OR GRANT NUMBER(s): F33615-72-C-1976, ARPA Order-2071
9. PERFORMING ORGANIZATION NAME AND ADDRESS: Westinghouse Electric Corporation, Research Laboratories, 1310 Beulah Road, Pittsburgh, PA 15235
10. PROGRAM ELEMENT, PROJECT, TASK AREA & WORK UNIT NUMBERS: P.E. 61101E, W.U. No. 20710001
11. CONTROLLING OFFICE NAME AND ADDRESS: Advanced Research Projects Agency, 1400 Wilson Boulevard, Arlington, VA 22209
12. REPORT DATE: Nov 1975
13. NUMBER OF PAGES: 124
14. MONITORING AGENCY NAME & ADDRESS (if different from Controlling Office): Air Force Materials Laboratory (AFML/LPJ), Air Force Systems Command, Wright-Patterson Air Force Base, OH 45433
15. SECURITY CLASS. (of this report): UNCLASSIFIED
15a. DECLASSIFICATION/DOWNGRADING SCHEDULE: N/A

16. DISTRIBUTION STATEMENT (of this Report)

Approved for public release; distribution unlimited.

17. DISTRIBUTION STATEMENT (of the abstract entered in Block 20, if different from Report)

18. SUPPLEMENTARY NOTES

19. KEY WORDS (Continue on reverse side if necessary and identify by block number)

Thallium, arsenic, sulfur, selenium, phosphorus, crystals, growth, phase, equilibrium, sulfosalts, chalcogenides.

20. ABSTRACT (Continue on reverse side if necessary and identify by block number)

This report constitutes the Final Technical Report for Contract No. F33615-72-C-1976, Study of Phase Equilibria in the Systems Tl-As-S and Tl-As-Se -- Crystal Growth and Application of Sulfosalt Materials. As a result of this program, we now have available extensive knowledge of the ternary melting (liquidus) relations around Tl_3PS_4 and Tl_3PSe_4 in the systems Tl-P-S and Tl-P-Se. Optimized crystal growth compositions were

(over)

DD FORM 1 JAN 73 1473 EDITION OF 1 NOV 65 IS OBSOLETE

UNCLASSIFIED
SECURITY CLASSIFICATION OF THIS PAGE (When Date Entered)

376 670

20.

determined for Tl_3PS_4 and Tl_3PSe_4 and crystal growth from these compositions resulted in remarkably improved optical quality. The optical absorption was reduced to less than 10%/cm-1* Two successful device applications of new single crystal sulfosalt materials were made. In the first, and potentially most important, Tl_3AsSe_3 was used in an infrared tunable collinear acousto-optic filter in the 3-5 μm** region. Operation to 5.3 μm** was achieved, which is the longest wavelength at which any such device has yet been used. Tl_3AsS_4 was successfully used as a laser intracavity acousto-optic modulator and Q-switch with low drive power requirements. Technical difficulties believed to be associated with two-photon absorption of pump radiation or with phase matching problems prevented successful operation of a 2.1 μm**-pumped optical parametric oscillator on Tl_3AsSe_3.

* 1000 @ 1/cm.

** micrometer

TABLE OF CONTENTS

TABLE OF CONTENTS (concluded)

LIST OF ILLUSTRATIONS

LIST OF ILLUSTRATIONS (cont'd)

LIST OF ILLUSTRATIONS (cont'd)

LIST OF ILLUSTRATIONS (concluded)

LIST OF TABLES

STUDY OF PHASE EQUILIBRIA IN THE SYSTEMS Tl-As-S AND Tl-As-Se -- CRYSTAL GROWTH AND APPLICATION OF SULFOSALT MATERIALS

Final Report
Contract No. F33615-72-C-1976
ARPA Order No. 2071 Amd #2

1. INTRODUCTION

1.1 Program Objectives

This report constitutes the Final Technical Report for Contract No. F33615-72-C-1976, Study of Phase Equilibria in the Systems Tl-As-S and Tl-As-Se -- Crystal Growth and Application of Sulfosalt Materials. The reporting period covered here, January 1, 1974 to June 30, 1975, represents an 18-month extension of Contract F33615-72-C-1976, which began July 1, 1972. The results obtained during the period July 1, 1972 to December 31, 1973 were reported in Report AFML-TR-74-6. The objectives of the present program were to continue studies of sulfosalt compounds for nonlinear and acousto-optic applications. In addition to continued crystal growth and device studies of Tl_3AsSe_3, Tl_3AsS_3, and Tl_3AsS_4, phase equilibria studies in the Tl-P-S and Tl-P-Se systems were to be carried out so as to optimize crystal growth of compounds in these systems, notably Tl_3PS_4 and Tl_3PSe_4. These compounds are promising candidates for acousto-optic devices. Optical techniques were to be used to evaluate crystal quality and the optical properties of any new compounds encountered were to be investigated to determine their potential as useful optical materials.

1.2 Background Information

Increasing interest is being shown in sulfide-type materials for nonlinear optical and acousto-optic applications in the infrared

region of the wavelength spectrum. These materials have the required wide range of transparency in the infrared and many of them transmit in the 10 μm region where oxides are opaque and where high-power gas lasers operate. In addition, sulfide-type materials generally have large refractive indices and low acoustic velocities. The importance of these properties for acousto-optic interactions can be appreciated from the so-called "acousto-optic figure of merit," $M_2 = n^6 p^2/\rho v^3$, where n is the refractive index of the material at the wavelength of the incident light, p is the photoelastic coefficient (which is roughly constant but may increase in regions of strong dispersion), ρ is the density, and v the acoustic velocity in the material.

The particular sulfide-type materials of concern here are sulfosalt materials, defined as having the general formula

$$A_m B_n C_p$$

where A represents a metal, usually Ag, Cu, Hg, Pb, Tl, or Zn; B represents As, Bi, or Sb; and C represents S, Se, or Te. The first of these materials to be used in optical devices were proustite (Ag_3AsS_3)[1,2] and pyrargyrite (Ag_3SbS_3).[3] Westinghouse experience in the area of nonlinear sulfosalt materials was derived from a thorough study of the phase relations and crystal growth of proustite.[4] We began actively searching for new sulfosalt materials and synthesized several Tl-bearing sulfosalts that seemed promising for both nonlinear and acousto-optic applications. Of particular interest were the compounds Tl_3AsS_4 and Tl_3AsSe_3. Tl_3AsSe_3 had several advantages. It had the expected wide transmission range, 1.5 to 15 μm, the refractive indices were high, indicating a high figure of merit for nonlinear applications, and the birefringence was such as to allow phase matching for second-harmonic generation at 10.6 μm. It appeared that, in addition to second-harmonic generation, Tl_3AsSe_3 would also be useful as a parameteric oscillator pumped at wavelengths from 1.25 to beyond 10 μm, and especially useful as a material for a 2 μm pumped oscillator operating with outputs in

the 3 to 5 μm region. Both Tl_3AsSe_3 and Tl_3AsS_4 were shown to be useful acousto-optic crystals. The acousto-optic figure of merit was measured, by direct comparison, for Tl_3AsSe_3 at λ = 3.39 μm, relative to fused silica at λ = 0.6328 μm. The relative figure of merit was measured as 955. This figure of merit is about twice as large as the figure of merit for germanium, one of the materials presently being used in acousto-optic devices in the infrared region of the spectrum. Likewise, measurements of the figure of merit for Tl_3AsS_4 gave exceptionally high values at 0.6328 μm, higher than any other known material. It was also evident, however, that the crystal growth of these new materials would be difficult to optimize without a thorough knowledge of the melting relations in the applicable chemical systems.

Part I of ARPA-sponsored Contract F33615-72-C-1976 (effective dates July 1, 1972 to December 31, 1973) was granted with the aim of determining the phase equilibria in the systems Tl-As-S and Tl-As-Se and a portion of the quaternary system Tl-As-S-Se so as to optimize crystal growth of compounds in these systems, notably Tl_3AsS_3, Tl_3AsS_4, and Tl_3AsSe_3, and to study the optical properties and uses of crystals of these compounds. As a result of this program, there became available extensive knowledge of melting relations in the systems Tl-As-S and Tl-As-Se. Optimized growth compositions were determined for Tl_3AsSe_3 and Tl_3AsS_4 and crystals of improved optical quality were grown. Optical measurements were performed that confirmed the device potential of these compounds. Crystals of Tl_3AsS_3 and Tl_3AsSe_4 were obtained showing considerable improvement over early growth efforts. These studies were completely described in Final Technical Report AFML-TR-74-6, and published in the literature (a copy of the paper is attached to this report as Appendix A).

The present program, Part II of Contract F33615-72-C-1976 (effective dates January 1, 1974 to June 30, 1975), was proposed to continue studies of device applications of the Tl-As-S-Se crystals, and to investigate the phase relations of a new series of potentially useful thallium-phosphorus compounds. The device studies were to concentrate on the nonlinear properties of Tl_3AsS_3 and Tl_3AsSe_3, in particular the

demonstration of optical parametric oscillation in Tl_3AsSe_3. The data accumulated to that point indicated that Tl_3AsSe_3 should be exceptionally useful as a tunable oscillator for the 3 to 5 μm wavelength region. Crystals of Tl_3AsS_3 (grown from optimized growth compositions) were to be studied to determine its advantages, if any, over Tl_3AsSe_3. Studies of new materials were to focus on compounds in the Tl-P-S-Se system, their melting relations, crystal chemistry, optical properties, and crystal growth. Particular compounds of interest are Tl_3PS_4 and Tl_3PSe_4, which were identified in previous Westinghouse studies[5,6] as useful acousto-optic (but not nonlinear optical) materials. The present report describes the results and gives the conclusions of Part II of the study.

1.3 General Approach

The experimental approach adopted for Part II was the same as that used successfully in Part I. Approximately two thirds of the study was devoted to determining the melting relations of Tl_3PS_4 and Tl_3PSe_4 in the ternary systems Tl-P-S and Tl-P-Se. These phase relations were determined by quenching experiments and thermal heating and cooling curves. X-ray diffraction techniques were used to supplement these methods and to determine crystal cell dimensions and compound solid solution ranges. The data from the phase diagram study were used to understand and optimize the crystal growth of Tl_3PS_4 and Tl_3PSe_4. Concurrent with the above efforts, crystal growth and properties studies of Tl_3AsS_3 were continued as well as device studies of Tl_3AsS_4 and Tl_3AsSe_3.

1.4 Summary

As a result of this program, we now have available extensive knowledge of the ternary melting (liquidus) relations around Tl_3PS_4 and Tl_3PSe_4 in the systems Tl-P-S and Tl-P-Se. Both compounds deviate in composition from the ideal stoichiometric compositions; crystals

grown at the stoichiometric compositions were always filled with second phase inclusions and severely cracked. They were essentially opaque to light. Optimized growth compositions were determined for Tl_3PS_4 and Tl_3PSe_4 and crystal growth from these compositions resulted in remarkably improved optical quality. The optical absorption was reduced to less than $10\%/cm^{-1}$. Two successful device applications of new single crystal sulfosalt materials were made during the course of this program. In the first and potentially most important, Tl_3AsSe_3 was used in an infrared tunable collinear acousto-optic filter in the 3-5 μm region. Operation to 5.3 μm was achieved, which is the longest wavelength at which any such device has yet been used. Tl_3AsS_4 was successfully used as a laser intracavity acousto-optic modulator and Q-switch with low drive power requirements. Technical difficulties believed to be associated with two-photon absorption of pump radiation or with phase matching problems prevented successful operation of a 2.1 μm-pumped optical parametric oscillator on Tl_3AsSe_3; a few erratic oscillations were observed with Ag_3AsS_3, but reliable operation could not be achieved with that material either.

In general, new knowledge was gained concerning an important class of new optical materials, including their phase relations, crystal chemistry, detailed optical, nonlinear optical and acousto-optic properties, techniques for obtaining them in large crystals of good optical quality, and in using them in new optical devices.

ACKNOWLEDGMENTS

Particular recognition is due Dr. R. H. Hopkins for his contributions to the theoretical discussion of crystal growth problems (Sec. 5.3). Substantial contributions to the acousto-optic filter studies were made by M. Gottlieb and J. J. Conroy. The technical assistance of R. P. Storrick, W. E. Gaida, J. T. Veligdan, and S. J. Pieseski was invaluable.

2. TECHNIQUES OF PHASE DIAGRAM STUDY AND CRYSTAL GROWTH

2.1 Introduction

The experimental techniques for phase diagram determination and crystal growth used in this study are essentially the same as those previously used for the Tl-As-S-Se system and crystal growth of Tl_3AsSe_3 and Tl_3AsS_4.[7,8] Only a summary will be given in this Final Report.

2.2 Techniques of Phase Diagram Study

Two techniques have been used for phase diagram study: (1) quench-type or silica-tube experiments, and (2) thermal analysis experiments. Both types of experiments were conducted in sealed, initially-evacuated, silica glass containers, which are well-suited for reactions among sulfide-type compounds because they are inert and because they constitute sealed containers for the volatile components such as sulfur and selenium. The reactant materials for these experiments were the high-purity (99.999+) elements Tl, P, S, and Se. A great deal of care was taken to exclude oxygen contamination of the As and Tl. In the case of Tl, for example, the Tl was deoxidized in warm water with ultrasonic agitation, dried, and stored under a vacuum of better than 5×10^{-6} torr in a sealed quartz tube. This quartz tube was opened in a N_2-flow glove bag. The Tl was placed in a screw-cap preweighed bottle in the glove bag, the bottle closed, and the Tl weighed outside the glove bag. Similar precautions were taken in the case of the other elemental reactants, and in this way oxygen contamination of the reactants was kept at a minimum. The melting-point tubes were loaded in the glove bag, and sealed, again under a pressure of $< 5 \times 10^{-6}$ torr.

For quench-type experiments, reactant materials (typically 200-500 mg of Tl, P, and S or Se) were weighed in desired proportions, sealed in the containers, heated for lengths of time necessary to obtain equilibrium phase assemblages, and then chilled to room temperature. Phases were identified using standard microscope and x-ray powder diffraction techniques.

The experimental system used for the thermal analysis experiments varied little from that previously described. It consisted of a furnace, a temperature control system, and a strip chart recorder which produced a direct plot of sample temperature as a function of time (the cooling curve). The recorder was calibrated to record the desired temperature interval by means of a potentiometer. Chromel-alumel thermocouples were used throughout, and these were recalibrated after every six runs against a high-purity lead standard (melting point 227.5°C). The cooling rates we used for the thermal analysis experiments were occasionally as fast as 20°C/min, but were usually much slower, 5°C/hour. We placed more reliability on the data obtained at the slower rates. We tested the reproducibility of the system by preparing and running three duplicate samples. In no case was there a variation between the duplicates of greater than 1/2°C.

We have observed that crystallization rates are sluggish for many compositions in both the Tl-P-S and Tl-P-Se systems. This problem, undoubtedly due to the well-known glass-forming nature of many liquids in these systems, leads to unreproducible thermal data, particularly for low-temperature arrests at solidus points such as eutectic crystallizations. For this reason, we concentrated on the upper-melting or liquidus temperatures only, and tried to increase reproducibility by slow cooling rates. This emphasis on liquidus temperatures is justified since from a map of the liquidus temperature for a specific compound we can determine the maximum-melting composition -- that composition which is best for crystal growth.

2.3 Techniques of Crystal Growth

Our experience has shown that the essential features of a crystal-growth technique for congruently-melting sulfosalt materials are: (1) carefully prepared reactant material that matches the congruently-melting composition of the desired crystal as closely as possible, (2) a slow growth rate (10 to 20 mm/day), and (3) a steep (5 to 15°C/mm) temperature gradient at the solid-liquid interface in the crystal growing furnace. Growth facilities were optimized to provide the necessary steep temperature profiles and slow growth rates.

For crystal growth, portions of the prepared reactant material were sealed under about 0.8 atm pressure of pure argon into quartz "crystal-growing" tubes which contain a necked-in portion near the bottom of the tube. The neck in the tube serves exactly the same purpose as a neck in a Czochralski crystal -- to initiate single-crystal growth from a polycrystalline boule. The argon pressure in the tubes suppresses the presence of vapor during a growth run.

Figure 1 shows the quartz-tube furnaces used for crystal growth. Each furnace consisted of two heated zones separately controlled by variacs: an upper high-temperature zone and a lower low-temperature zone. The temperature gradient at the solid-liquid interface could be varied by adjusting the voltages to the two windings. As the crystal-growth tubes containing melt dropped slowly through the furnace, the melts crystallized when the temperature reaches that of the solidification (melting) point. The grown crystal was allowed to anneal at the temperature of the lower furnace (usually set at about half the melting temperature) and then cooled to room temperature over two to three days.

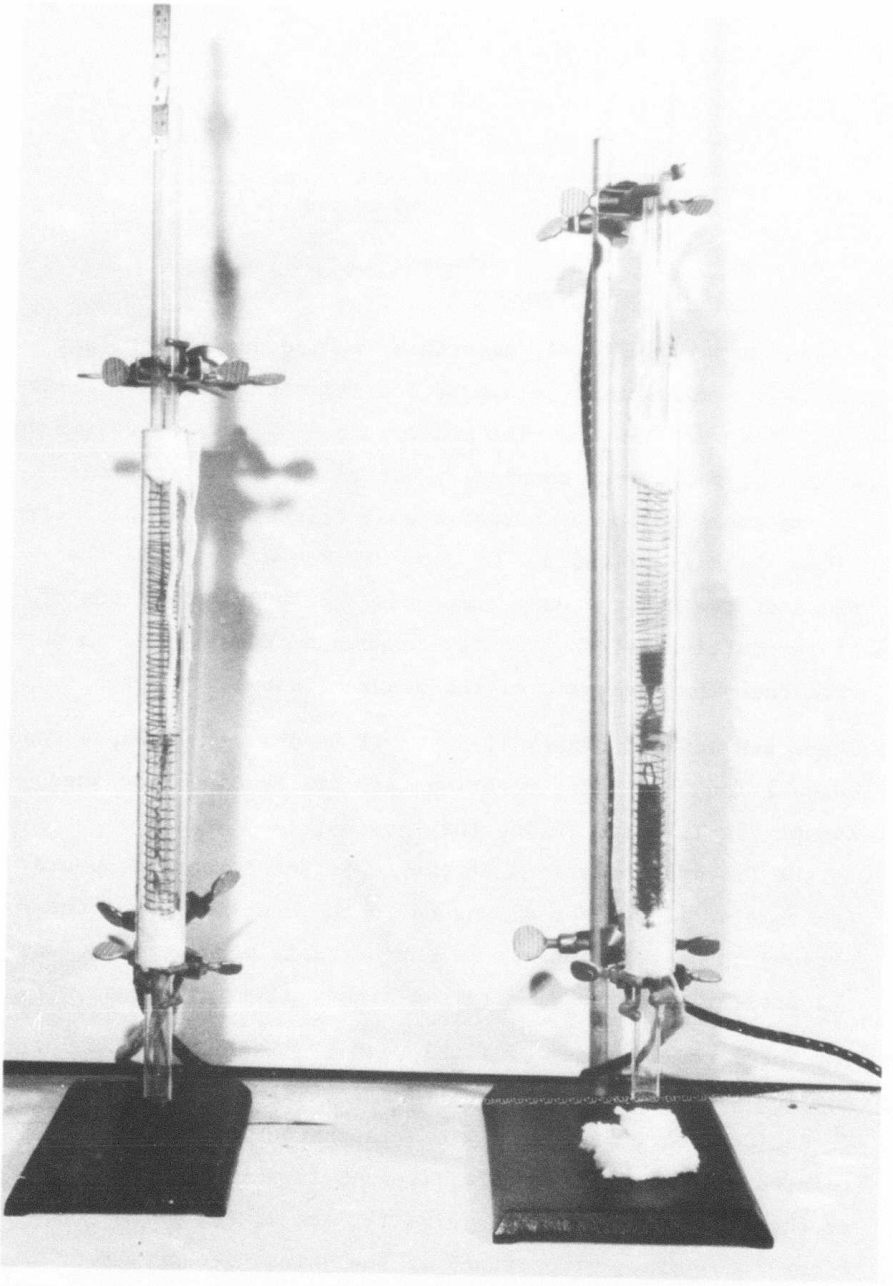

Fig. 1. Furnaces used for crystal growth.

3. COMPOSITION AND CRYSTAL DATA FOR INVESTIGATED COMPOUNDS

3.1 Composition of Ternary Compounds

The ternary sulfosalt materials studied during the last year and a half have compositions in one of four ternary systems: Tl-As-S, Tl-As-Se, Tl-P-S, or Tl-P-Se. The compositions of ternary phases in the first two of these were completely described in the previous report.[7] The three component compositional triangles for the latter two are shown in Figs. 2 and 3. On each diagram are plotted the compositions of the known binary compounds and the compositions of the ideal compositions of the ternary compounds investigated in this study. The following features of the diagrams should be noted:

- There are several binary Tl-S and Tl-Se phases[9-11] whose exact compositions and phase relations are not precisely defined. Except for Tl_2S and Tl_2Se, they are not involved in the liquidus relations of the important ternary compounds (this point is further discussed in the description of the ternary phase relations). No further data were derived from the present study to clarify the binary phase diagrams.
- The ideal compositions of Tl_3PS_4 and Tl_3PSe_4 lie at the intersection of composition joins from $Tl_2S(Se)$-$P_2S_5(Se_5)$ and from $Tl_3PS_3(Se_3)$-S(Se). This feature is characteristic of many related systems, for example, Tl-As-S in which Tl_3AsS_4 lies at the intersection of the joins Tl_2S-As_2S_5 and Tl_3AsS_3-S. Often such joins, or portions of the joins, act as pseudobinary systems in a phase diagram sense, thus simplifying the phase diagram study. The phase diagram studies reported below show,

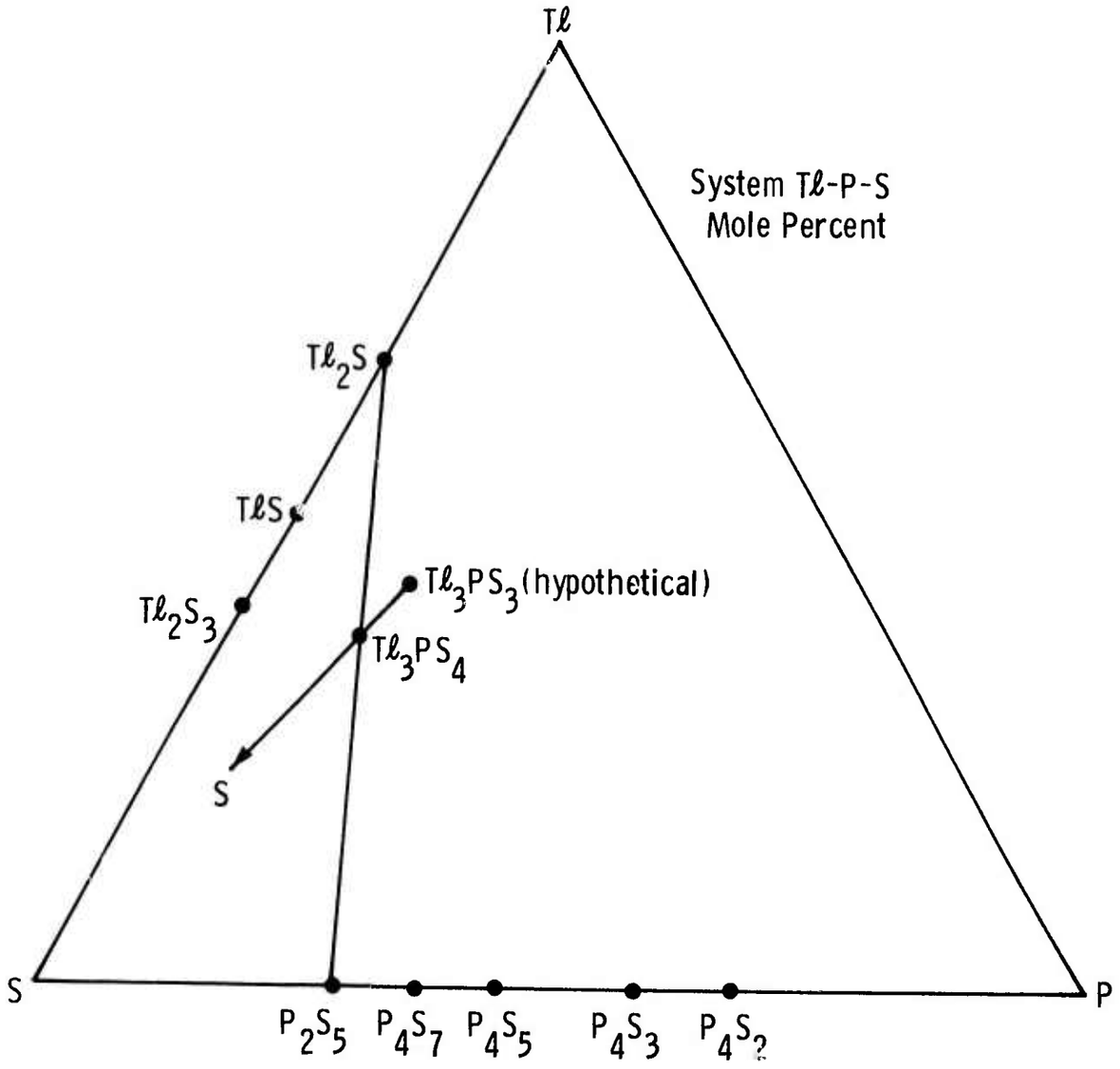

Fig. 2—Phases in the system Tℓ-P-S

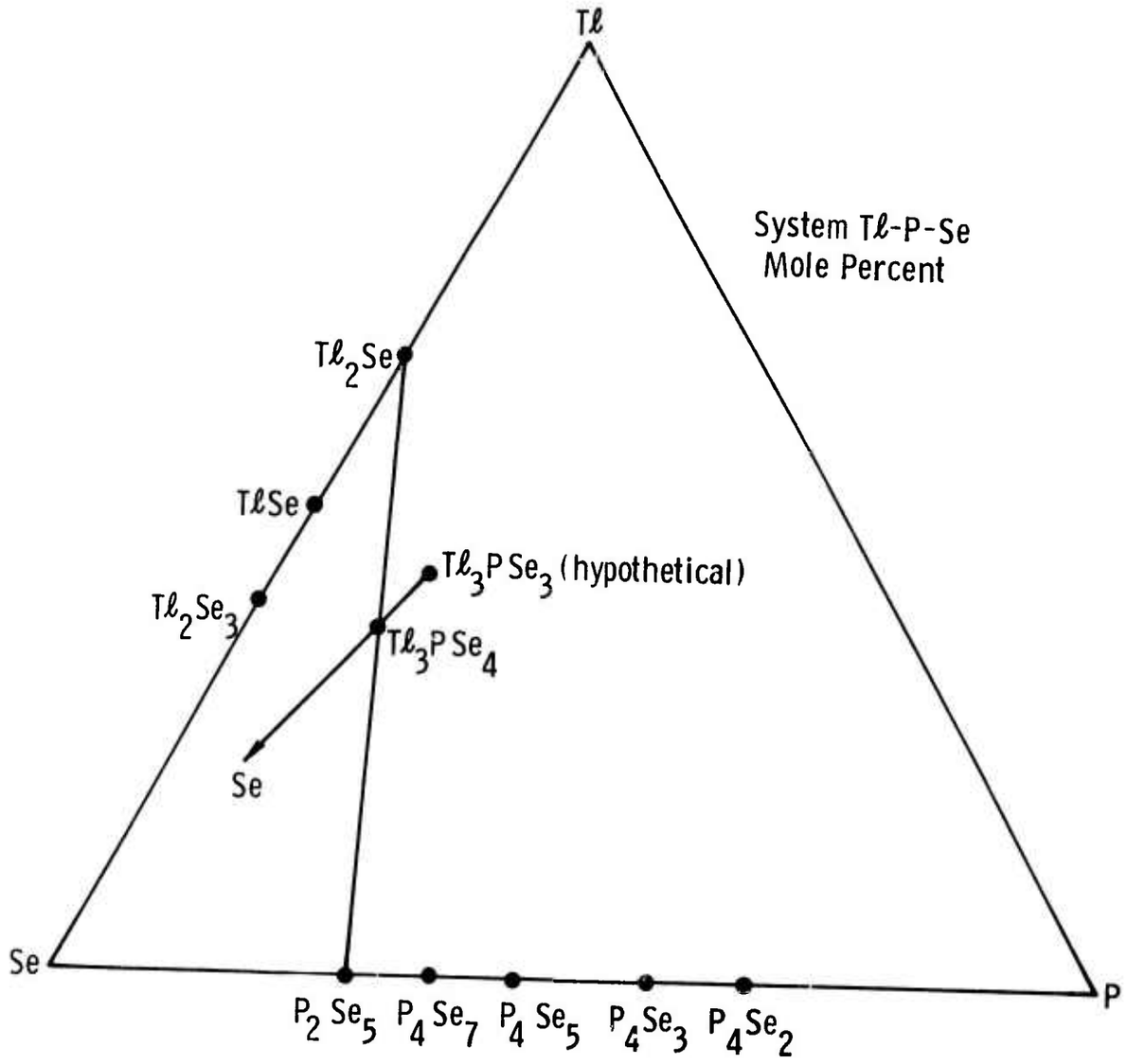

Fig. 3—Phases in the system Tℓ-P-Se

however, that the maximum-melting Tl_3PS_4 and Tl_3PSe_4 compositions deviate from the ideal stoichiometric value; nevertheless, it seems clear that both belong to the group of orthorhombic sulfosalt compounds (See Section 3.2.4) having the ideal A_3BC_4 atom ratio so that we shall use the ideal composition in a general sense.

- The compounds Tl_3PS_3 and Tl_3PSe_3 are shown in Figs. 2 and 3 as "hypothetical" because we have not been able to prepare pure phases having these compositions by quenching or slow cooling molten charges. If they exist as stable phases, then melting must be incongruent (in contrast to the congruently-melting Tl_3AsS_3 and Tl_3AsSe_3).

3.2 Crystallographic and X-Ray Data

Samples of the ternary compounds were examined by x-ray powder diffraction methods and single crystals of Tl_3AsS_3 were studied in some detail using Laue and Buerger precession camera techniques. The latter technique can provide a relatively rapid means of determining crystal symmetry (diffraction aspect) and cell dimensions. The available crystallographic and x-ray data are reported in the following sections.

3.2.1 Tl_3AsS_3

Tl_3AsS_3 was previously identified[7] as a potentially useful nonlinear optical material for second harmonic generation and optical upconversion in the infrared. This material seemed appropriate for such applications because the x-ray powder data for Tl_3AsS_3 showed sufficient similarity to those for the well-characterized Tl_3AsSe_3 so as to suggest that the two were isostructural. A considerable amount of effort was therefore devoted in the present study to obtaining the additional crystallographic data necessary for the x-ray orientation

of large Tl_3AsS_3 single crystals grown from a melt of $Tl_3AsS_{2.995}$ as described in the Final Report for Part I, AFML-TR-74-6 so that measurements of optical properties such as refractive indices and nonlinear coefficients could be made.

The first attempts to establish the crystallographic orientation of Tl_3AsS_3 crystals using the more or less routine procedures developed for Tl_3AsSe_3 met with complete failure because a unique crystal axis represented by the intersection of crystal mirror planes could not be identified. The only symmetry element identified in single crystal Laue photographs was a single mirror plane, suggesting that the crystal symmetry was monoclinic. X-ray photographs subsequently made at 10° intervals about the axis normal to the mirror plane failed to show the presence of any of the further symmetry elements, e.g., additional mirror planes, that would be required if the symmetry were higher than monoclinic.

We attempted to verify the suggested monoclinic symmetry and obtain cell dimensions by single crystal x-ray precession photographs. In this we were not successful; Tl_3AsS_3 is an extremely soft and easily deformed material and the precession photographs of crystal slices always reflected a considerable degree of strain, e.g., multiple spots, spot streaking, etc. Small crystals gathered from voids in a Tl_3AsS_3 charge solidified by slowly cooling a Tl_3AsS_3 melt also showed considerable distortion, probably developed during the cooling to room temperature.

The difficulties described above make it extremely difficult to obtain the crystallographic orientation of a crystal of Tl_3AsS_3 (indeed, the task is probably impossible without unit cell dimensions gotten from single crystal x-ray diffraction studies). We did not pursue this line of endeavor since the success of Tl_3AsS_3 as a nonlinear optical material would be extremely doubtful because of its difficult-to-use monoclinic (optically biaxial) symmetry.

3.2.2 Tl_3AsSe_3

The structure of Tl_3AsSe_3 was solved by single-crystal x-ray study in a joint effort with H. Y-P Hong and J. C. Mikkelsen, Jr., of

the Lincoln Laboratory, Massachusetts Institute of Technology.[12] The structure is rhombohedral, with space group R3m and cell parameters a = 9.870(2)Å, c = 7.094(3)Å, z = 3. A full-matrix least-squares refinement gives weighted R = 0.058. The Se atoms form equilateral triangles around Tl at 3.178 Å and around As at 2.207 Å. The structure may be described in terms of units formed from three $TlSe_3$ triangles by corner-sharing. These units share corners to produce a helical arrangement along the c axis. The triangles of $AsSe_3$ are isolated from each other.

3.2.3 Tl_3AsS_4

The single-crystal x-ray diffraction data previously obtained[7,13] for this orthorhombic material allowed us to index the x-ray powder diffraction pattern. This was accomplished by using the single-crystal values for the unit cell edges as preliminary data and improving the cell data by iterative techniques until sufficiently precise data were at hand to index the complete x-ray powder pattern. The final values for the Tl_3AsS_4 cell dimensions are $\underline{a}$ = 9.14 Å, b = 10.93 Å, c = 8.97 Å (all $\pm$ 0.02 Å). The indexed powder data are reported in Table 1.

3.2.4 Tl_3PS_4 and Tl_3PSe_4

Single crystal x-ray data for Tl_3PS_4[5] and Tl_3PSe_4[14] showed that both are orthorhombic with diffraction aspect Pc*n. The probable space group for both is Pcmn, the same as that proposed for Tl_3AsS_4. These three compounds appear isostructural, and we were able to use the indexed diffraction data for Tl_3AsS_4 as an aid to index those for Tl_3PS_4 and Tl_3PSe_4. These data are reported in Tables 2 and 3, along with the values for the cell dimensions. Crystals of all three compounds have a well developed pinacoidal {010} cleavage, which is a most useful aid in crystal orientation.

TABLE 1

X-ray powder diffraction data for Tl_3AsS_4 indexed for an orthorhombic cell, $\underline{a}$ = 9.14, $\underline{b}$ = 10.93, $\underline{c}$ = 8.97 Å. CuKα radiation, Ni-filtered, s = strong, ms = medium strong, m = medium, w = weak, vw = very weak line intensity.

hkℓ	d_{obs}	d_{calc}	I_{rel}
200	4.587	4.570	w
002	4.484	4.485	w
121	4.160	4.157	m
102	4.022	4.026	ms
211	3.819	3.816	ms
220	3.507	3.506	ms
022	3.453	3.467	m
130	3.386	3.384	ms
221	3.268	2.265	ms
122	3.246	3.242	ms
202	3.198	3.201	w
310	2.935	2.935	m
301	2.884	2.885	w
032	2.821	2.828	vs
311	2.788	2.789	m
113	2.750	2.750	w
040	2.730	2.733	m
231	2.712	2.712	w
132	2.697	2.702	m
321	2.550	2.551	ms
213	2.432	2.439	w
400	2.284	2.285	w
241	2.267	2.269	m
401	2.209	2.214	w
411	2.170	2.170	w
150	2.122	2.126	w
233	2.057	2.063	vw
421	2.049	2.052	vw
124	2.017	2.023	w
412	1.998	2.002	w
251	1.922	1.926	w
152	1.918	1.921	w
034 }	1.903	1.910	vw
422 }		1.908	vw
431	1.890	1.892	w

Additional reflections at lower d values.

TABLE 2

X-ray powder diffraction data for Tl_3PS_4 indexed for an orthorhombic cell, a = 9.04 Å, b = 10.92 Å, c = 8.78 Å. CuKα radiation, Ni-filtered, s = strong, ms = medium strong, m = medium, w = weak, vw = very weak line intensity.

hkℓ	d_{obs}	d_{calc}	I_{rel}
020	5.488	5.460	vw
200	4.529	4.520	w
002	4.413	4.390	w
121	4.152	4.126	m
102	3.949	3.960	m
211	3.771	3.771	ms
220	3.481	3.482	s
022	3.428	3.421	w
130	3.376	3.377	vs
221	3.234	3.237	m
202	3.153	3.149	m
310	2.903	2.905	m
301	2.848	2.850	w
032	2.800	2.802	s
311	2.757	2.758	w
040 } 222	2.729	2.730 2.728	ms
231	2.698	2.698	w
132	2.677	2.677	m
321	2.527	2.523	s
213	2.398	2.397	vw
400	2.260	2.260	m
223	2.243	2.240	m
401	2.187	2.189	vw
411	2.138	2.146	w
051	2.120	2.119	w
313	2.062	2.062	vw
332	2.057	2.052	vw
233	2.037	2.036	vw
421	2.032	2.032	vw
124	1.989	1.987	vw
412	1.974	1.976	vw
214 } 143	1.945	1.943 1.949	vw
251	1.917	1.919	w
152	1.911	1.911	w
034	1.881	1.880	vw
431	1.873	1.876	w
342	1.836	1.837	w

Additional reflections at lower d values.

TABLE 3

X-ray powder diffraction data for Tl_3PSe_4. Indexed for an orthorhombic cell, $\underline{a}$ = 9.32 Å, $\underline{b}$ = 11.09 Å, $\underline{c}$ = 9.09 Å. CuKα radiation, Ni-filtered, s = strong, ms = medium strong, m = medium, w = weak, vw = very weak line intensity.

hkℓ	d_{obs}	d_{calc}	I_{rel}
200	4.671	4.660	w
002	4.536	4.545	w
121	4.230	4.221	w
102	4.095	4.085	m
211	3.895	3.884	m
220	3.574	3.568	w
022	3.520	3.515	w
130	3.440	3.436	m
221	3.320	3.321	m
122	3.290	3.289	w
202	3.256	3.254	w
131	3.219	3.214	w
310	2.998	2.992	m
301	2.940	2.940	w
032	2.868	2.868	s
311	2.842	2.842	m
222	2.805	2.806	s
040	2.773	2.773	m
132	2.740	2.741	ms
140	2.661	2.657	vw
321	2.599	2.597	ms
213	2.479	2.476	vw
400	2.331	2.330	m
223	2.309	2.309	m
411	2.207	2.211	w
150	2.159	2.158	w
412	2.039	2.038	w
251	1.955	1.956	w
152	1.952	1.949	w
403	1.848	1.847	w

Additional reflections at lower d values.

4. THE MELTING RELATIONS OF Tl_3PS_4 AND Tl_3PSe_4

4.1 Introduction

In our previous studies of the crystal growth of various sulfosalt compounds,[4,7,8] we have repeatedly found that success depends in large measure on matching the crystal growth composition to the maximum-melting composition of the desired solid phase. In the case of proustite, Ag_3AsS_3, for example, this simply means minimizing the loss of volatile reactants in the crystal growth charge during preparation of the crystal growth experiment. For Tl_3AsSe_3 we found the maximum-melting composition to deviate slightly from the ideal stoichiometric composition. Thus, the best crystals were obtained from melts containing 24.62 mole % As_2Se_3 rather than 25.00 mole %, which is the ideal composition in the pseudobinary Tl_2Se-As_2Se_3 system. The preliminary crystal growth efforts made prior to the start of this program showed that there must be even greater deviations of the maximum-melting compositions of Tl_3PS_4 and Tl_3PSe_4 from ideal stoichiometric values in the Tl-P-S and Tl-P-Se systems. A significant portion of the materials effort in the present contract was devoted to the study of the appropriate melting relations in these two systems so that crystals of Tl_3PS_4 and Tl_3PSe_4 could be obtained.

The approach used to determine the melting relations of Tl_3PS_4 and Tl_3PSe_4 was similar to that previously used in the Tl-As-S and Tl-As-Se systems. The first efforts were confined to the composition joins $Tl_2S(Se)$-$P_2S_5(Se_5)$ and $Tl_3PS_3(Se_3)$-S(Se). As discussed in Chapter 2, the Tl_3PS_4 and Tl_3PSe_4 compositions lie at the intersection of these composition joins. The thermal data thus obtained could then be used to choose appropriate ternary compositions not on the joins so

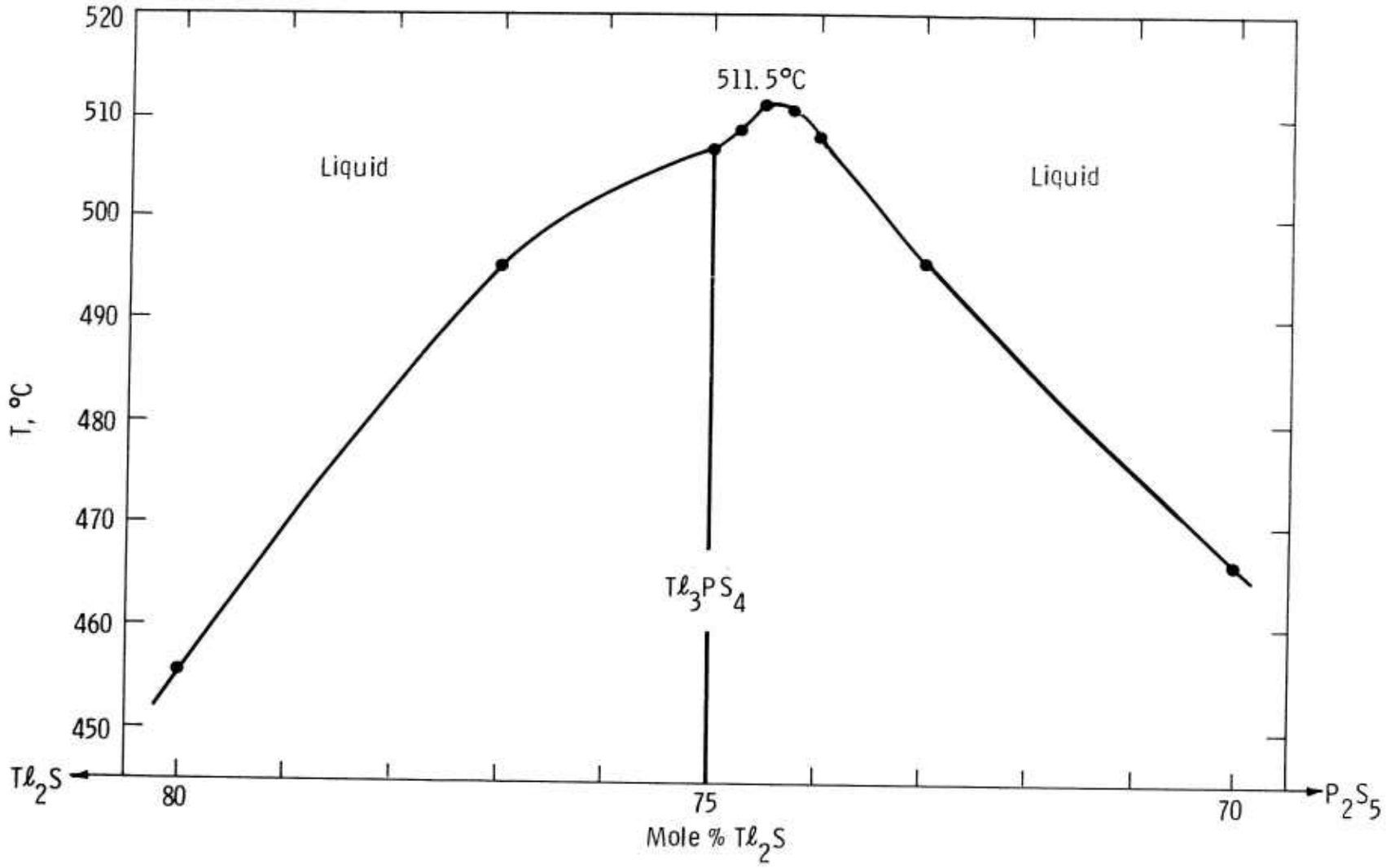

Fig. 4—The Tl_3PS_4 liquidus curve along the composition join Tl_2S-P_2S_5

that a complete picture of the liquidus surface appropriate to crystal growth was obtained. The results are described in the following sections.

4.2 Studies in the System Tl-P-S

Thermal analysis experiments along the composition join Tl_2S-P_2S_5 showed immediately that the maximum-melting Tl_3PS_4 composition was nonstoichiometric as suspected from early crystal-growth efforts. This is shown in Fig. 4 by the nonstoichiometric location of the peak in the liquidus surface at 511.5°C. Additional evidence is provided by the microstructure of quenched melts of Tl_3PS_4 composition. As shown in Fig. 5, there is an appreciable percentage of second phase, Tl_2S, present with the quench-crystallized Tl_3PS_4 in such runs.

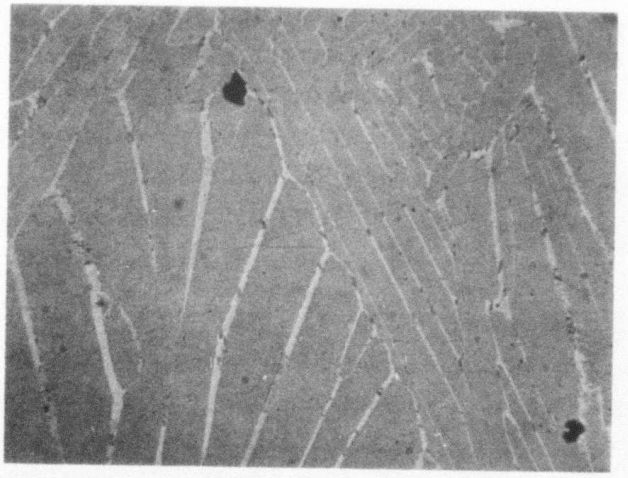

Fig. 5. Photomicrograph (reflected light) of Tl_2S second phase (light) with Tl_3PS_4 (dark) crystallized from a melt of Tl_3PS_4 composition by quenching to room temperature. X200.

We have observed another interesting feature of runs in the system Tl_2S-P_2S_5 -- the trend of the liquidus surface (either toward Tl_2S or P_2S_5) is strikingly indicated by the color of the charges. Charges which lie on the Tl_2S-side of maximum melting are black in color; those on the P_2S_5-side of maximum-melting are yellow. This is vivid when seen in color, but is evident also in black and white (Fig. 6). The color of the ground powders are, however, not significantly different, and the x-ray powder pictures of both products are the same. The color changes probably indicate the coloring effects caused by the presence of second phases which are Tl_2S-rich (black) or P_2S_5-rich (yellow).

The deviation of the maximum-melting Tl_3PS_4 composition from stoichiometry is not evident in the thermal data for the join Tl_3PS_3-S (Fig. 7). The liquidus curve shows a smooth rise on either side of the ideal composition and peaks at that composition and a temperature of 507.5°C.

The liquidus surface defined by ternary experiments is shown in Fig. 8. The maximum-melting composition can be seen from these data to be rich in P relative to Tl_3PS_4, which most probably indicates a coupled omission of Tl^+ and $S^=$ ions from the structure. The highest melting temperature observed was 514°C; the maximum-melting composition is $Tl_{37.2}P_{12.9}S_{49.9}$ within $\pm$ 0.2 mole % of each component.

After the thermal data were collected for each of the compositions shown in Fig. 8, the charge was opened and an x-ray diffraction powder pattern was obtained for the product. There is no detectable ($\pm$ 0.002 Å) charge in the unit cell dimensions we conclude that there is essentially no solid solution range to Tl_3PS_4, at least above $\sim$ 490°C. The implications of this in the crystal growth study are discussed in Chapter 5.

Tl-P-S System
Preparations of Tl_3PS_4, off Stoichiometry
$2Tl_3PS_4 \rightleftharpoons Tl_6P_2S_8 \rightleftharpoons 3Tl_2S \cdot P_2S_5$

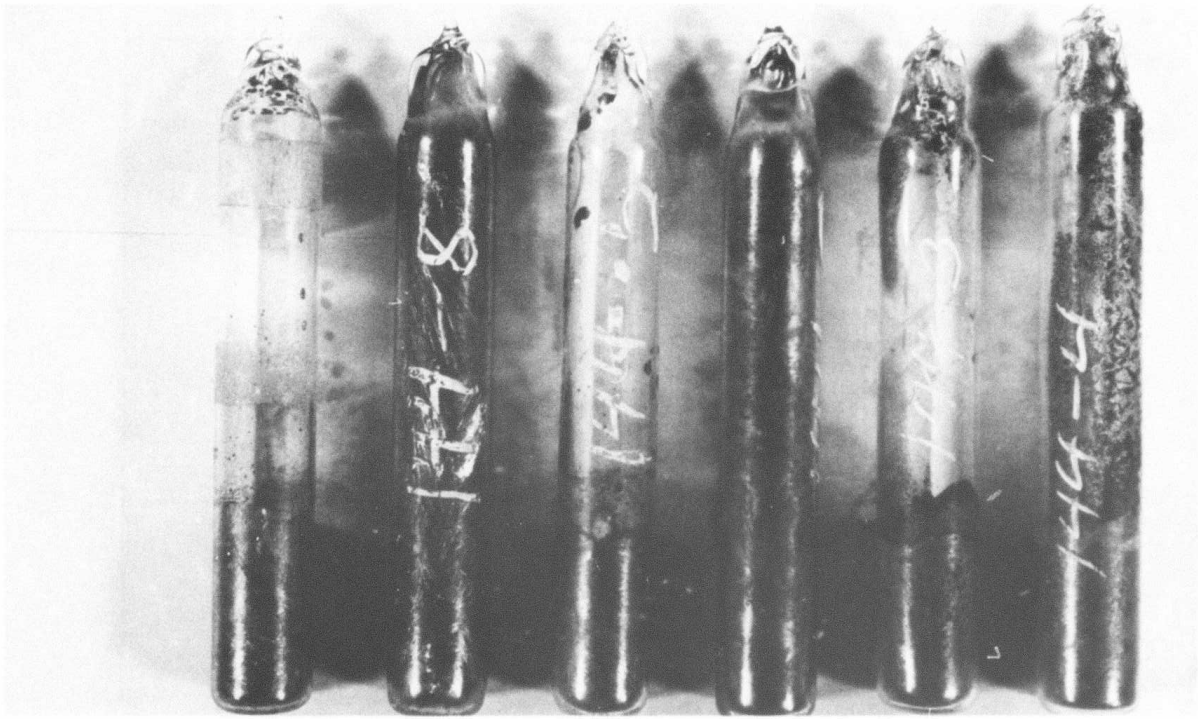

mole fraction Tl_2S	.7500	.7475	.7450	.7400	.7300	.7000
mole fraction P_2S_5	.2500	.2525	.2550	.2600	2700	.3000

Fig. 6 -- A photograph of polycrystalline Tl-P-S samples along the composition join Tl_2S-P_2S_5. The maximum-melting composition separates light from dark samples.

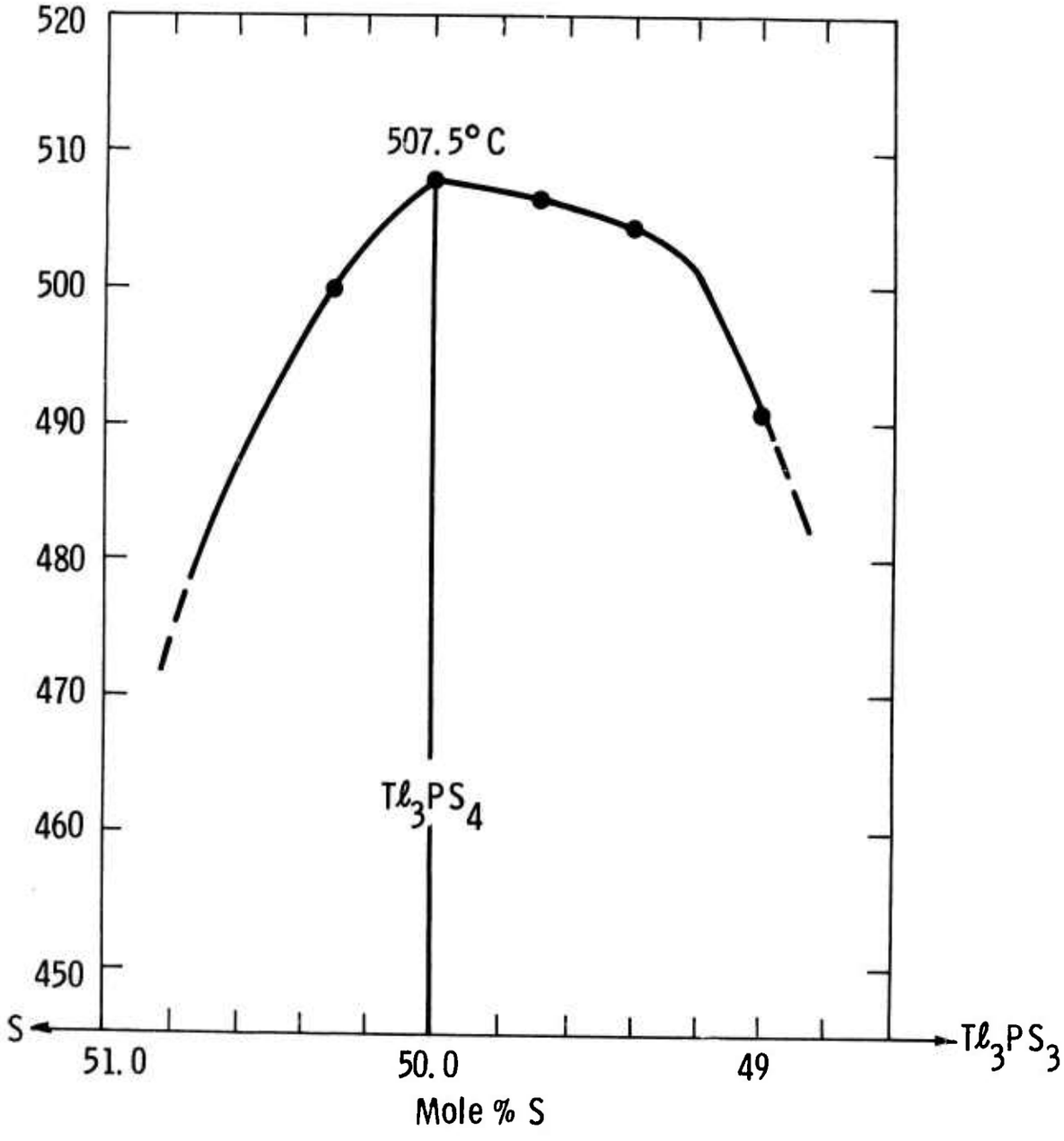

Fig. 7 –The Tl_3PS_4 liquidus curve along the composition join Tl_3PS_3-S

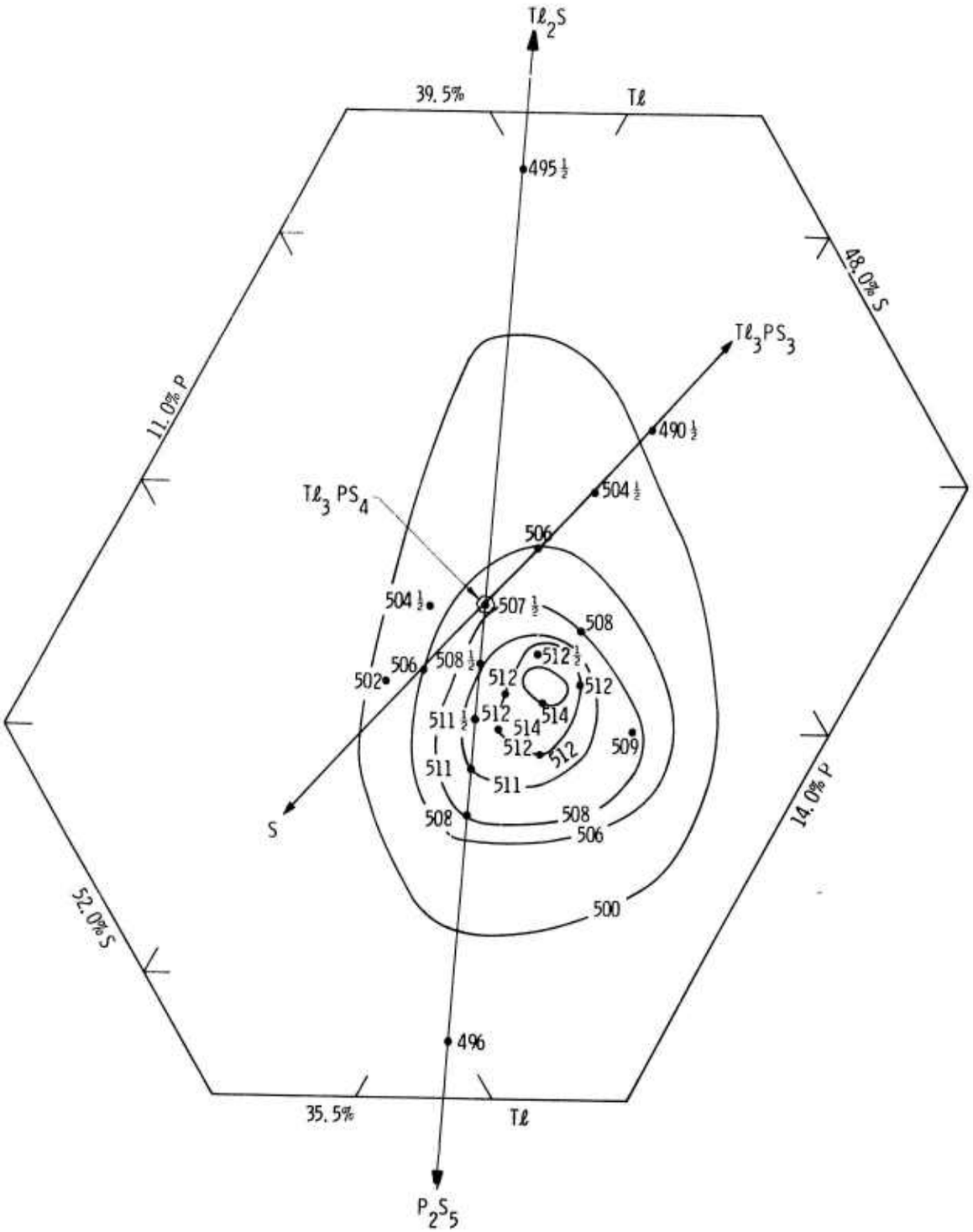

Fig. 8 – Liquidus map for the $Tℓ_3PS_4$ region of the system Tℓ-P-S

4.3 Studies in the System Tl-P-Se

The liquidus relations of Tl_3PSe_4 in the system Tl-P-Se are somewhat simpler than those of Tl_3PS_4 discussed above. Along the composition join Tl_2Se-P_2Se_5, there is a sharp maximum (459.5°C) in the liquidus curve at Tl_3PSe_4 composition. The diagram is shown in Fig. 9. The nonstoichiometry of the maximum-melting Tl_3PSe_4 composition is, however, seen on the liquidus curve along the Tl_3PSe_3-Se composition join (Fig. 10). The highest melting temperature observed on that join was 461°. The experiments conducted in the ternary system, i.e., which did not lie on composition joins, showed that the peak in the Tl_3PSe_4 liquidus surface corresponds very closely to that observed on the Tl_3PSe_3-Se join. Thus, the maximum-melting Tl_3PSe_4 composition is therefore a selenium-deficient composition represented approximately by the formula $Tl_3PSe_{3.95}$.

As was the case for Tl_3PS_4, x-ray powder patterns of the products of the runs shown on Fig. 11 did not show any shifts in the angular line positions that would indicate the presence of a measurable solid solution range.

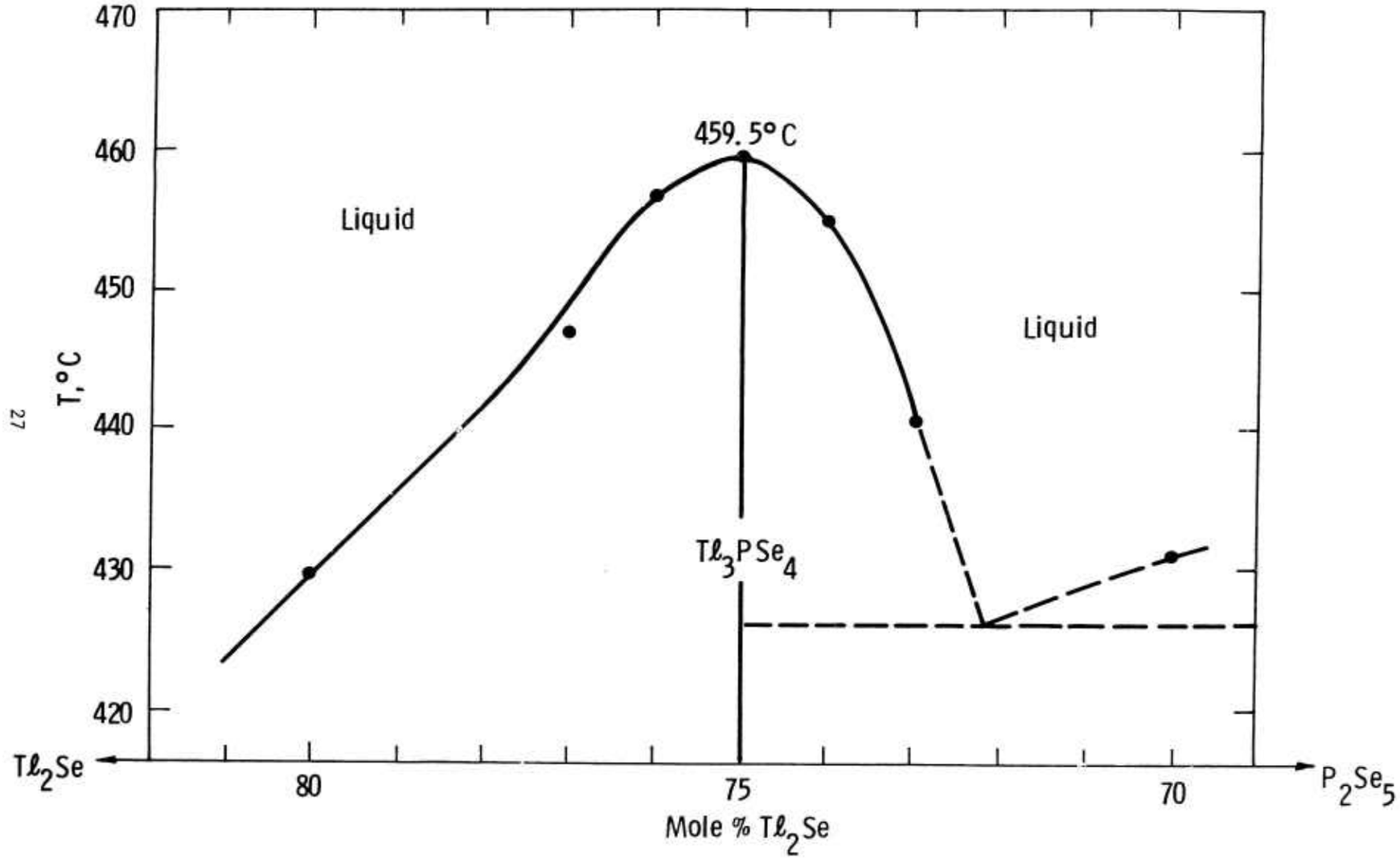

Fig. 9 —The $Tl_3P\,Se_4$ liquidus curve along the composition join Tl_2Se-$P_2\,Se_5$

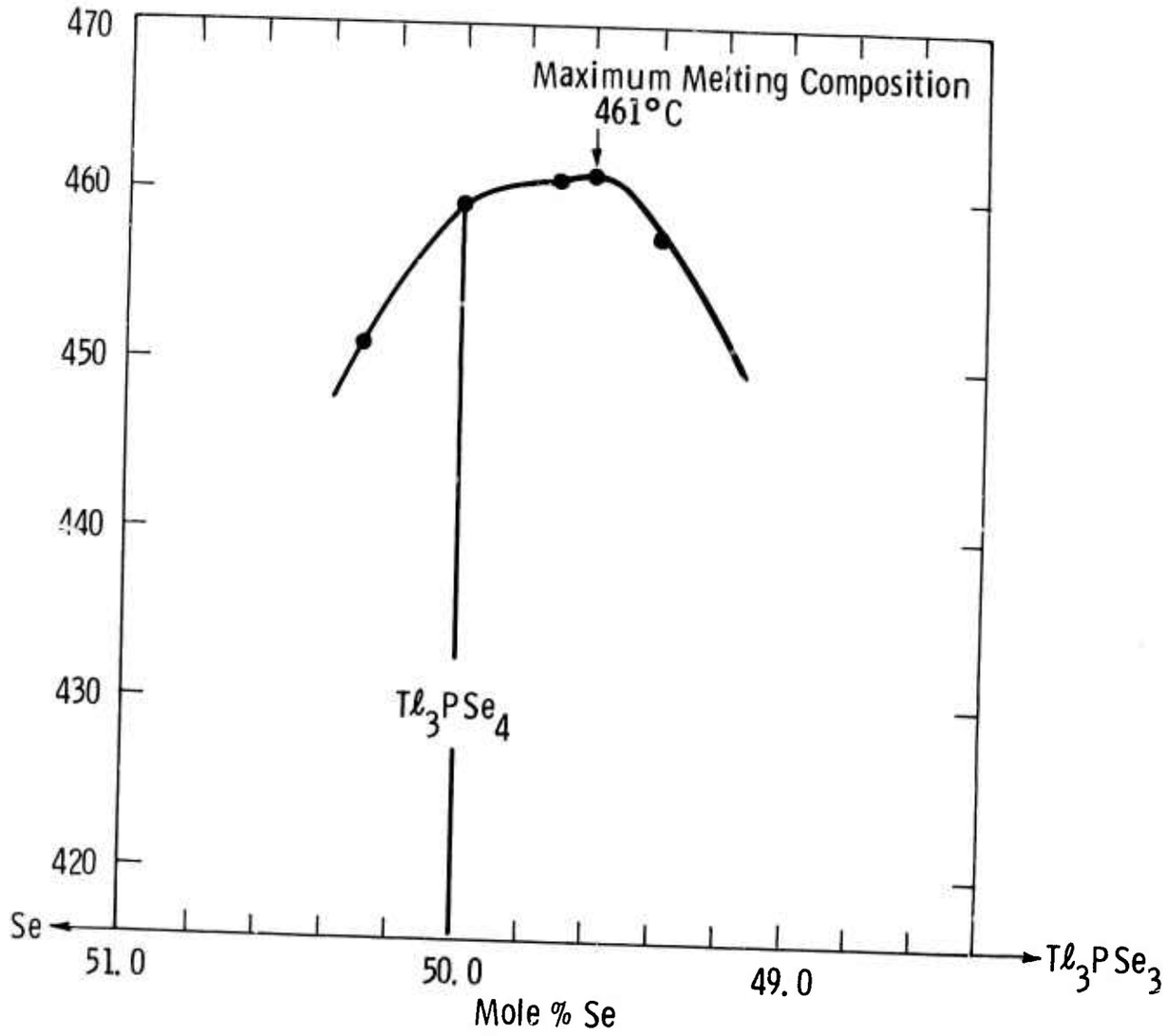

Fig. 10—The Tl_3PSe_4 liquidus curve along the composition join Tl_3PSe_3-Se

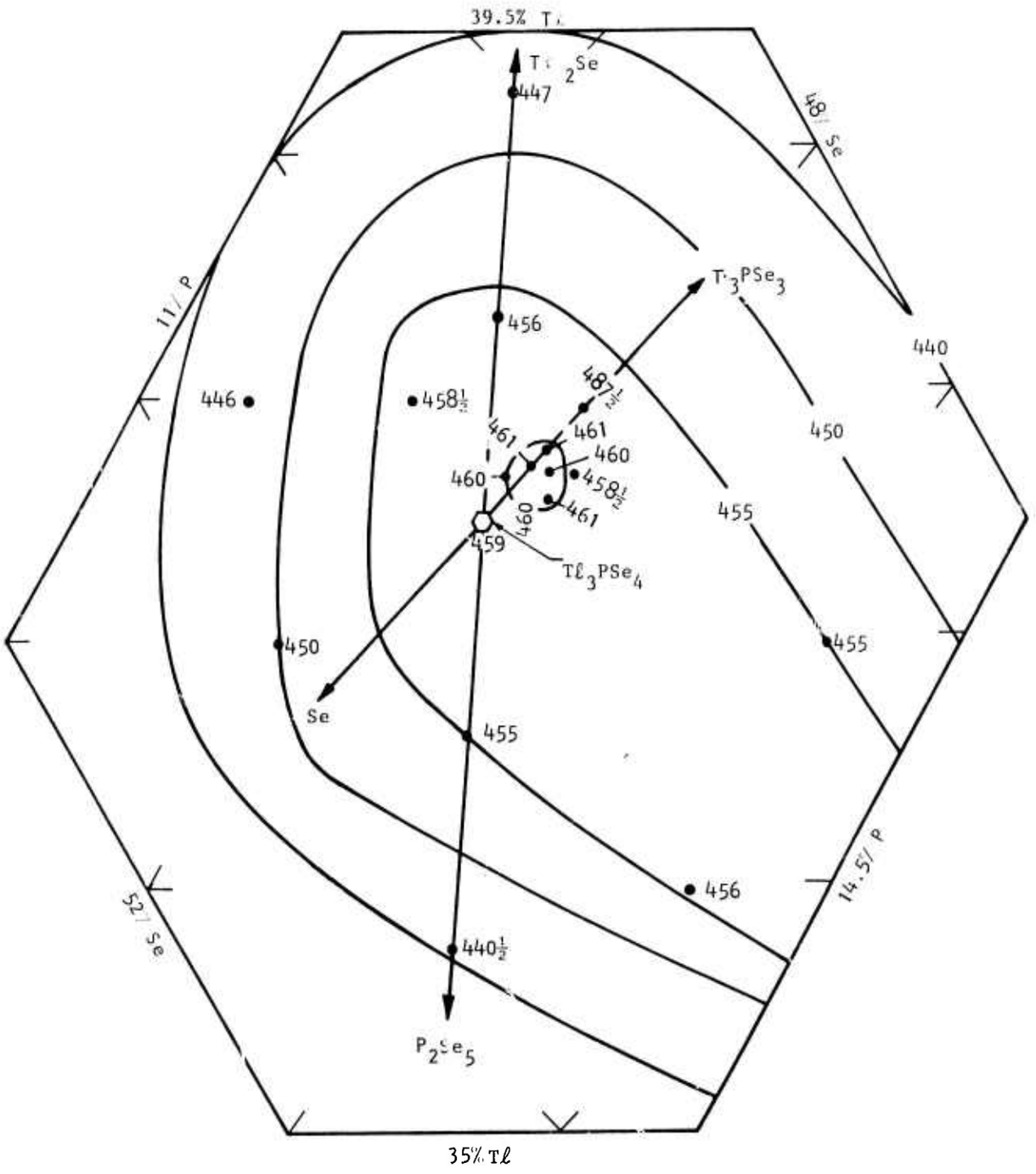

Fig. 11–The Tl_3PSe_4 liquidus surface in a portion of the Tℓ - P - Se system

5. CRYSTAL GROWTH OF Tl_3PS_4 AND Tl_3PSe_4

5.1 Introduction

The crystal growth of Tl_3PS_4 and Tl_3PSe_4 is considerably more difficult than for any of the other sulfosalt materials we have previously studied. The sulfosalt compound Tl_3AsS_4, for example, could readily be obtained as single crystal material and simply required optimization of the growth composition to reduce scattering losses and minimize cracking problems. In contrast, for Tl_3PS_4 and Tl_3PSe_4, it was considered a feat to even get single crystal material that was translucent to light. Our crystal-growth studies can be described as having three phases: 1) early (generally unsuccessful) growth experiments, 2) theoretical analysis of the crystal growth of Tl_3PS_4 and Tl_3PSe_4, and 3) successful growth experiments using large-volume melts and regrowth procedures. Much of this work has been concentrated on Tl_3PS_4 rather than Tl_3PSe_4 because the former is transparent to visible light and standard transmitted-light microscope techniques can be used to evaluate crystal quality. We assumed the growth problems associated with Tl_3PSe_4 to be of the same nature as with Tl_3PS_4, a valid assumption as it turned out. The three study phases listed above are described in the following sections.

5.2 Early Crystal-Growth Experiments

The first crystal-growth experiments were conducted on melts having the ideal Tl_3PS_4 and Tl_3PSe_4 compositions. These were conducted prior to any knowledge of the liquidus relations, and in view of the nonstoichiometric melting relations subsequently determined, it is not surprising that only polycrystalline material, completely opaque,

could be obtained. Subsequent growth efforts were confined to the maximum-melting regions of the liquidus surfaces of Tl_3PS_4 and Tl_3PSe_4 as determined from the thermal analysis study.

Crystal growth compositions used in the effort to grow good quality Tl_3PS_4 crystals are plotted on the Tl_3PS_4 liquidus surface in Fig. 12. The typical melt weighed 20 grams and the typical growth velocity was 12 mm/day (the significance of this is discussed in the next section). Boules grown from these compositions gave generally poor material and in only one run was measurable material obtained. The optical transmission of that material is shown in Fig. 13. The band edge is at about 0.52 μm, and the edge is not nearly as sharp as those seen in other sulfosalt single crystals. This is probably a result of scattering from small cracks on inclusions; a few small cracks were evident to the eye in this sample. The lattice absorption frequency appears to be in the 900 cm^{-1} region, higher than that of heavier sulfosalts, and in keeping with the general idea that lighter constituents will lead to higher lattice absorption frequencies. Attempts to reproduce this crystal in subsequent runs using the same growth conditions were not successful. More typical material obtained from these growth runs is shown in Fig. 14. Both crystal fragments are barely translucent to a strong microscope light. The other feature of note in Fig. 14 is the color difference between the two samples a surprising distinction in view of the similarity in growth compositions. This is undoubtedly a reflection of the liquidus trend as noted on the Tl_2S-P_2S_5 composition join (Sec. 4.2).

The optical examination of sections of Tl_3PS_4 boules clearly showed features indicative of a breakdown of the solid-liquid interface during crystal growth. Particularly important in this respect was the observation that cellular structure was often present (Fig. 15). Such structure is typically the result of constitutional supercooling during crystal growth. Inclusions of second phase observed in Tl_3PS_4 crystals (Fig. 16) provided additional evidence that growth compositions were

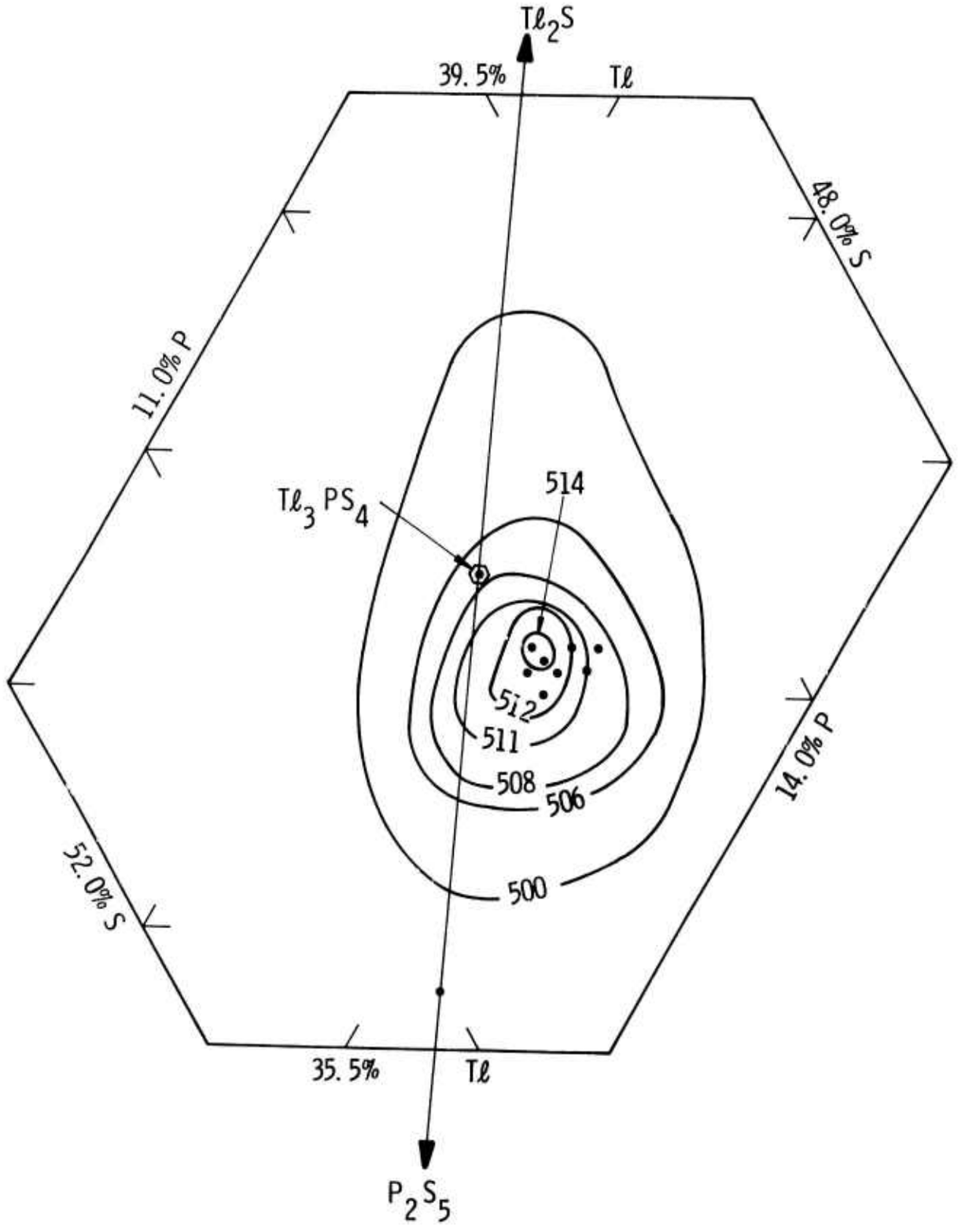

Fig. 12 — Compositions of crystal growth runs conducted in the system Tl-P-S

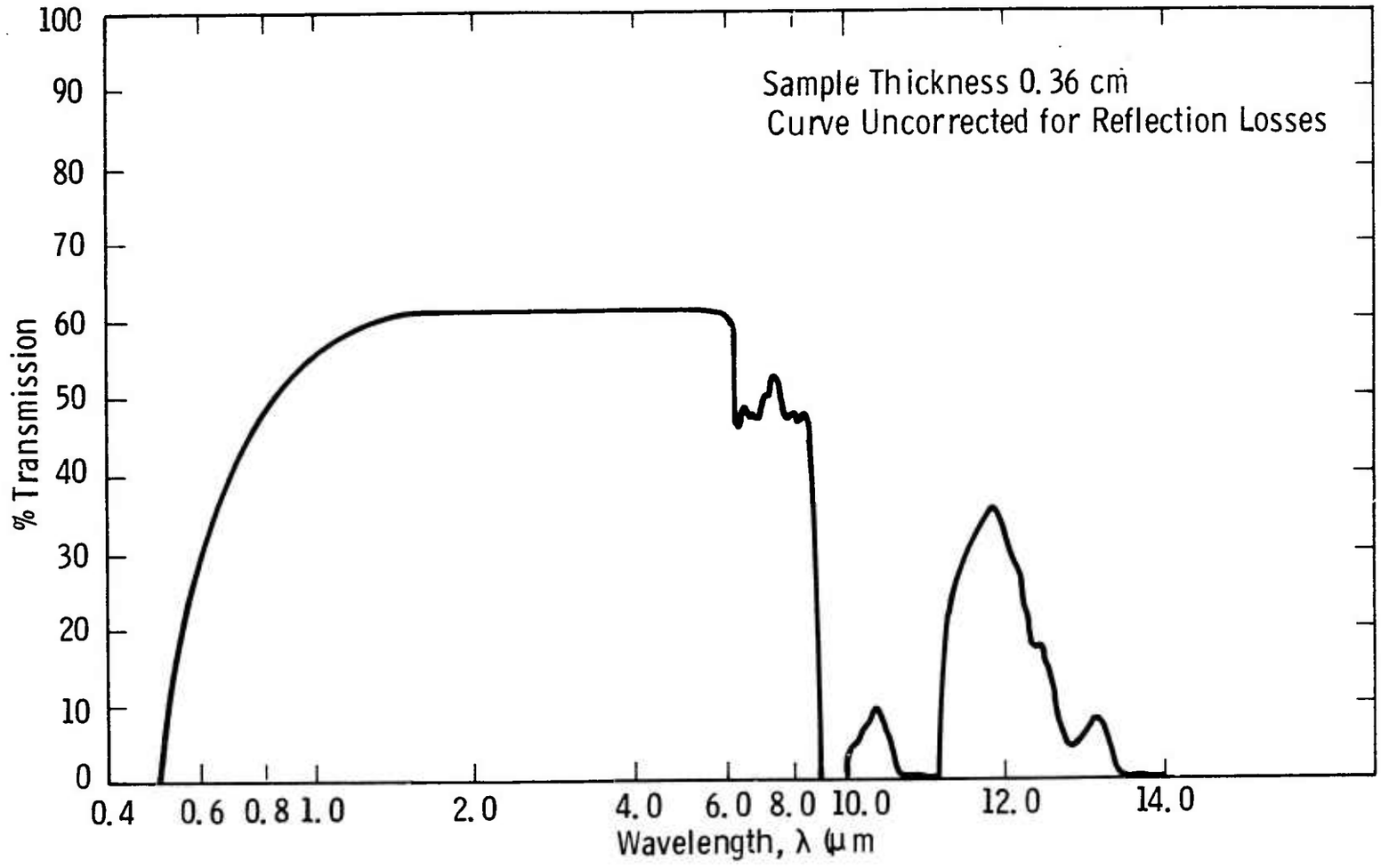

Fig. 13 - Optical transmission of $T\ell_3 PS_4$

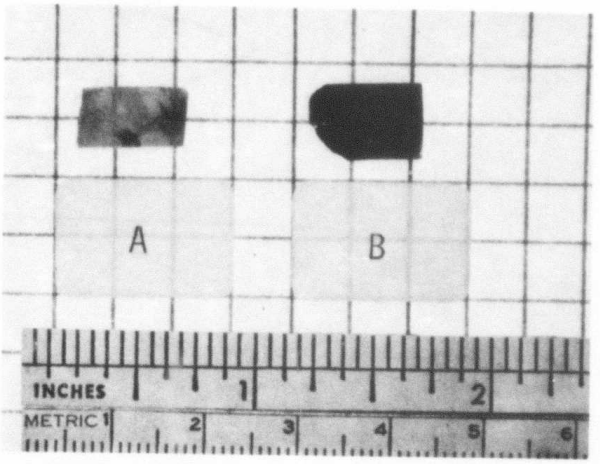

Fig. 14. Polished slices 2 mm thick of Tl_3PS_4 boules showing the typically poor optical transmission obtained in the early growth runs. Slice A was polished from boule MR 7-2 grown from a melt composition $Tl_{37.1}P_{13.1}S_{49.8}$. Slice B was polished from boule 206196-71 grown from a melt composition $Tl_{37.1}P_{13.0}S_{49.9}$.

Fig. 15. Cellular structure observed in Tl_3PS_4 crystal grown from a melt of composition $Tl_{37.1}P_{13.1}S_{49.8}$. Growth direction left to right. X500.

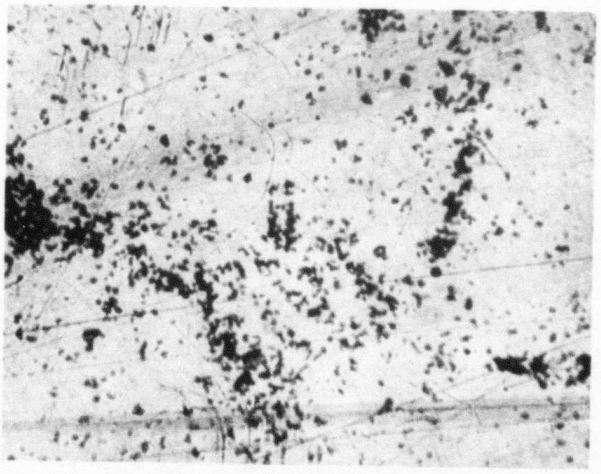

Fig. 16. Inclusions of a second-phase observed in a Tl_3PS_4 crystal grown from a melt of composition $Tl_{37.1}P_{13.1}S_{49.8}$. Growth direction left to right. X100.

not ideal (because of the measurable lack of solid solution these inclusions could not have formed by precipitation). These features of Tl_3PS_4 led us to the theoretical analysis of crystal growth described in the next section.

5.3 Theoretical Considerations Relating to Tl_3PS_4 Crystal Growth

We consider the crystal growth from a melt whose composition deviates slightly from the maximum-melting composition. In such a situation the atom fractions of solute in the solid and liquid phases at equilibrium are different. The magnitude of the difference is given by k_o, the distribution coefficient defined as the ratio of the solute concentration in the solid, c_s, to that in the liquid with which it coexists, c_L. Thus, when a crystal is grown by progressively freezing a non-congruently melting liquid, excess components will be rejected by the solid phase to accumulate ahead of the crystal-liquid interface.

The distribution of solute in the liquid will depend on what transport mechanisms operate. When there is no stirring, a small freezing velocity and a vertical temperature gradient -- as in most of our experiments -- solute should move mainly by diffusion. In this case the moving crystal-liquid interface will be preceeded at steady state by a solute-rich ($k_o < 1$) boundary layer whose concentration decays exponentially from the value, c_o/k_o at the interface to c_o, the bulk liquid composition, far from the interface. Mathematically, the liquid composition is given by

$$c_L = c_o \left[1 + \frac{1-k_o}{k_o} \, e^{\frac{V}{D} x} \right] \qquad (1)$$

where x is measured from the interface into the liquid and $\frac{V}{D}$ is the characteristic thickness of the boundary layer in terms of the freezing velocity V and solute diffusion coefficient D.

The presence of the solute-rich boundary layer during crystal growth has important consequences with respect to the optical quality

of single-crystal materials. This stems from the fact that the increased solute content of the liquid ahead of the interface depresses the equilibrium liquidus temperature relative to that of the bulk liquid. If the actual (applied) temperature in the liquid now 'falls' below the liquidus temperature, a zone of "constitutionally" supercooled liquid is established in which a planar crystal-liquid interface becomes unstable. The condition for the onset of constitutional supercooling is given by the well known relation

$$\frac{G}{V} < -\frac{mc_o}{D}\frac{1-k_o}{k_o} \qquad (2)$$

where G is the thermal gradient in the liquid and m is the liquidus slope from the relevant phase diagram.

Physically, when the inequality of Eq. 2 holds, the liquid near the interface is unstable with respect to the solid phase; any protrusion which forms on the interface can spontaneously grow into the supercooled liquid layer. Arrays of protrusions d lop surrounded by deep grooves in the interface to which solute rich liquid laterally diffuses and segregates. Solute enrichment in the grooves often exceeds the solubility limits of other phases in the system. The resulting array of inclusions takes on a fibrous morphology often termed cellular structure, such as shown in Fig. 15.

In typical sulfosalt experiments the freezing velocity lies in the range 5 to 15 mm/day (5.8 to 17.4 x 10^{-6} cm/hr) and the measured furnace thermal gradients are 80 to 120°C/cm (the actual gradient in the freezing liquid will be less than the furnace gradient). We may rearrange Eq. 2 to estimate the maximum tolerable departure from the congruent composition for which no constitutional supercooling occurs under these conditions:

$$c_o < -\frac{DG}{mV}\frac{k_o}{(1-k_o)} \qquad (3)$$

In the case of Tl_3PS_4 m = - 10°C/mole % P_2S_5 and $k_o \sim 0.01$. We take

$D \tilde{=} 10^{-5}$ cm^2/sec, the value calculated for proustite[4] and typical of many liquids. If G = 100°C/cm and V = 11.6×10^{-6} cm/sec, values commonly employed, we find $c_o < .09$ mole % P_2S_5 to avoid interface breakdown when growing Tl_3PS_4. The magnitude of the allowable composition variation c_o is quite small considering the relatively high G and low V values employed. In fact, the variation in c_o is comparable to the precision with which we can measure the value of the stoichiometric Tl_3PS_4 maximum melting composition and it is also comparable in magnitude to the weighing errors expected in a typical 20 g charge. Clearly, to successfully grow inclusion-free Tl_3PS_4 crystals requires that we freeze samples with the highest G and lowest V practical in our system, and that large charges be utilized to minimize weighing errors.

As written, Eq. 2 predicts whether a stable planar crystal-liquid interface will ever break down at steady-state. Since the initial crystal to form must have a composition $k_o c_o$ given by the phase diagram, it follows that constitutional supercooling will not develop until enough crystal has formed to reject into the liquid the critical amount of solute to stimulate interface breakdown. By recasting Eq. 2 we can calculate the length of this transient, x_c

$$\frac{G_L}{V} < \frac{-mc_o}{D} \frac{(1-k_o)}{k_o} \left[1 - \exp\left(\frac{-ky}{D} x_c\right)\right] \qquad (4)$$

Using the parameter values for Tl_3PS_4 we estimate that about 8 cm of crystal need be grown before spontaneous breakdown would occur for a crystal of uniform diameter. However, since TPS crystals are marginally stable to breakdown under the usual growth conditions, other transient phenomena may intervene to induce inclusions well before the steady-state spontaneous instability develops.

In our experiments solute transients are introduced primarily in two ways, by variation in the crystal growth velocity and available melt volume. The operation of the first mechanism is obvious. If the growth tube hangs up or the furnace temperature varies, V will depart

from the steady state value and the thickness of the diffusion boundary layer D/V will abruptly change. For an increase in V, less solute can diffuse away from the interface per unit time, the interface concentration rises above the critical value and inclusions develop. The phenomenon, called banding, is well known in crystal growth.

The second mechanism operates because of the design of the growth tube and its finite size. Each growth tube contains a constriction or neck to promote single crystal growth. As the crystal-liquid interface approaches the neck, the melt volume available to permit forward diffusion of solid diminishes. In the vicinity of the neck the critical solute concentration for interface breakdown is exceeded and inclusions form. Just past the constriction where the tube diameter recovers its original size, the inclusions disappear as a new boundary layer is rebuilt. The same kind of transient or end effect can occur at a distance D/V $\sim$ 1 cm from the terminus of the growth tube. Here the end of the tube restricts diffusion, solute concentration increases and inclusions again form. Thus, from a view of transient effects long growth tubes (large charge mass) favors improved crystal quality as does a highly stable furnace control and drive system.

By comparison at the same G/V values the growth of extremely perfect Tl_3AsS_4 crystals is relatively easy. This is because the liquidus slope for Tl_3AsS_4 is about one third as steep as that of Tl_3PS_4. Hence, faster growth rates, lower thermal gradients or larger error in composition during melt preparation can all be tolerated compared to growing Tl_3PS_4. Even for Tl_3AsS_4, however, the growth conditions are not far removed from those which allow interface breakdown. This is evident in Fig. 17 for crystals of Tl_3AsS_4 grown from melts of $Tl_3AsS_{3.95}$ composition (about 0.2 mole % S away from the ideal stoichiometric composition). For example, severely cracked and clouded crystals were obtained when growth rates exceeded about 15 mm/day at a temperature gradient of about 10°C/mm. Since the curve shown in Fig. 17

is expected to be displaced upward with steepening liquidus slope, it is therefore not surprising that crystal growth conditions used to obtain high-quality Tl_3AsS_4 crystals fail when applied to Tl_3PS_4.

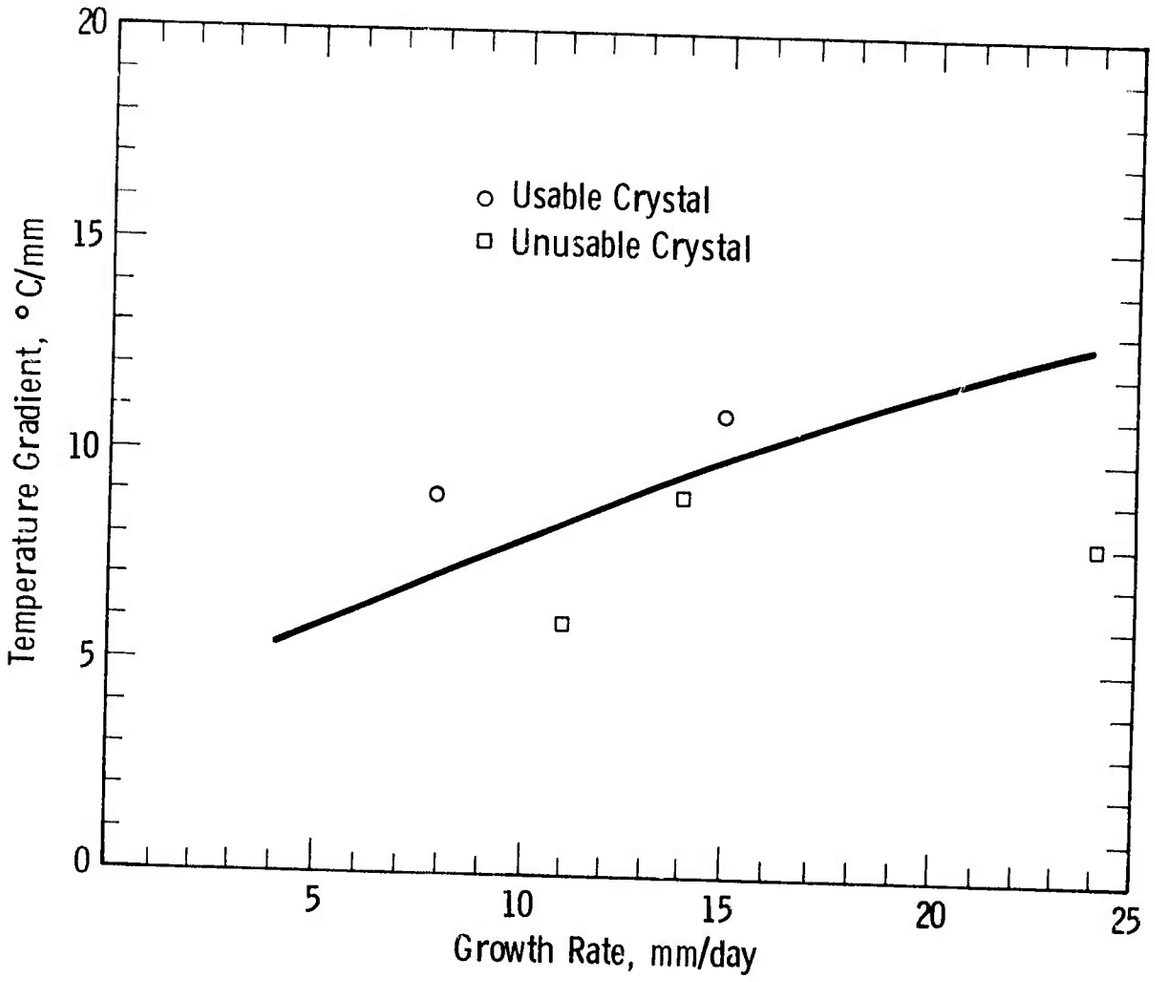

Fig. 17. Crystal growth data for Tl_3As_4 grown from melts of $Tl_3As_{3.95}$ composition.

5.4 Revised Crystal-Growth Procedures for Tl_3PS_4 and Tl_3PSe_4

Our previous experiences with crystal growth of Tl_3PS_4 and Tl_3PSe_4 and the theoretical considerations detailed in Sec. 5.3 led us to revise the crystal growth techniques as follows:

- Reactant material was prepared in batches of 40 to 60 grams rather than as 15-20 gram batches as previously used. In this way weighing errors (on a percent basis) were minimized.
- All the prepared reactant material was used for a single growth run. Thus, a larger volume of melt was available during most of the crystal-growth run for the resolution and redistribution of impurities that were rejected from the crystal ahead of the solid-liquid interface during crystal growth.
- The crystal growth rates were decreased to 5-8 mm per day.
- A regrowth procedure was established. Following growth of a crystal, the last-to-grow 1 cm of the boule and about 1 cm of crystal above the neck in the crystal-growth tube were discarded. The remaining boule was reloaded into a new crystal-growth tube and passed again through the crystal-growth furnace. In this way material containing second-phase inclusions because of transient effects was discarded and the material used for the second growth pass was much closer to maximum-melting material than could be prepared by weighing and melting elemental reactant materials.

The implementation of the above procedures immediately resulted in improved crystal quality for Tl_3PS_4. This was evident even without the regrowth step. After the first pass, the boules contained large areas of clear material (absorption less than $0.1\,cm^{-1}$) with translucent to opaque areas immediately above the neck and at the last-to-grow end of the charge. The appearance of these areas is shown in Figs. 18 and 19. Regrowing the central section of such boules usually gave clear material (absorption $< .05\ cm^{-1}$) such as shown in Fig. 20.

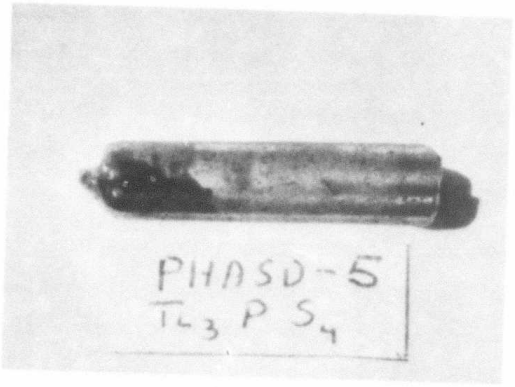

Fig. 18. Boule of Tl_3PS_4 showing area of dark and cracked crystal occurring above the neck in the growth tube (left-hand end of boule). The boule is 3 cm in length.

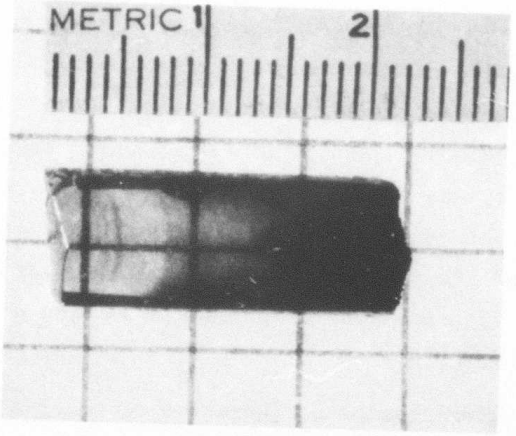

Fig. 19. Polished slice of Tl_3PS_4 crystal showing the dark and opaque material in the last-to-grow portion of the crystal. The slice is 4 mm in thickness.

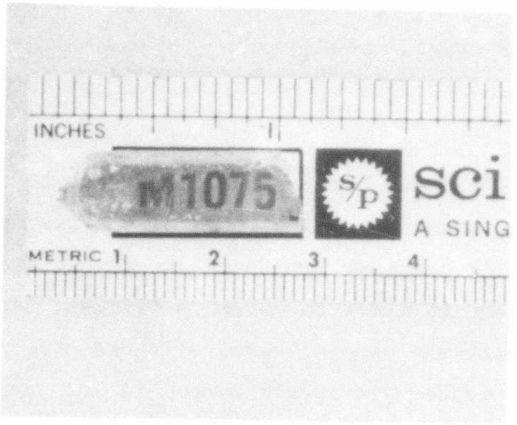

Fig. 20. Polished slice of Tl_3PS_4 crystal (PHASD-6) having good optical transmission. The slice is 6 mm thick.

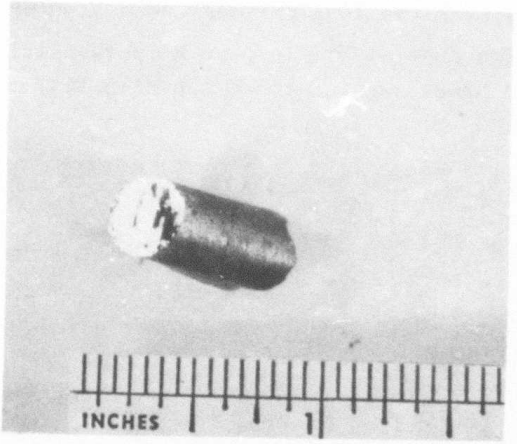

Fig. 21. Cracked crystal of Tl_3PSe_4 showing the well developed {010} cleavage. The crystal is 8 mm in diameter.

Time restrictions prevented the extensive application of the revised crystal growth techniques to Tl_3PSe_4. One growth run was made, however, from the composition $Tl_{.377}P_{.127}Se_{.496}$; the product after the regrowth cycle was of very good single-crystal quality as determined by x-ray single crystal photographs. Although the crystal was cracked, the cracks reflected the well-developed {010} cleavage (Fig. 21).

There still remain, however, problems with the crystal growth of Tl_3PS_4 and Tl_3PSe_4, problems which ironically arise because of the revised techniques. As presently employed, these techniques require long charges, 10-20 cm, in order to obtain sufficient lengths of material. As a result, the crystals generally crack during cooling to room temperature because our growth system is not designed to provide uniform temperature zones over such lengths. In addition, the slow growth rates, 5-8 mm/day, give rise to stability problems; our growth system is not designed to provide temperature and crystal growth-rate stability over the long periods necessary for each growth pass (15-20 days). The crystals reflect such instabilities in the presence of inclusion bands such as those shown in Fig. 22. We believe,

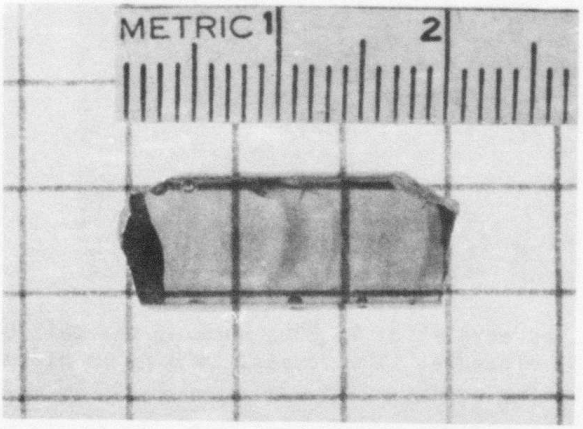

Fig. 22. Polished slice of Tl_3PS_4 crystal showing the development of solute bands in the crystal. The slice is 4 mm thick.

however, that the basic problems in the crystal growth of Tl_3PS_4 and Tl_3PSe_4 have been delineated and solved, and that an improved crystal growth system would result in the reproducible growth of these crystals on a routine basis. More importantly, perhaps, we have gained much insight into the crystal growth of ternary sulfosalt materials.

6. OPTICAL PARAMETRIC OSCILLATION

6.1 Summary

Although Tl_3AsSe_3 does not possess the highest nonlinear optical coefficients of infrared nonlinear materials, the material can be grown in large size crystals of good quality, so that hopefully these crystals with suitable antireflection coatings would present losses in an OPO cavity low enough to allow net gain to be parametrically generated and oscillation to occur. Unfortunately, no output was observed from Tl_3AsSe_3 in attempts to pump a double resonant oscillator. Possible reasons for this might include failure to achieve the exact crystal orientation and oscillator alignment for phase matching, or pump-induced losses in the material, such as two-photon absorption. In a separate experiment, however, no two-photon absorption was observed up to power densities of 6 Mw/cm^2, well above the calculated oscillator threshold power densities. Similar attempts in Ag_3AsS_3 also failed to generate reliable oscillator action because of the lower value of the nonlinear optical coefficient. Here, however, parametric fluorescence in the 4 μm region was observed, and a few instances of erratic spiking output which could possibly have been oscillator action were observed.

6.2 Oscillator Design

For an optical parametric oscillator system with small losses, the small signal threshold condition on the gain G is[15,16]

$$G = \Gamma^2 \ell^2 = 2\alpha_s \quad \text{(singly resonant, idler coupled out)} \qquad (1a)$$

$$G = \Gamma^2 \ell^2 = \alpha_s \alpha_i \quad \text{(doubly resonant)} \ , \qquad (1b)$$

where α_s and α_i are the single pass power losses at signal and idler wavelengths, respectively, and ℓ is the crystal length. It is clear that for small losses, the doubly resonant configuration requires gains considerably lower than the singly resonant system. For initial oscillator tests the doubly resonant configuration was therefore chosen.

As a function of pump beam and nonlinear material parameters, the single pass power gain for the case where phase matching is not at 90° to the crystal optical axis is given, for signal, idler and pump beams confocally focused in the crystal, by[15,16]

$$\Gamma^2 \ell(^2\rho) = \frac{2\,\omega_s \omega_i |d|^2\, \ell}{\pi\, n_s n_i n_p \varepsilon_o c^3} P_p k_o \bar{h}_m(B,\xi)(1-\delta^2)^2 \qquad (2)$$

Here, d is the effective nonlinear optical coefficient, n is the refractive index, ω_s and ω_i the signal and idler frequencies, c the velocity of light, ε_o the permittivity of free space, and P_p the pump power.

The factor $(1-\delta^2)^2$ is the "degeneracy factor", which describes the extent to which gain is reduced when the system is tuned away from degeneracy ($\lambda_s = \lambda_i = 2\lambda_p$). The factor δ is defined as

$$\delta \equiv \frac{2\lambda_p - \lambda_s}{\lambda_s} \quad .$$

The reduction in gain due to the Poynting vector walkoff[17] is accounted for by the factor $\bar{h}_m(B,\xi)$, where

$$B \equiv \frac{\rho}{2}\left(\frac{2\pi\ell}{\lambda}\right)^{1/2}\left(\frac{n_p}{n_o}\right)^{1/2} \qquad (3)$$

is the "birefringence parameter". The parameter ξ is defined as the ratio of crystal length to effective length of the focused beam in the crystal, $\ell/b \equiv \zeta$. The beam parameter b is related to the beam radius at the waist by

$$b = W_o^2 \frac{2\pi n}{\lambda_o} \,,$$

where λ_o is the degenerate wavelength. The so-called birefringence angle, ρ, is the small angle at which the Poynting vector, or power flow, departs from the phase propagation direction for beams propagating in birefringent crystals; and can be calculated from the measured values of the refractive

indices. Values of the factor $\bar{h}_m(B,\xi)$ have been calculated by Boyd[17] for various beam conditions. This factor can also be approximated over a wide range of $\xi = \ell/b$ by

$$\bar{h}_m(B,\xi) \tilde{=} \frac{\pi}{4B^2} \text{ when } \xi \text{ is in the range } \frac{B^2}{4} > \xi > \frac{2}{B^2} \quad .$$

To determine a value for $\bar{h}_m(B,\xi)$, and evaluate the gain and thus the pump power required for oscillator threshold, we consider in more detail the phase matching conditions associated with the nonlinear materials used in the experiment, namely Tl_3AsSe_3 and Ag_3AsS_3.

For Tl_3AsSe_3, the refractive indices are given by the Sellmeier equations[7]

$$n_o^2 - 1 = \frac{10.125}{1 - \left(\frac{0.445}{\lambda}\right)^2} + \frac{0.10}{1 - \left(\frac{20}{\lambda}\right)^2} \qquad (4a)$$

$$n_e^2 - 1 = \frac{8.96}{1 - \left(\frac{0.445}{\lambda}\right)^2} - \frac{0.05}{1 - \left(\frac{20}{\lambda}\right)^2} \quad . \qquad (4b)$$

Phase matching curves[7] for Type I matching for optical parametric generation in Tl_3AsSe_3 based on the above Sellmeier equations are shown in Fig. 23. The exact phase match angle for degenerate oscillation at a pump wavelength of 2.098 μm can be calculated as follows. The index matching scheme follows that for Type I phase matching in a negative uniaxial crystal, as discussed by Midwinter and Warner.[18] The pump beam at frequency ω_p propagates as an e-ray, while signal and idler at ω_s and ω_i propagate as o-rays. In the following, subscripts p, s, and i denote pump, signal and idler, and superscripts e and o denote extraordinary or ordinary rays. Matching of momentum vectors requires that we find a propagation direction Θ with respect to the crystal optic axis such that

$$n_p^e(\Theta) = \frac{\omega_s}{\omega_p} n_s^o + \frac{\omega_i}{\omega_p} n_i^o \quad . \qquad (5)$$

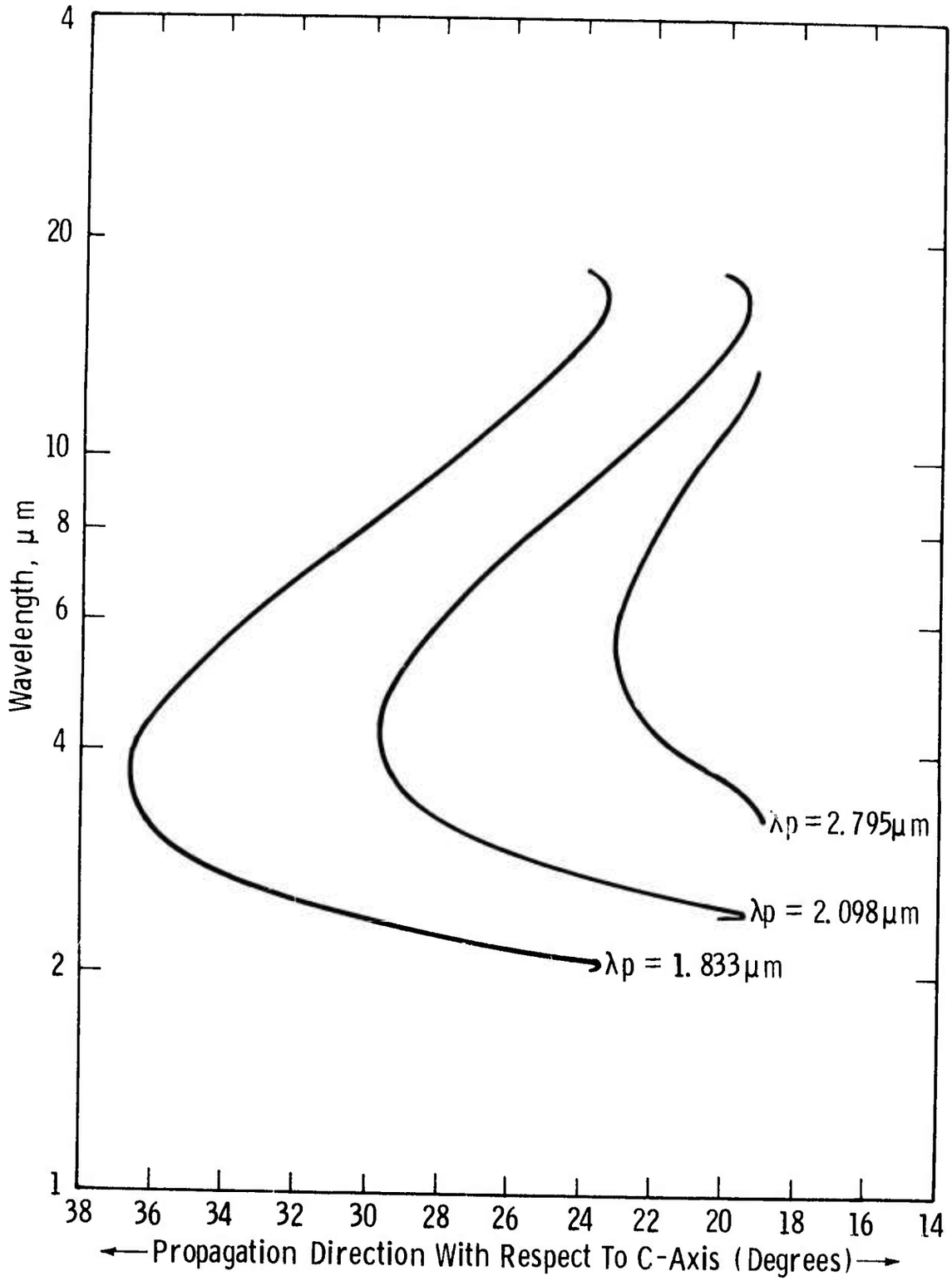

Fig. 23 -Phase matching curves (Type I) for optical parametric oscillation in Tl_3AsSe_3

For ω_p as an e-ray propagating at an angle θ to the optic axis,

$$n_p^{e^2}(\theta) = \frac{n^o n^e}{n_p^{o^2} \sin^2\theta + n_p^{e^2} \cos^2\theta} \quad . \tag{6}$$

Equations (4) and (5) and solving for θ gives us the required phase matching direction. It should be noted that in Ref. 18, n^o and n^e are interchanged in the denominator of the right hand side of equation (5), which is inconsistent with the definition of θ as measured from the optic axis.

For the degenerate case, $\omega_s = \omega_i$, and equations 5 and 6 then give

$$\sin^2\theta_m = \frac{\frac{1}{n_s^{o^2}} - \frac{1}{n_p^{o^2}}}{\frac{1}{n_p^{e^2}} - \frac{1}{n_p^{o^2}}} \quad . \tag{7}$$

Solving (7) exactly, using the Sellmeir equations (4a,b) at $\lambda_p = 2.098$ μm and $\lambda_s = \lambda_i = 4.196$ μm, we find the phase match angle in Tl_3AsSe_3 to be

$$\theta_m = 31.8° \quad .$$

The birefringence angle, ρ, may be calculated from[16]

$$\tan\rho = \frac{1}{2} \sin 2\theta_m \left[\frac{n_p^{o^2} - n_p^{e^2}}{n_p^{e^2} \cos^2\theta_m + n_p^{o^2} \sin^2\theta_m} \right] \quad . \tag{8}$$

For the above degenerate case in Tl_3AsSe_3, this yields

$$\rho = 0.0509 \text{ rad} = 2.91°$$

The birefringence parameter B (Eq. 3) for a crystal length

ℓ = 1 cm, then becomes,

$$B = \frac{5.09 \times 10^{-2}}{2}\sqrt{\frac{2\pi}{4.196 \times 10^{-4}}}\sqrt{\frac{3.2222}{3.3520}} \quad ,$$

$$B = 3.053 \quad .$$

We will see in a later section that the confocal parameter, b, of the oscillator cavity used, is about 6.7 cm at $\lambda_s = \lambda_i = 4.2$ μm. Thus

$$\xi = \frac{\ell}{b} \simeq 0.15 \quad .$$

From the curves for $h_m(B,\xi)$ given in Ref. 17 the gain reduction factor can be interpolated to be

$$h_m(3.05,0.15) \simeq 0.063 \quad .$$

With this value for $h_m(B,\xi)$, we can calculate the single pass gain per unit of pump power for confocally focused signal, idler and pump beams at degeneracy ($\lambda_o = 4.196$ μm). For the effective nonlinear optical coefficient, we have

$$d^+(Tl_3AsSe_3) = d_{22}\cos(\theta_m+\rho) + d_{31}\sin(\theta_m+\rho) \quad .$$

For $d^+(Tl_3AsSe_3)$ our most recent fully corrected measurements made relative to $d^+(Ag_3AsS_3)$ for second harmonic generation at 10.6 μm give

$$\frac{d_+(Tl_3AsSe_3)}{d_+(Ag_3AsS_3)} = 3.10$$

Chemla et al.[19] recently made accurate measurements of d_{22} and d_{31} for Ag_3AsS_3, finding that, on the basis of the Levine and Bethea measurement of d_{36}(GaAs),

$$d_{31}(Ag_3AsS_3) = 27 \times 10^{-9} \text{ esv} = 11.3 \times 10^{-12} \frac{M}{V}$$

$$d_{22}(Ag_3AsS_3) = 1.6\ d_{31}(Ag_3AsS_3) = 18.1 \times 10^{-12} \frac{M}{V} \quad .$$

We will see later that for 2.1 μm-pumped degenerate oscillation in Ag_3AsS_3, the phase match angle $\theta_{pm} \tilde{=} 15.9°$ and $\rho \tilde{=} 2.7°$. Thus,

$$d^+(Ag_3AsS_3) = 20.8 \times 10^{-12} \text{ M/V, and}$$

$$d^+(Tl_3AsSe_3) \tilde{=} 56.4 \times 10^{-12} \text{ M/V for the same configuration.}$$

With these values for the parameters, equation (2) yields a gain per watt for a 1 cm long Tl_3AsSe_3 crystal in our cavity configuration (B = 3.05, ξ = 0.15)

$$\Gamma^2\ell^2 = 15.0 \times 10^{-5} \text{ P (watts)} \qquad (9)$$

Several criteria can be cited for thresholds. The simplest in concept is that the single pass gain must exceed the single pass loss, which for the doubly resonant configuration is represented in Eq. 1b. In the degenerate case, $\alpha_s = \alpha_i$, and for our system with Tl_3AsSe_3 we can reasonably expect the following losses with an antireflection coated crystal:

$$a_{\text{reflection}} = 2\alpha(\text{residual reflection}) = 2(0.05 \text{ per surface}) = 0.1/\text{pass}$$

$$\alpha(\text{bulk loss}) \lesssim 0.05 \text{ cm}^{-1} \times 1 \text{ cm} = 0.05/\text{pass}$$

$$a_{\text{output}} = \alpha(\text{output coupling}) = 0.02/\text{pass}$$

$$a_s = a_i = 0.17/\text{pass}.$$

With this and Equations 1b and 9, we find that the cw threshold pump power must be

$$P_p = \frac{(0.17)^2 \text{ watts}}{15 \times 10^{-5}} = 193 \text{ watts} \quad .$$

The corresponding pump power density in Mw/cm^2 is approximately given by dividing this pump power by the area of the confocal spot size in the resonator cavity:

$$\frac{P_p}{A} = \frac{0.134 \times 10^3 \, \omega}{\pi \omega_o^2} = \frac{0.134 \times 10^3}{\frac{\lambda}{2} b_o} = \frac{0.134 \times 10^3 \, \omega}{(2.098 \times 10^{-4})(6.7 \text{ cm}^2)}$$

$$= 0.14 \text{ Mw/cm}^2 \text{ for } b_o = 6.7 \text{ cm.}$$

A more stringent and more realistic pump power requirement is obtained by considering that the oscillator signal must build up from spontaneous noise in the cavity, and that therefore the parameteric gain must be large enough and must exist for a long enough time to allow such a build-up. Byer[16] has shown that this requirement can be formulated in terms of an equivalent loss associated with the finite rise time of the oscillator, and we will use his treatment to estimate the threshold pump power requirements on that basis. Pearson[20] has also calculated the rise times of parametric oscillators and the pump requirements on this basis, but his calculated curves do not cover all of the parameters involved in our system.

The power at the degenerate frequency starts out from a noise power $P_o(0) \tilde{=} h\omega_o/\tau_{ph}$, equivalent to that present in a single cavity mode, and grows at a rate proportional to the excess gain. Here τ_{ph} is the lifetime of a photon in the cavity,

$$\tau_{ph} = \frac{\ell/c}{-1/2 \, \ell n R_1 R_2 + \alpha_T} \quad .$$

Since signal and idler losses are the same, the power at λ_o increases with time as

$$P_o(t) = P_o(0)e^{2[\Gamma(t)\ell - a]} \quad , \tag{10}$$

where a is the single pass power loss at λ_o, and $\Gamma(t)\ell$ the instantaneous single pass gain. Equation (10) can be rewritten and integrated in time to yield

$$\ell n\left[\frac{P_o(t)}{P_o(0)}\right] = 2\Gamma(t)\ell - 2a$$

$$\sqrt{\Gamma(T)\ell} = a + \frac{L_c}{2\tau_p c}\ \ell n\left[\frac{P_o(T)}{P_o(0)}\right] \quad , \tag{11}$$

where $\Gamma(T)\ell$ is the gain required to generate signal power $P_o(T)$ times the noise power. The second term in the expression is the loss equivalent of the DRO finite rise time. The quantity $\tau_p c/L_c$ is the number of transits, η, of the cavity made by the signal during the pump pulse. The only remaining issue to be settled is to define how large $P_o(T)$ must be for the oscillator to be considered "on". Since the expression involves $\ell n\ P_o(T)$, the gain is not a sensitive function of it; a reasonably conservative definition is to set $P_o(T)$ at some fraction of the peak pump power, for then it can be detected with good discrimination against the pump signal if bandpass filters with good blocking or spectrometers with good stray light rejection are available.

If we choose the fraction to be the total cavity loss at λ_o, $-1/2\ \ell n\ R_1R_2+a$, this slightly simplifies the calculation. For a typical DRO, $-1/2\ \ell n\ R_1R_2+a$ will be in the range of $0.05 \rightarrow 0.3$. If we so choose, then

$$\frac{P_o(T)}{P_o(0)} \rightarrow \frac{P_p^P}{hw_o/L/c} \quad ,$$

where P_p^P is the peak pump power and L/c is simply the transit time in the cavity. Thus the gain criterion for our DRO becomes

$$\Gamma^2 \ell^2 = (15 \times 10^{-5})\ P_p^p = \left\{ a + \frac{1}{2n} \ell n \left[\frac{P_p^p}{h\omega_o/(L/c)} \right] \right\}^2 . \qquad (12)$$

This equation can be solved by iteration to find the required P_p^p.

For our system, we have $L \tilde{=} 12$ cm, $a = 0.17$, and $\tau_\rho \tilde{=} 150$ ns, $\eta = \tau_\rho c/L = 37.5$, $hw_o/L/c \tilde{=} 1.185 \times 10^{-10}$ watts.

Solving (12) by iteration with these parameters yields

$$P_p^p = 2.2\,\text{kw} \quad ,$$

and the required peak pump power density is then

$$\frac{P_p^p}{\pi\omega_o^2} = 1.55\ \frac{\text{Mw}}{\text{cm}^2} \quad .$$

Rise time considerations thus increase threshold pump requirements by about a factor of ten over the cw threshold. Also note that the loss equivalent of the DRO rise time is about 40% per pass, compared to the existing static cavity loss of 17% per pass.

Byer[16] has also shown that since the pump peak power must be on long enough for the signal to build up, this is equivalent to a requirement of a minimum threshold <u>energy</u> density rather than power density,

$$W_{min}^{DRO} > \frac{P_p^p/A}{\sqrt{\frac{\Gamma^2\ell^2}{a} - 1}} \left(\frac{\tau_{cav}}{2a} \right) \ell n \frac{P_p^p}{\left(\frac{h\omega_o}{\tau_{cav}} \right)}$$

For our case at the previously calculated values of pulsed threshold, with $P_p^p = 2.2$ kw, $P_p^p/A = 1.55\ \text{Mw/cm}^2$, we find $W_{min}^{DRO} > 235$ millijoules/cm^2, which for the given spot size is equivalent to a pulse energy of 230 microjoules/pulse. Very similar considerations yield corresponding values for another material under consideration, Ag_3AsS_3. For this material, we have used refractive index values given in Ref. 21, because these index values seem to give best agreement with the measured values of

θ_{Pm} (10.6 μm SHG) by us and others. A summary of the calculated OPO parameters for degenerate operation of the two materials at a pump wavelength of 2 098 μm in a doubly resonant oscillator using parameters of our system is shown in Table 4. Although the results were arrived at under slightly different assumptions and values of parameters, they are in reasonable agreement with other calculations on similar systems.[16,22]

6.3 Pump Laser Design and Output Parameters

Two different Ho:YAG pump lasers were used in the OPO experiments. The first used a large (9") spherical optical pumping cavity with convective liquid nitrogen cooling, and has been described in a report on a previous contract.[23] The second used a more compact (6") spherical pump cavity, with cooling by forced supercooled circulating liquid nitrogen, and is described in more detail below. Both lasers were cw-pumped, and continuously Q-switched by a rotating mirror.

A diagram of the smaller laser is shown in Fig.24, and a picture of the laser is shown in Fig. 25. The laser rod (3 x 30 mm), cemented between stainless steel rod holders with RTV, is contained in a double-walled dewar which is silvered except for the 35 mm section surrounding the laser rod. A tungsten-iodine pump lamp (Type 300T4QC1 or 200T4QC1) is mounted alongside the clear section of the dewar with transite mounts which clamp onto the outside circumference of the dewar. The entire dewar assembly is mounted at each end on x-y mounts, so the rod assembly position can be optimized inside the mode volume of the laser cavity, which consists of a flat output mirror of reflectivity 92.5%, and a rotating mirror of 1 meter radius of curvature with 100% reflectivity. A hemispherical configuration (mirror spacing about 52 cm) is used. Brewster angle windows mounted on aluminum tubes seal the cold laser rod ends from the atmosphere; the space between laser rod ends and the windows is vacuum evacuated to forepump pressure to prevent water condensation in the space. A sapphire etalon 3 mm thick is used in the cavity to reduce the number of longitudinal modes oscillating. This has a marked effect in reducing laser output linewidth, as will be seen. An aperture (slit) is also used intracavity to restrict the transverse mode structure to TEM_{oo}.

Table 4. Calculated OPO Parameters for Tl_3AsSe_3 and Ag_3AsS_3 for Degenerate Operation at 2.098 μm in the Doubly Resonant (2) System.

Material	d^+(M/V)	θ_m	ρ	B	$\bar{h}_m(B,\xi)$	$\Gamma^2\ell^2$/watt (1 cm)	Thresholds for Confocal Focusing, Loss = a = 0.17/pass			
							cw		Pulsed	
							P_p	P_p/A	P_p	P_p/A
Tl_3AsSe_3	56.4×10^{-12}	31.76°	2.9°	3.05	0.063	15.0×10^{-4}	193 w	0.14 $\frac{Mw}{cm^2}$	2.2 kw	1.55 $\frac{Mw}{cm^2}$
Ag_3AsS_3	20.8×10^{-12}	15.92°	2.7°	2.78	0.068	3.41×10^{-5}	850 w	0.60 $\frac{Mw}{cm^2}$	10.8 kw	7.7 $\frac{Mw}{cm^2}$

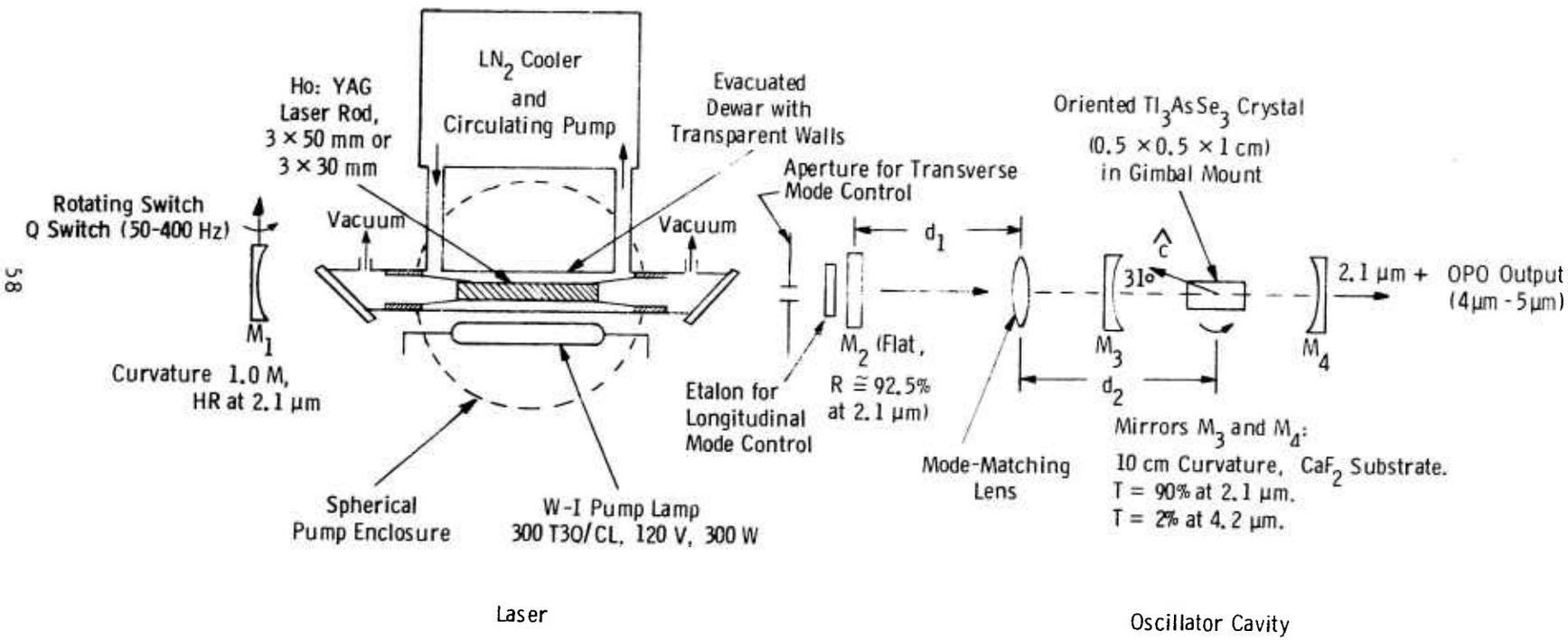

Fig. 24—Schematic diagram of holmium 2 micrometer pumped optical parametric oscillator

Fig. 25. Photograph of laser used for 2 micrometer pumped optical parametric oscillator.

Threshold pump powers required from the tungsten-iodine lamps for this configuration ranged from 100 to 150 watts. Average output powers ranging up to 300 milliwatts TEM_{oo} were attainable, at pulse repetition frequencies of 200 to 300 Hz, implying peak powers of the order of 2.5 to 12 kilowatts for the 150 ns pulse widths used. The pulse widths were measured by frequency doubling the 2.1 μm pulses in a properly oriented Ag_3AsS_3 crystal, and using a fast photomultiplier (2 ns resolution) with S-1 spectral response to measure the width of the 1.05 μm SHG pulses. Suitable corrections were made for the effect of SHG on the temporal pulse shape. With the closed loop liquid nitrogen cooling system, running times of over an hour at 100-200 milliwatt power levels without LN_2 refilling were easily achieved.

Because the laser cavity and OPO cavity lengths cannot be physically made exactly the same, their longitudinal mode structures will be different. Both signal and idler waves must be modes of the oscillator cavity, and oscillation will occur only at frequencies which add up to that of the pump wave, which is a mode of the oscillator cavity. This "cluster effect"[15,24] makes the DRO output highly susceptible to minor disturbances of oscillator or pump cavity spacings, and thus erratic and noisy. We could thus expect erratic oscillator output from this effect.

To reduce this effect, a sapphire etalon was used inside the pump laser cavity to reduce the number of longitudinal modes oscillating. The effect of introducing the etalon is shown in Fig. 26, where the output linewidth of the laser is reduced from 4 Å in the free running case to less than 0.5 Å. Eventually we were able to reduce the linewidth to about 0.22 → 0.4 Å (1.5 GHz → 2.75 GHz) or 0.05 cm^{-1}, corresponding to no more than about 5 to 10 longitudinal modes, at 100 mW output levels.

The extent to which the output frequency spectrum of the pump is effective in driving the oscillator to threshold over its entire output frequency spectrum in the degenerate case can be estimated as follows. The parametric gain of the oscillator depends on momentum mismatch, Δk, as

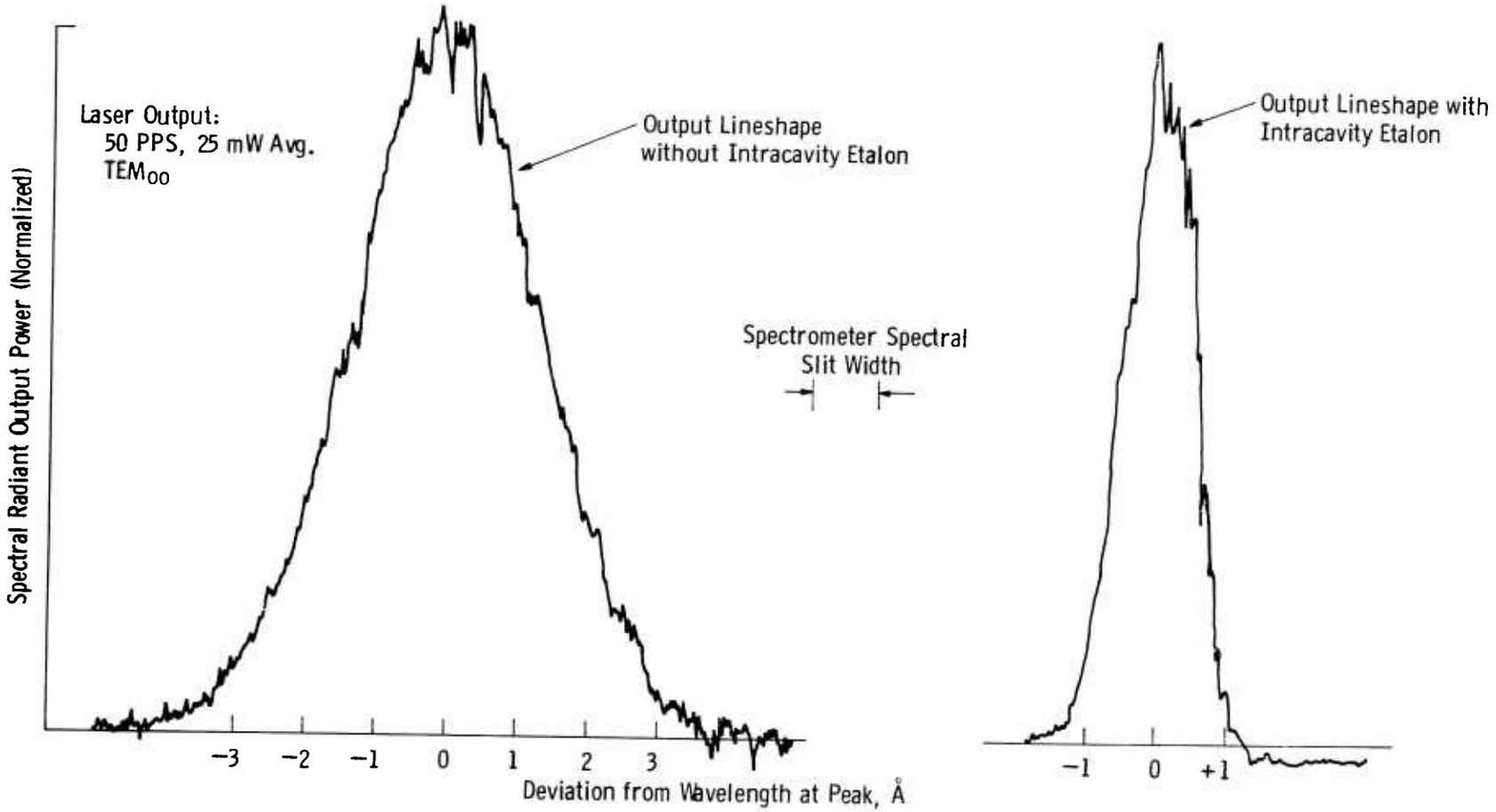

Fig. 26 - Output lineshape of a Q-switched H_o: YAG laser with and without longitudinal mode selection by intracavity etalon

$$\Gamma^2 \ell^2 \approx \frac{\sin^2 \frac{\Delta k \ell}{2}}{\left(\frac{\Delta k \ell}{2}\right)^2}$$

where ℓ is the crystal length. A range of momentum mismatch Δk given by $\Delta k \ell/2 = \pi$ is the width between zeros of the above $\sin^2 x/x^2$ function, i.e., $\Gamma^2 \ell^2$ is appreciable over the range $\Delta k = 2\pi/\ell$. The phase mismatch Δk can be expanded about $\Delta k = 0$ to yield

$$\Delta k = \left(\frac{\partial k_s}{\partial \omega_s} - \frac{\partial k_i}{\partial \omega_i}\right) \delta\omega_i + \frac{1}{2}\left(\frac{\partial^2 k_s}{\partial^2 \omega_s} + \frac{\partial^2 k_i}{\partial^2 \omega_i}\right) \delta^2 \omega_i \quad .$$

At degeneracy, the first term approaches zero, so the above requirements yield for the bandwidth

$$|\delta\omega_i| = |\delta\omega_s| = \left| \ell \left(\frac{\partial^2 k_s}{\partial^2 k_s} + \frac{\partial^2 k_i}{\partial^2 k_i}\right) \right|^{1/2}$$

The denominator can be evaluated from the Sellmeier curves for each material, using $\omega_s = \omega_i$ at degeneracy. For Tl_3AsSe_3, this gives for the oscillator bandwidth at degeneracy $|\delta\omega_s| \tilde{=} 26\ cm^{-1}$. This is much larger than the laser output linewidth of 0.5 cm^{-1} to 0.05 cm^{-1} (Fig.26), hence 100% of the spectral linewidth of the laser should be effective in pumping the oscillator.

6.4 Mode Matching

For optimum transfer of power in the oscillator cavity between pump and the parametrically generated beams, geometric matching of

the mode volume of all three beams is required. We calculate the confocal parameters, b_L and b_0, of laser and oscillator cavities. The laser cavity corresponds to optical system #1 of Table II in the treatment by Kogelnik and Li,[25] with the radius of curvature of the curved mirror R = 100 cm; and its spacing from the flat mirror, d, equal to about 54 cm. Thus $b_L = 2\sqrt{d(R-d)} = 99.7$ cm. The oscillator cavity is a confocal one formed by dielectric coatings on CaF_2 substrates, corresponding to optical system #4 of Ref. 26. The mirror inside radius of curvature is R = 10 cm, the spacing d = R, and the refractive index of CaF_2 is about 1.41 at 4.2 μm and 1.42 at 2.1 μm. We have

$$b_o = \frac{2R_o\sqrt{d(2R_o-d)}}{2R_o+d(n^2-1)} ,$$

$$b_o \ (4.2\ \mu m) = 6.7 \text{ cm}$$

$$b_o \ (2.1\ \mu m) = 6.6 \text{ cm}$$

To match the pump beam into the oscillator cavity, a lens of minimum focal length f_o must be used, where f_o is given by

$$f_o^{\,2} = \frac{1}{4} b_L b_0 \ .$$

In this case, $f_o = 12.9$ cm. The measured focal length of the lens used was f = 15.6 cm. This leads to parameters for spacing of matching lens from laser output mirror, d_1, and spacing of OPO cavity center from the matching lens, d_2, as given by Kogelnik and Li.

$$d_1 = f \pm \frac{1}{2} b_L \sqrt{(f/f_o)^2-1} = (15.6 \pm 33.4) \text{ cm}$$

$$d_2 = f \pm \frac{1}{2} b_0 \sqrt{(f/f_o)^2-1} = (15.6 \pm 2.3) \text{ cm}$$

Choosing the + signs, we find

$$d_1 = 49 \text{ cm}$$

$$d_2 = 18 \text{ cm}.$$

This is the configuration used for the oscillator tests, and it is indicated in the experimental diagram in Fig. 24.

The spot size of the 2.1 μm pump beam in the OPO cavity under these mode matching conditions is

$$w_o^2 = \frac{\lambda b_o}{2\pi} = 6.9 \text{ cm}^2$$

$$w_o = 1.5 \times 10^{-2} \text{ cm}$$

These focusing conditions are modified slightly by the presence of the crystal, which has a high refractive index, in the oscillator cavity. The actual mirror spacing was increased to 12.4 cm to compensate for this.

6.5 Oscillator Pumping Experiments

6.5.1 Tl_3AsSe_3

An overall view of one configuration of the oscillator experiment is shown in Fig. 27 , where the pump laser is on the left, as seen previously in Fig. 25, and the 10 cm oscillator cavity is on the right. The Tl_3AsSe_3 crystal holder, with provisions for rotation and angular orientation of the sample, is mounted between the triangular CaF_2 mirror mounts.

Doubly resonant oscillator pumping experiments were made with several different Tl_3AsSe_3 samples oriented for phase matching and with broadband antireflection coatings for the 2-5 μm spectral region. Since it would have required extensive x-ray orientation work to determine the sample orientation for propagation in the proper direction to give the larger (d^+) effective nonlinear optical coefficient, faces were cut at both $+\theta_m$ and $-\theta_m$ from the crystal c-axis, and pumping experiments were done with beams propagating in both the crystal quadrants allowed by these

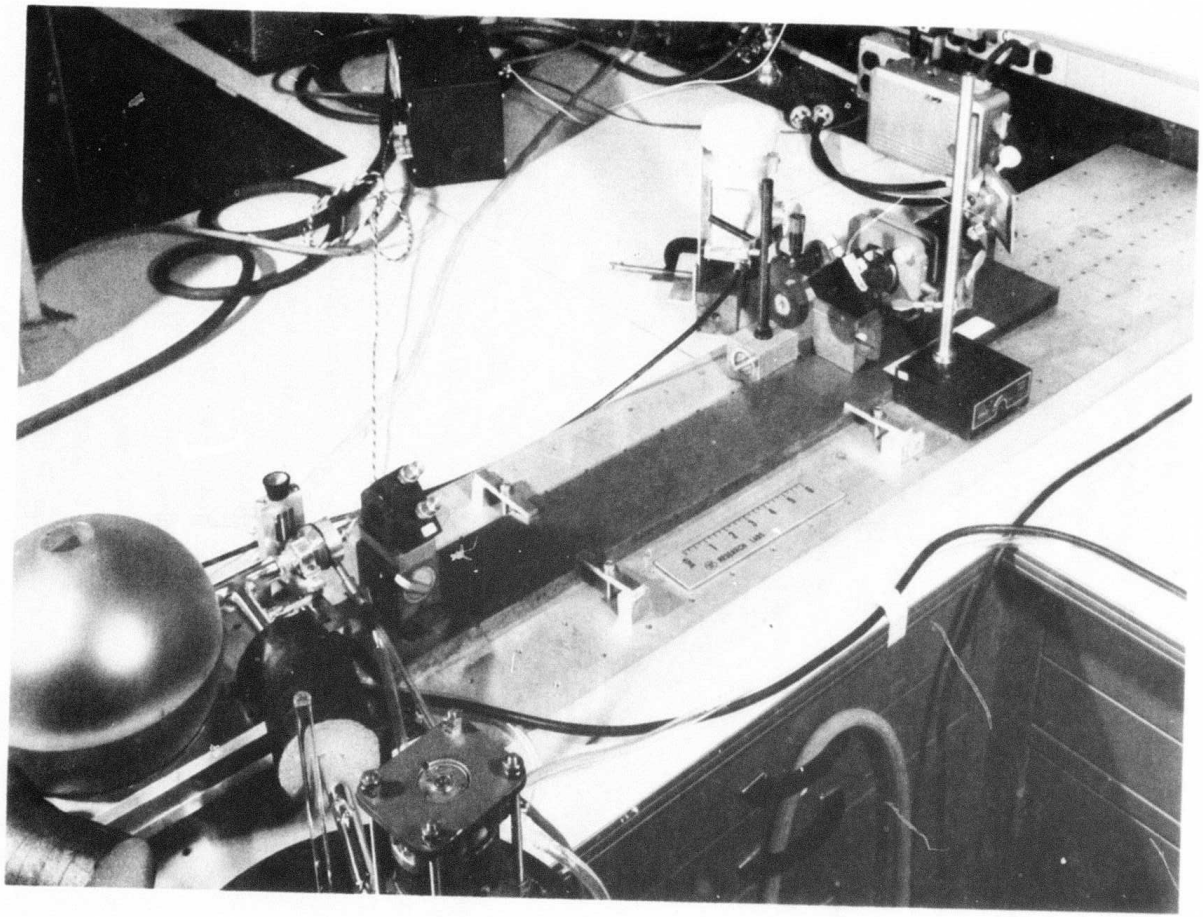

Fig. 27. Overall view of one configuration of the oscillator pumping experiment.

cuts. The same technique had been used on a smaller crystal to measure the ratio $|d^+/d^-|$ in Tl_3AsSe_3 by 10.6 μm SHG.

The oscillator cavity was monitored with either Ge:Au (rise time $\tilde{=}$ 50 ns) or InSb (rise time $\tilde{=}$ 200 ns) detectors, preceded by combinations of long pass infrared filters with high attenuation (at about 1000) at 2.1 μm, and about 50% transmission at 4.2 μm. Thus, oscillator outputs with peak powers of about 1% of the pump power, or of the order of 1-10 watts, would have been observed.

No 4.2 μm output was observed with Tl_3AsSe_3 oscillator crystals, despite the use of pump power densities which damaged the crystals in several cases. The previously measured damage threshold at 2.1 μm for 200 ns pulses was about 10 Mw/cm^2.

6.5.2 Ag_3AsS_3

The sample used in this case was 1.0 cm long, and the phase matching orientation was arranged to be in the d^+ direction by first making 10.6 μm SHG measurements at $\pm\theta_m$ to the c-axis and choosing the cut which gave the largest SHG signal.

In pumping experiments with this sample, the detector signal observed through the long pass filter ($\lambda > 3$ μm) increased by about 100% when the Ag_3AsS_3 sample was in the cavity compared to when it was removed. This was apparently spontaneous parametric fluorescence from the crystal, driven by the 2.1 μm pump. The dependence of this signal on the phase match angle was not critical. When the crystal was rotated in the cavity in attempts to angle phase-match the process, occasional but very erratic large spikes were observed; it was not possible to tune the system accurately to maximize these pulses. It is possible that these were sporadic oscillations at 4.2 μm, generated at random when the proper "cluster" mode configuration of pump and oscillator cavities, along with optimum phase matching was achieved.

7. ACOUSTOOPTIC DEVICE EXPERIMENTS

7.1 Infrared Tunable Acoustooptic Filter

In 1969, on the basis of an analysis of anisotropic Bragg scattering by Dixon,[26] Harris and Wallace[27] proposed the electronically tunable collinear acoustooptic filter, which was later realized for operation in the visible and near infrared using $LiNbO_3$, $CaMoO_4$ or α-SiO_2.[28-30]

The basic operation of the collinear filter can be discussed by noting the behavior of light scattering by acoustic waves in transparent media, as indicated in Fig. 28. In normal Bragg diffraction, light incident as an ordinary ray, with propagation vector $\vec{k}_i^o$, and polarized in the plane of incidence, enters the acoustic column generated in the crystal by the transducer at an angle of incidence θ_i. A portion of the beam is diffracted at angle $\theta_D = \theta_i$, with propagation vector $\vec{k}_d^o$. In isotropic media, the diffracted beam is also polarized in the plane as the incident beam. However, in anisotropic media, the possibility also exists that for certain configurations the scattered beam can have a polarization orthogonal to that of the incident beam. In any case, moments of $\vec{k}_i$ and $\vec{k}_d$ of the incident and scattered beams and pseudomomentum of the interactions acoustic beam $\vec{k}_a$ must be conserved, with

$$\vec{k}_a = \vec{k}_i^o - \vec{k}_d^o$$

in the isotropic case or

$$\vec{k}_a = \vec{k}_i^o - \vec{k}_d^e$$

and

$$\vec{k}_a = \vec{k}_i^e - \vec{k}_d^o$$

Normal Bragg Diffraction

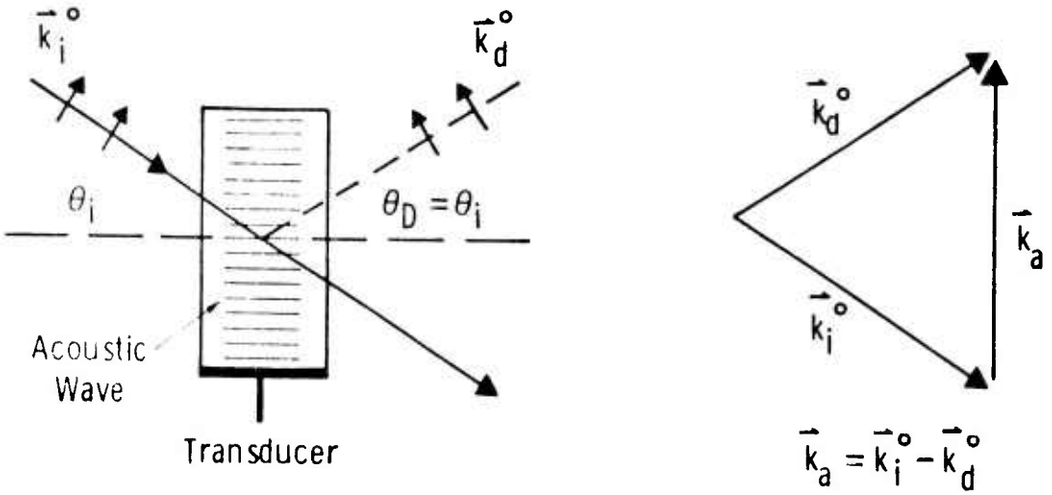

Anisotropic Bragg Diffraction (Negative Uniaxial Crystal)

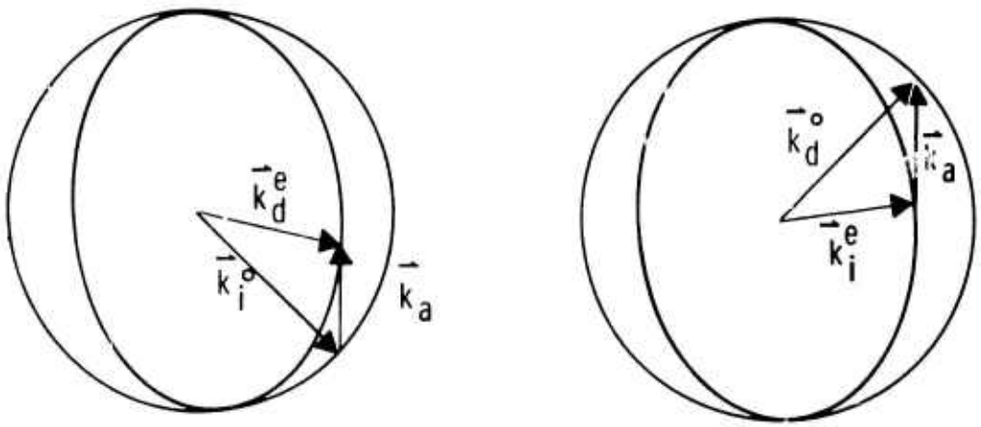

For Collinear Propagation,

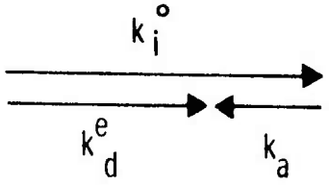

$$k_a = k_i^{\circ} - k_d^{e}$$

For Cumulative Phase Matching, $f_a = \dfrac{V(n_o - n_e)}{\lambda}$

Fig. 28—Behavior of light scattering by acoustic waves in transparent media

in the anisotropic scattering case for a negative uniaxial crystal, as indicated in Fig. 28. In such an anisotropic crystal, the refractive index surface is ellipsoid for the extraordinary ray and a sphere for the ordinary ray. In the special configuration where all three beams are propagated collinearly, normal to the optic axis of the crystal, the vector diagram collapses to a line, and the momentum conservation requirement becomes simply

$$k_a = k_i^o - k_d^e \quad . \tag{13}$$

For cumulative phase matching, if we want this diffraction from the incident to the orthagonal polarization to add up over the entire path length in the crystal, we thus require a one-to-one correspondence between acoustic beam frequency, f_a, and light wavelength, λ, given from Eq. 13, as

$$f_a = \frac{V(n_o - n_e)}{\lambda} \tag{14}$$

where V is the acoustic velocity.

A plot of this theoretical tuning curve for Tl_3AsSe_3 is given in Fig. 29, where the Sellemeier relations and constants of Eqs. 4a,b were used for n_o and n_e. The two points on Fig. 29 indicate the experimentally measured tuning frequencies at wavelengths of 3.39 μm and 5.3 μm for the Tl_3AsSe_3 collinear tunable filter. The experimental configuration used for these measurements is shown in Fig. 30. A polarized input beam is incident from the right on the MgF_2 Rochon prism. A He-Ne laser was used for the 3.39 μm beam, and the frequency-doubled output of a Q-switched CO_2 laser was used for the 5.3 μm signal. The characteristics of the Rochon prism are such that it transmits, undeviated, a beam polarized in the plane of the diagram as shown. This undeviated incident beam then enters the Tl_3AsSe_3 crystal. traversing parallel to the crystal a-axis collinearly with the acoustic beam, which is generated by a $LiNbO_3$ transducer bonded to the end of the crystal. The beam is reflected

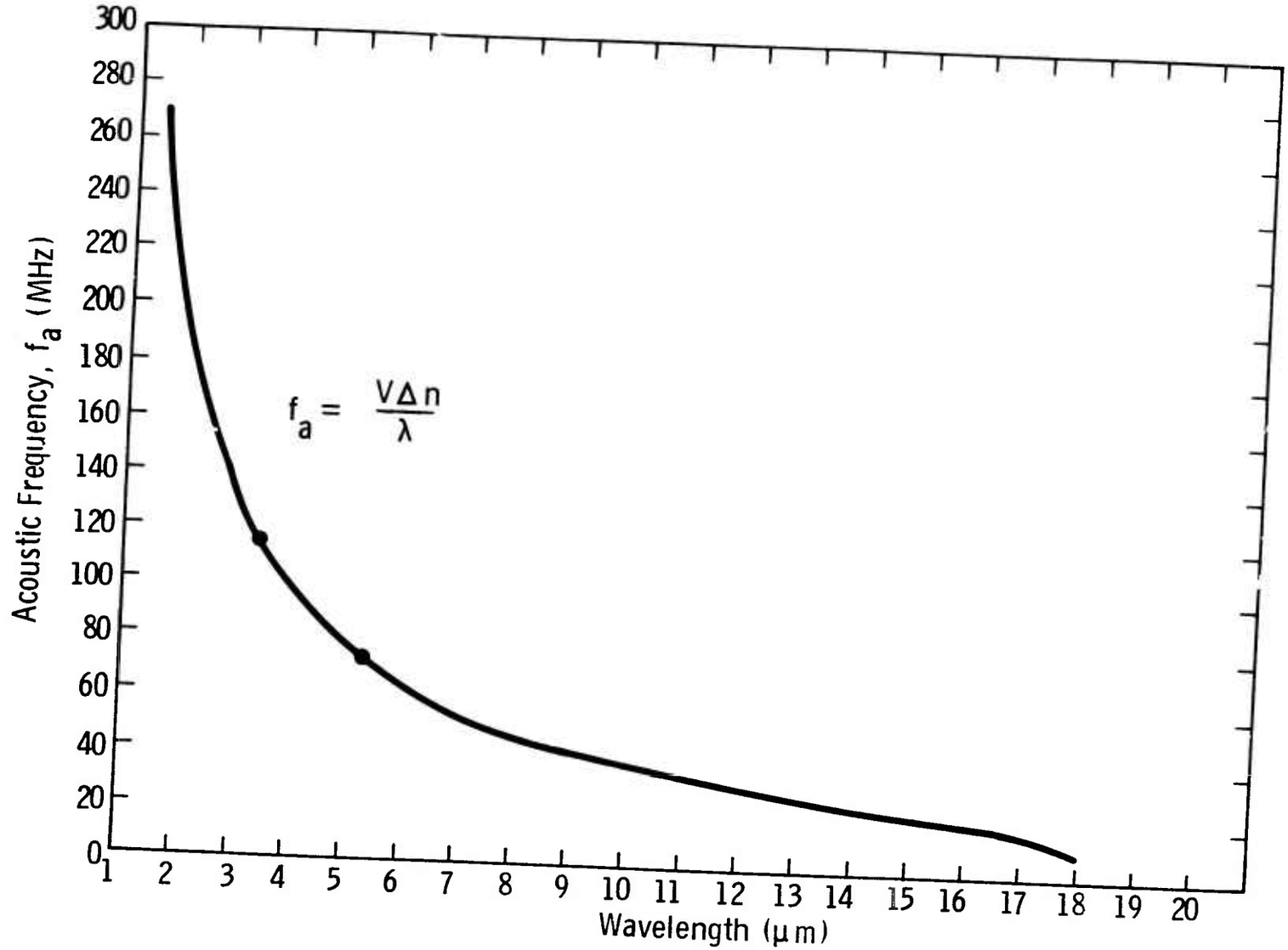

Fig. 29-Theoretical tuning curve for a collinear tunable acoustooptic filter based on Tl_3AsSe_3

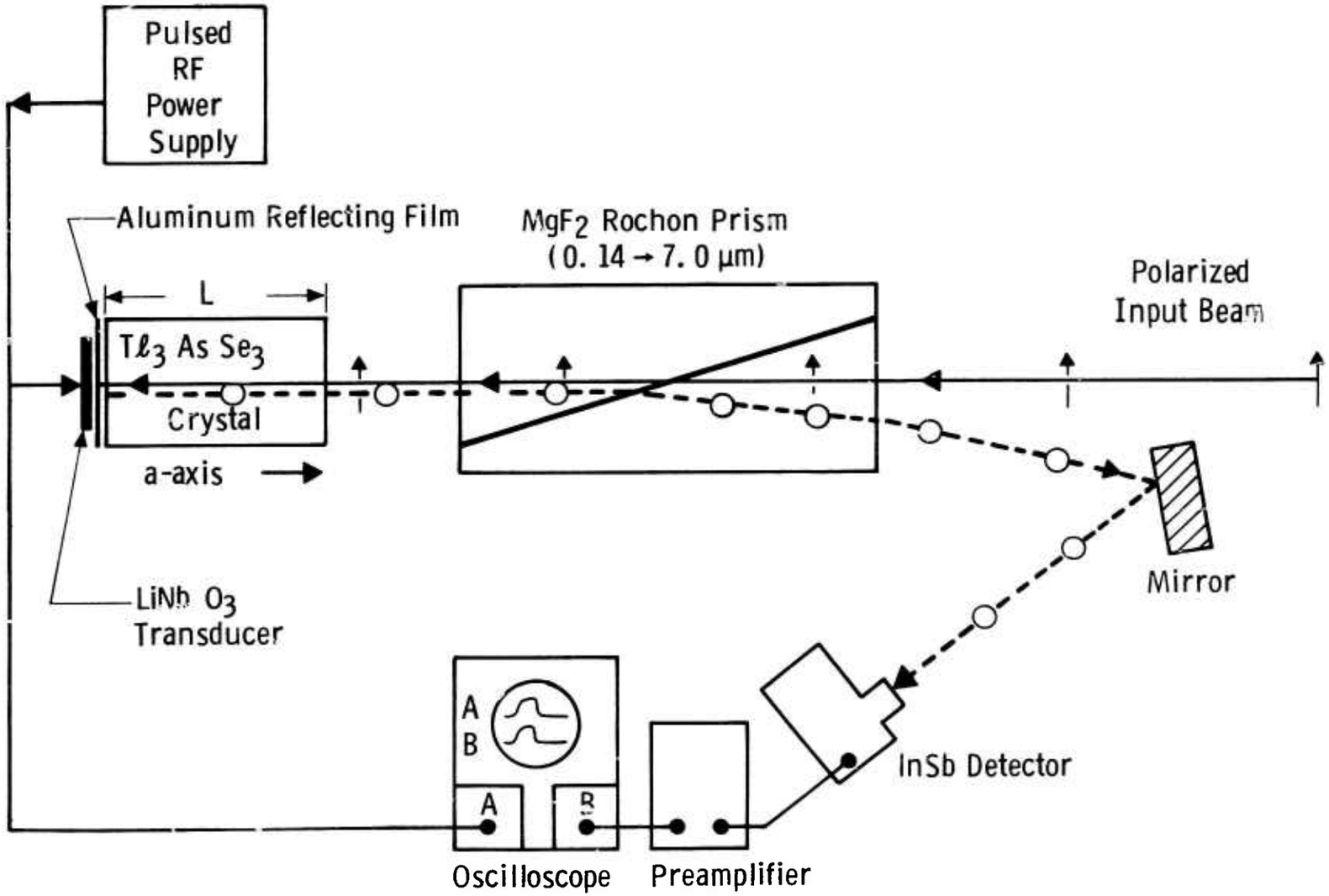

Fig. 30—Experimental set up for an infrared tunable acoustooptic filter using $T\ell_3AsSe_3$

from an aluminum film deposited on the polished Tl_3AsSe_3 crystal face to which the $LiNbO_3$ transducer is bonded. After reversing its direction, the optical beam continues to interact with the collinear acoustic beam, during which interaction the light is scattered from the initial polarization into the orthogonal polarization, if the acoustic frequency is tuned to meet the phase matching requirement (Eq. 14). The light beam then again enters the Rochon prism, where the fraction which has been scattered into the orthogonal polarization is deviated from the initial path by a few degrees. This component is then picked off with a mirror, from which it is reflected to an appropriate detector. In some cases, the detector was preceded by infrared filters and/or wire grid polarizers to insure that the signal was at the correct wavelength and of the proper polarization.

For the measurements at 3.39 μm, the He-Ne laser used was operated cw, and the acoustic transducer was driven either continuously or a pulsed mode. In the case of measurements at 5.3 μm, the CO_2 laser at 10.6 μm was Q-switched and the second harmonic consisted also of short pulses at about a 370 Hz PRF, so it was necessary to synchronize the RF pulses to the Tl_3AsSe_3 filter with the laser pulses. This was done by reflecting an alignment laser beam from the rotating mirror of the CO_2 laser, detecting this reflected beam with a photomultiplier, and using the photomultiplier output to trigger the RF pulse generator. Synchronism to within about 100 ns was achieved in this way, which was more than adequate because the acoustic pulse lengths required to fill the entire length of the crystal with sound were of the order of 12-15 μsec.

Harris showed that the acoustic power density required to scatter 100% of the polarized incident beam into the opposite polarization and thus achieve 100% transmission of the filter for a polarized input beam at wavelength λ_o is given by

$$\frac{P_A}{A} = \left[\frac{\rho V^3}{n_o^3 n_e^3 |p_{41}|^2}\right] \frac{\lambda_o^2}{2L^2} \qquad (15)$$

Here, the brackets enclose the relevant materials parameters; ρ is the density, V the acoustic velocity, n_o and n_e the ordinary and extraordinary refractive indices, and p_{41} the photoelastic coefficient involved in the anisotropic Bragg scattering process. In Eq. (15), the combination of materials parameters

$$\left[\frac{\rho V^3}{n_o^3 n_e^3 |p_{41}|^2}\right]$$

is approximately the same as $1/M_2$, where M_2 is an acoustooptic figure of merit describing the efficiency with which a given material can deflect light when used as an acoustooptic modulator.[31]

With respect to use in the collinear acoustooptic filter, only certain crystal classes process the proper elements of the photoelastic tensor and at the same time allow propagation of the sound wave in an acoustically isotropic direction.[30] Among uniaxial crystals, the usable point groups are 32, 3 m, $\bar{3}$ m, 4, 41 m, $\bar{4}$, and 6, $\bar{6}$, 6 m. From Eq. (15) and the definition of M_2, it is clear that materials with a large acoustooptic figure of merit M_2 will make efficiency collinear acoustooptic filters. Also to be noted from Eq. (15) is the fact that the required acoustic power density for 100% transmission at λ_o increases as λ_o^2. Since a limit exists to the acoustic power density which can be applied to a crystal before heating occurs, along with attendant thermal optical distortion and eventual damage, extension of collinear filter operation into the infrared has proven to be difficult.

The properties of the four single crystal materials in which tunable collinear filter operation has now been demonstrated are summarized in Table 5. We see that by virtue of the fact that it possesses a high refractive index and low acoustic velocities, Tl_3AsSe_3 has a high acoustooptic figure of merit, M_2. A clear advantage for Tl_3AsSe_3 in the infrared is also its transparency range, which extends to 18 μm, where as α-SiO_2 is limited to about 2 μm, and $LiNbO_3$ and $CaMoO_4$ to 4.5 μm. In actual practice, tunable filter operation has been observed only out to about 3 μm in $CaMoO_4$ and $LiNbO_3$. Another severe problem begins to occur

TABLE 5. COMPARISON OF MATERIALS FOR COLLINEAR TUNABLE FILTERS

Material (Point Group)	Useful Optical Transparency Range	Refr. Index (2 μm) η	Biref. $\Delta\eta$	Photoelastic Coefficient $\lvert r_{41} \rvert$	Density ρ gm/cm^3	Acoustic Velocities V_L V_S $\left(\frac{cm}{sec}\right)$	Accustooptic Figure of Merit, $M_2 = n^6 p^2 / \rho V^3$	Estimated Required Power Density for T = 100% (L=4 cm, λ_0=2 μm)	Demonstrated Tuning Range
$\alpha - SiO_2$ (32)	0.2 – 2 μm	1.52	0.01	0.041	2.65	5.75×10^5 3.36×10^5	1 5	7,500 mw/mm^2 (Long.)	0.2 → 1 μm
$CaMoO_4$ (4/m)	0.4 – 4.5 μm	1.95	0.01	0.1	4.26	6×10^5 2.95×10^5	14 118	500 mw/mm^2 (Shear)	0.5 → 3 μm
$LiNbO_3$ (3m)	0.4 – 4.5 μm	2.2	0.09	0.155	4.64	6.57×10^5 4×10^5	49 217	350 mw/mm^2 (Shear)	0.4 → 3 μm
Tl_3AsSe_3 (3m)	1.27 – 18 μm	3.3	0.18	>0.1	7.83	2.14×10^5 1.0×10^5	>500	5 mw/mm^2 (Long.)	3.39 μm, 5.3 μm

in $CaMoO_4$ as λ_o is increased; here because of the small birefringence (0.01), the required acoustic frequency f_a becomes very low at large λ_o. Severe problems of diffraction of the acoustic beam are then experienced.

The results of tunable collinear acoustooptic filter tests on Tl_3AsSe_3 crystals are shown in Table 6.

TABLE 6. Tl_3AsSe_3 COLLINEAR TUNABLE ACOUSTOOPTIC FILTER RESULTS

λ_o	Crystal Length L	Peak Transmission at λ_o	P_A/A Required	Filter Bandwidth
3.39 μm	0.8 cm	20%	60 $\frac{mw}{mm^2}$ (cw)	2 cm^{-1}
3.39 μm	1.4 cm	Not Measured	Pulsed; Not Measured	2 cm^{-1}
5.3 μm	1.4 cm	10%	Pulsed; Not Measured	2 cm^{-1}

This represents collinear tunable filter operation at the longest wavelengths so far attained. The power density of 60 mw/mm^2 quoted for 20% transmission at 3.39 μm is considerably higher than the value calculated assuming $p_{41} \tilde{=} p_{31} \tilde{=} 0.15$ (see Fig. 31). However, the actual power density in the crystal was very difficult to measure accurately because the coupling efficiency from the $LiNbO_3$ transducer to the Tl_3AsSe_3 was not known accurately, and in addition the transducer used was cut for 40 MHz, but operated on its 3rd harmonic in order to generate a signal at 115 MHz for tuning at 3.39 μm. As a rough estimate, for a given transducer the power generated at the third harmonic would be about 20 db below that at the fundamental. The estimated 60 mw/mm^2 is a conservatively high value for the power density required at the 20% filter transmission value at 3.39 μm. Using it, we can calculate the effective value of p_{41}.

The transmission of the filter is given by[27]

$$\frac{P_x(L)}{P_z(0)} = \sin^2 \Gamma L \qquad (16)$$

where

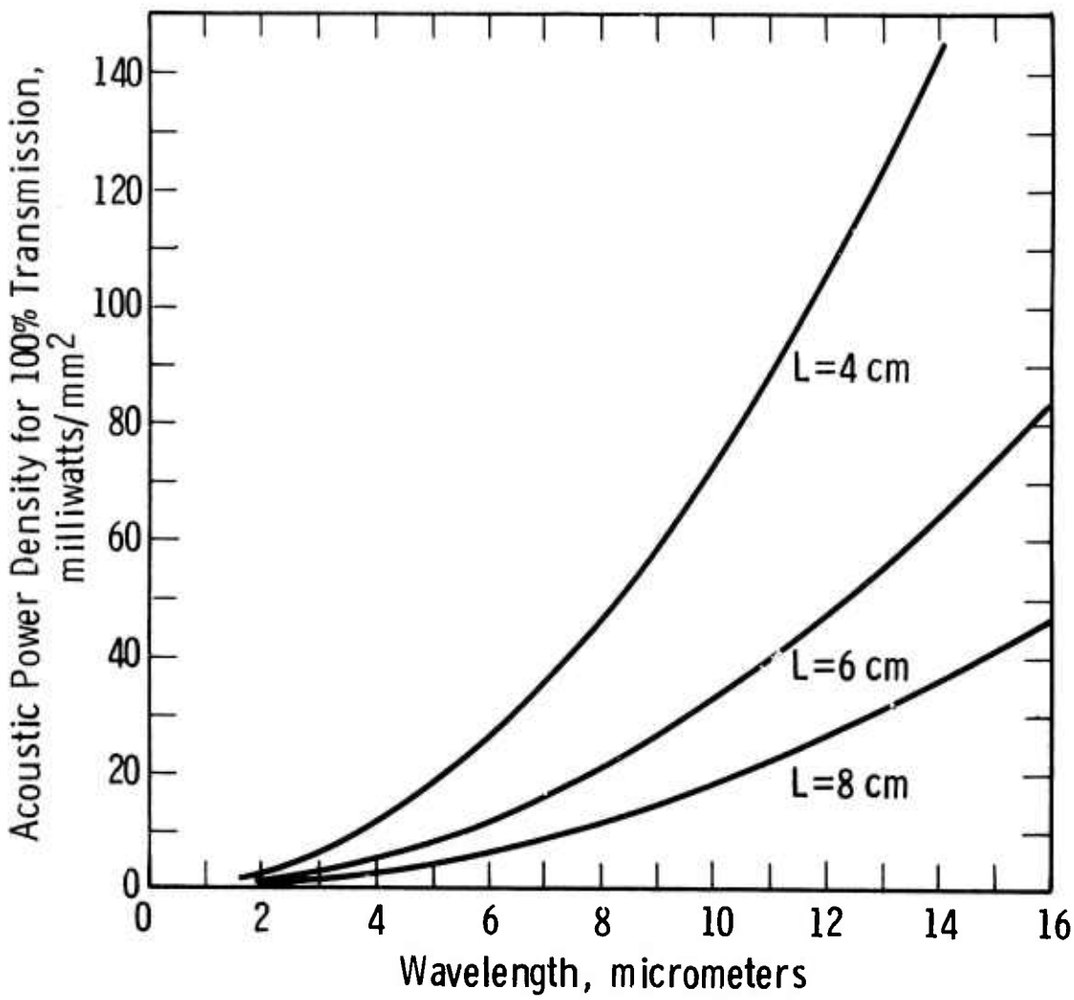

Fig. 31—Acoustic power density vs wavelength for Tl_3AsSe_3 crystals of various lengths

$$\Gamma = \left[\frac{n_o^3 n_e^3 p_{41}^2 \pi^2}{2\lambda_o^2 \rho V^3} \frac{P_A}{A}\right]^{1/2} \tag{17}$$

and L is the effective length of the filter. In our reflective mode filter, this is twice the crystal length. $P_x(L)$ is the power in the orthogonal polarization after traversing a length L, and $P_z(0)$ is the power at the incident polarization upon entering the crystal. Thus,

$$p_{41} = \frac{1}{\pi(2L_c)} \left[\frac{2\lambda_o^2 \rho V^3}{n_o^3 n_e^3 \left(\frac{P_A}{A}\right)}\right]^{1/2} \sin^{-1} \frac{P_x(L)}{P_z(0)} \tag{18}$$

with the experimental values $2L_c$ = 1.6 cm, $P_x(L)/P_z(0)$ = 0.2, and P_A/A = 60 mw/mm^2 = 6 x 10^7 erg/cm^{2}sec, we find

$$p_{41}(Tl_3AsSe_3) \tilde{=} 0.05 \quad .$$

Although this is a reasonable value for p_{41} in comparison with other materials, it cannot be considered definitive. More accurate measurements must be made using comparison techniques like those of Dixon and Cohen,[32] where the acoustic power density does not enter directly.

The calculated acoustic power density P_A/A required in Tl_3AsSe_3 for 100% peak transmission at various wavelengths λ_o is shown in Fig. 31, where crystal length has been used as a parameter. Here, we have used a value $p_{41}(Tl_3AsSe_3)$ = 0.16, considerably larger than that above, but still typical of values for p_{41}. It is apparent from Fig. 31 that tunable filter operation well beyond 10 μm will be possible with reasonably low acoustic power densities will be possible with Tl_3AsSe_3 crystals of lengths of the order of 4 to 8 centimeters.

The shape of the filter passband exhibits the typical $\sin^2 x/x^2$ dependence on phase mismatch existing in many optical parametric processes. It can be shown that the full width at half maximum of the filter transmittance is given by

$$\Delta y \cong \frac{5}{bL} \quad ,$$

where y is the deviation from center b, L is the length of the crystal in cm, and

$$b \equiv \left[\frac{\partial k_o}{\partial y} - \frac{\partial k_e}{\partial y}\right]$$

is the so-called dispersive constant[27] of the material.

Since $k_o = \frac{2\pi n_o}{\lambda_o} = 2\pi ny$, b can be written

$$b = 2\pi\left[(n_o - n_e) + y\,\frac{\partial(n_o - n_e)}{\partial y}\right] \quad . \tag{19}$$

With the Sellmeier equations for Tl_3AsSe_3 (Eq. 4), one can show that the second term in Eq. (19) is very small, and that an error of less than 3%, is involved in approximating

$$b \cong 2\pi(n_o - n_e)$$

for all wavelengths.

With this, the bandwidth expression becomes

$$\Delta y \cong \frac{5}{2\pi\Delta nL}\ \text{cm}^{-1} \quad . \tag{20}$$

A plot of this calculated filter bandwidth for several crystal lengths, vs. wavelength of peak transmission is shown in Fig. 32. The bandwidths range from 2 Å to about 300 Å over the range from 2 to 16 μm.

A direct measurement of filter bandwidth was not made, but the measurements at 5.3 μm give some verification of the filter bandwidth by virtue of its resolution of t separation of the frequency-doubled CO_2 laser vibration-rotation lines. The calculated FWHM of the 1.4 cm long filter at 5.3 μm is

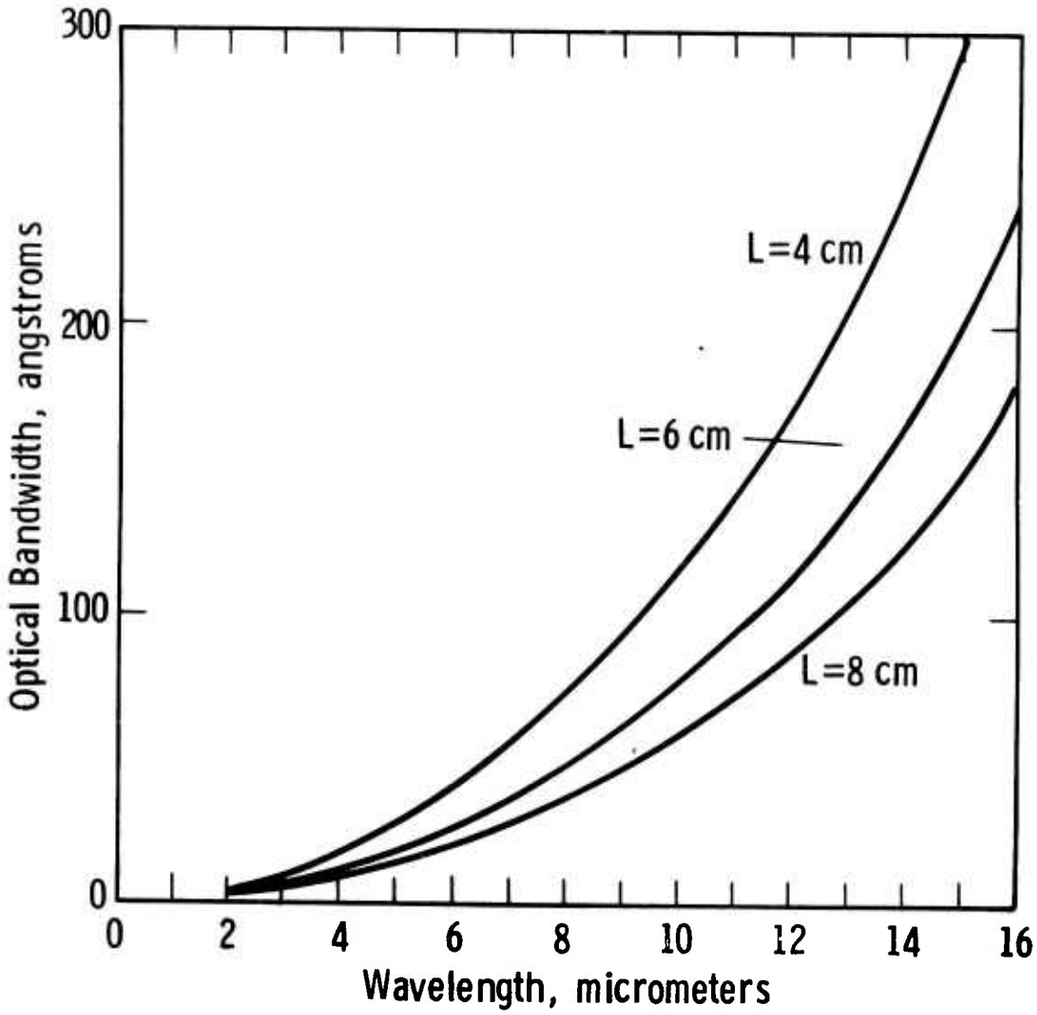

Fig. 32—Calculated filter bandwidth for several Tl_3AsSe_3 crystal lengths vs wavelength of peak transmission

$$\Delta y = \frac{5}{2\pi(\Delta n)L} = 3.19 \text{ cm}^{-1} \quad .$$

The CO_2 laser oscillates on several vibration-rotation transitions, with typical frequencies being listed in Table 7.

It can be seen from Table 7 that the individual vibrational-rotational transitions in the CO_2 laser, as frequency doubled will be spaced about 3 cm^{-1} apart and should just begin to be resolved by the Tl_3AsSe_3 filter, with its 3.19 cm^{-1} resolution. The highest gain transitions in the CO_2 laser lie in the P-branch manifold, so it is most likely that these are the ones oscillating in our CO_2 laser.

The output line structure of the frequency doubled CO_2 laser, as determined by scanning the acoustic frequency applied to the Tl_3AsSe_3 filter, is shown in Fig. 33. It appears that the filter is, as expected, just able to resolve individual vibrational-rotational transitions. Tuning between peaks appears to require a frequency change of the order of 100 kHz in the acoustic signal, implying that the filter tuning rate is about 30 cm^{-1}/kHz. This corresponds fairly well with the calculated rate

$$\frac{\Delta y}{\Delta f_a} = \frac{2\pi}{bV} = \frac{1}{(n_o - n_o)V} = \frac{1}{(.1784)(2.1\ 10^5 \text{ cm/sec})}$$

$$= \frac{27 \text{ cm}^{-1}}{\text{MHz}} \quad .$$

The filter bandwidth is, according to Eq. (20), inversely proportional to the crystal length L, but L is the effective length, i.e., that length of the crystal which is filled with sound. If the system is used in the pulsed mode, then as the pulse length is varied below the value 2L/V = 13 μs, the effective length of the crystal can be shortened, and the filter bandwidth decreased electronically. The effects of such pulse length charges on bandwidth are shown in Fig. 34, where the all experimental parameters are the same as in Fig. 35, but the acoustic pulse length is successively shortened to 10 μs and 8 μs.

TABLE 7. OUTPUT FREQUENCIES OF CO_2 LASER

Transition	Frequency (THz)	Doubled Frequency		Corresponding f_a of Tl_3AsSe_3 Filter
		(THz)	(cm^{-1})	
P_{16} (Δ)	28.412590	56.82518	1895.4837 (3.52 cm^{-1})	72.7032 MHz (135.2 kHz)
P_{18} (Δ)	28.359774	56.719548	1891.9602 (3.57 cm^{-1})	72.5680 MHz (137 kHz)
P_{20} (Δ)	28.306225	56.61245	1888.3878 (3.62 cm^{-1})	72.4310 MHz (139 kHz)
P_{22}	28.251942	56.503884	1884.7664	72.2921 MHz
R_{24} (Δ)	29.333860	58.667721	1956.944 (2.52 cm^{-1})	75.06055 MHz (96.53 kHz)
R_{22} (Δ)	29.296136	58.592271	1954.428 (2.55 cm^{-1})	74.96402 MHz (97.83 kHz)
R_{20} (Δ)	29.257658	58.515316	1951.877 (2.63 cm^{-1})	74.86619 MHz (101 kHz)
R_{18}	29.218430	58.436860	1949.244	74.76519 MHz

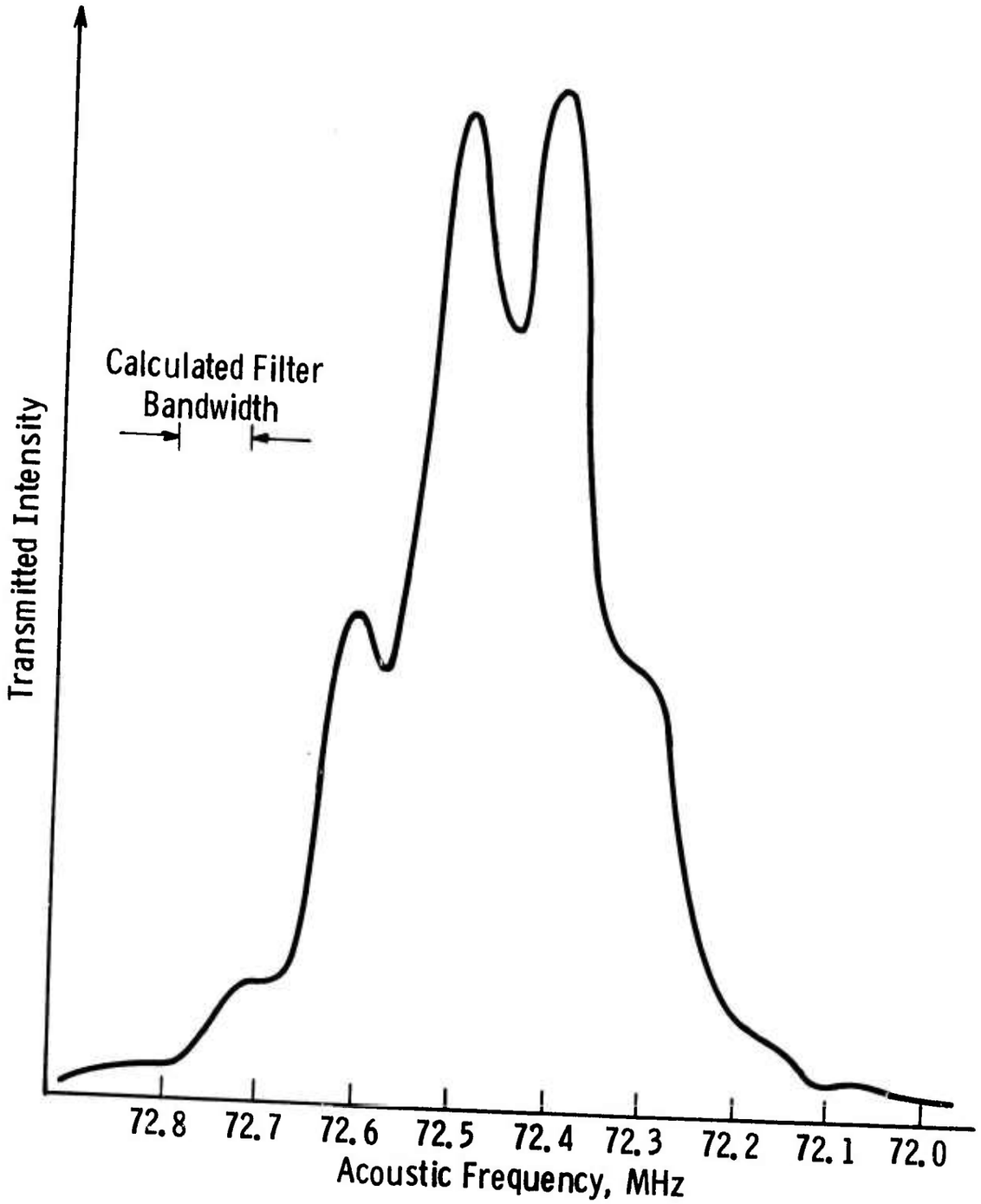

Fig. 33 - Transmitted intensity vs applied acoustic signal frequency
Source: Frequency doubled CO_2 laser at 5.3 μm

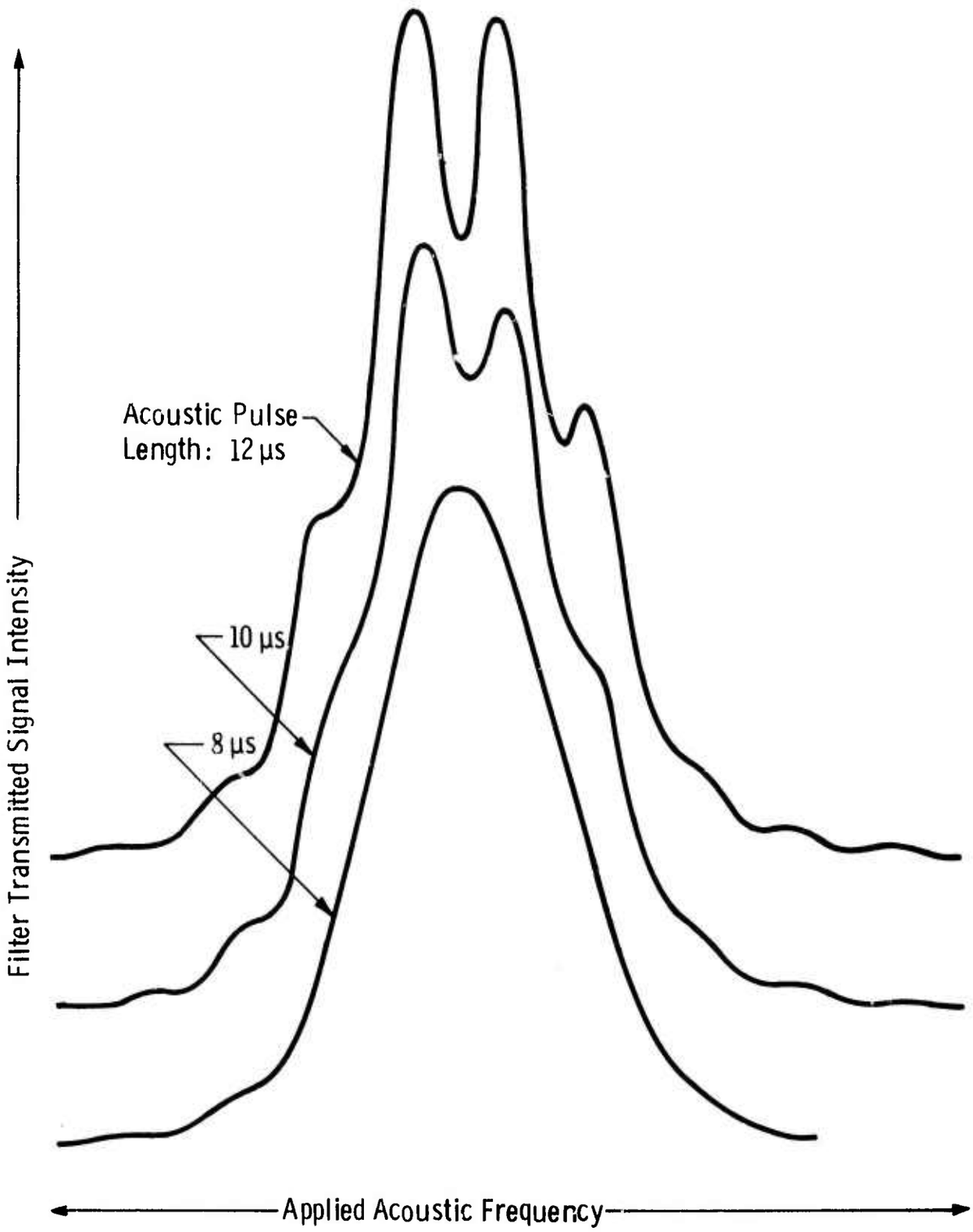

Fig.34 - Effect of changes in applied acoustic pulse length on filter resolution at 5.3 μm

The fine structure of the individually resolved lines gradually disappears as the bandwidth is increased.

The results of the work on acoustooptic filter applications indicate that Tl_3AsSe_3 can be successfully used at much longer infrared wavelengths than the other three materials in which collinear tunable acoustooptic filter action has so far been observed. Potential devices based on this include electronically tunable infrared prefilters for communications or optical processing and countermeasures applications, or to compact, electronically tunable infrared spectrometers.

7.2 Intracavity Q-Switching with Tl_3AsS_4

The high refractive indices and low acoustic velocities of the sulfosalt materials indicate that they would be useful as efficient acoustic modulators and Q-switches, requiring low RF acoustic drive powers. Successful intracavity operation, however, depends on insuring that the crystal insertion loss is low enough to allow laser action to take place. The results obtained here indicate that the optical quality of Tl_3AsS_4 can be made good enough for this purpose, and that suitable antireflection coatings can be applied to Tl_3AsS_4 so that it can be used as a modulator inside infrared laser cavities without problems due to reflection losses. A problem still to be solved satisfactorily, however, is that of reducing acoustic pulse echo trains, which interfere with the main pulses and cause the system to revert to a free-running condition. An inherent restriction to low pulse repetition frequencies and possibly low pulse energies will exist because of the low acoustic velocities.

For Bragg scattering at an optical wavelength λ by an acoustic beam of wavelength Λ, the scattering angle is

$$\theta = \frac{\lambda}{\Lambda} = \frac{f_a}{V}\lambda \ ,$$

where f_a is the acoustic frequency and V the velocity. For simplicity, we chose to use longitudinal waves in Tl_3AsS_4, at f_a = 40 MHz. For this, $V = 2.15 \times 10^5$ cm/sec, thus for λ = 2.1 μm (Ho:YAG laser),

$$\theta = 2.24° \quad .$$

This relatively large angle indicates that effective intracavity modulation should be possible, provided a large enough fraction of optical power can be scattered from the beam.

The fraction, f, of incident light scattered from the light beam in a single pass through the modulator is, in the approximation of small scattering, given by[33]

$$f \cong \left(\frac{\pi^2 d^2 n^6 p^2}{2\lambda^2 \rho V^3}\right) \frac{P}{A} \quad ,$$

where d is the length of the interaction region between light and acoustic beams, p is the relevant photoelastic coefficient, P the acoustic power coupled into the crystal, A the transducer area, etc. Note that as in the collinear acoustooptic filter case, the deflected signal is proportional to the figure of merit $M_2 \equiv n^6 p^2/\rho V^3$.

Two Tl_3AsS_4 samples of good optical quality with dimensions approximately 2 x 5 x 8 mm were used in the experiments; the large faces were antireflection coated, and the optical path thickness was small, d = 0.2 cm. With the refractive index n(2.1 μ) = 2.6, V = 2.15 x 10^5 cm/sec, and ρ = 6.2 gm/cm^3, and assuming a value of p = 0.9 for the photoelastic coefficient,[34] the fraction of light deflected at 2.1 μm becomes

$$f = 0.0182 \frac{P_A}{A} \text{ , with } \frac{P_A}{A} \text{ in watts/cm}^2 \quad .$$

A 1 watt/cm^2 (10 mw/mm^2) power density would thus introduce a one-way power loss of 1.8% into the cavity. Power densities up to 2000 mw/mm^2 were readily applied to the $LiNbO_3$ transducer, and estimated coupling efficiencies were about 15 db, so the actual acoustic power densities ranged up to about 60 mw/mm^2.

Both PbF_2 and NdF_3 were found to be suitable single layer antireflection coating materials for Tl_3AsS_4 at 2.1 μm; the reflectivity

at 0.53 μ was monitored during the deposition process to provide indication of when a λ/4 thickness at 2.1 μm was reduced. NdF_3 yielded the more stable coatings. Reflection loss per surface was reduced from 20% to considerably less than 4% by the application of the coatings.

A photograph of a Tl_3AsS_4 modulator mounted in the Ho:YAG laser optical cavity is shown in Fig. 35. The Tl_3AsS_4 crystal is mounted on a vertical plate attached to the aluminum rod placed between the laser output mirror and the spherical pump cavity. Fine wire leads from the transducer, which is cemented to the crystal with phenyl salicylate, extend to a BNC connector near the bottom of the post. RF drive power at 40 MHz is supplied by a Hewlett Packard HP 608 Signal Generator. The output of this signal generator is normally on, and is amplified to power levels of up to 200 mw by an EN1310L power amplifier.

A pulse generator is used to externally modulate the HP608, switching the output off to cut off the acoustic power in the cavity and allow the laser pulse to build up.

Figure 36 shows the output of the Ho:YAG laser as acousto-optically Q-switched by the Tl_3AsS_4 modulator. The upper trace is the laser output pulse train, and the lower trace is the envelope of the RF signal, showing the coincidence of the laser output pulses with the turn-off of RF power applied to the crystal. The transition of the temporal behavior of the laser output from the random-spiking free-running mode to controlled Q-switching is shown in Fig. 37. In the upper trace, the modulator crystal is in the cavity and the laser is above threshold, but no RF power is applied to the Tl_3AsS_4 crystal. The laser output consists of random bursts of wide pulses (> 50 μs), with random peak powers. In the lower trace, pulsed RF power has been applied and the transition to the Q-switched mode made. The pulses are much narrower (∿ 200 ns), and peak powers considerably higher (the vertical gain sensitivity in the two traces is not calibrated, but is orders of magnitude more sensitive in the top trace than in the bottom. The Q-switched peak powers are not uniform; this is a result of several factors. If the Q-switch does

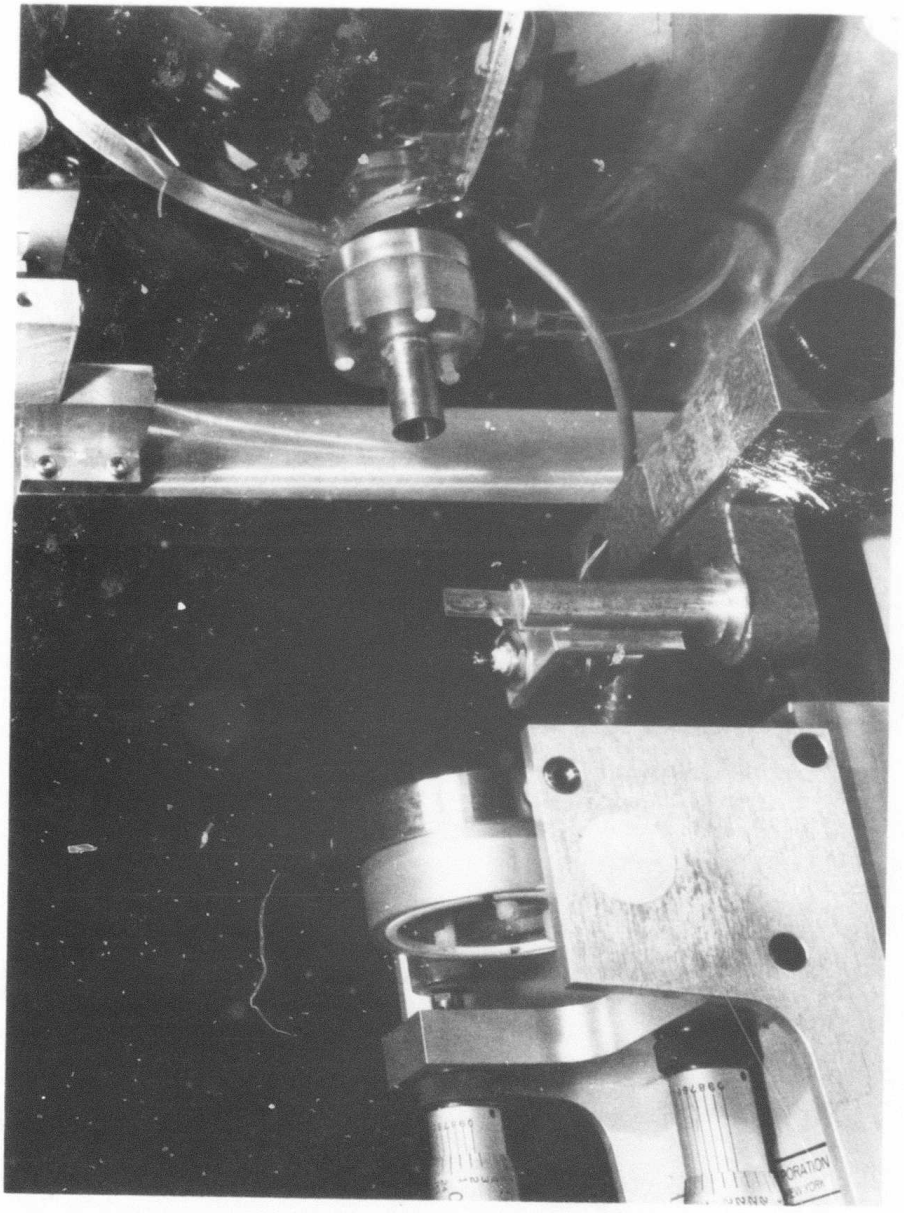

Figure 35. Tl_3AsS_4 Acoustooptic Modulator Mounted In Cavity Of Ho:YAG Laser.

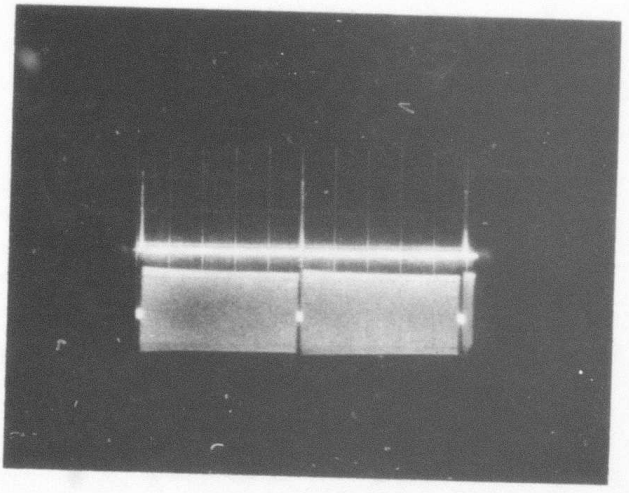

Fig. 36. Synchronization of Q-switched output pulses with RF power applied to Tl_3AsS_4 intracavity acousto-optic modulator. Sweep speed 200 μs/cm.

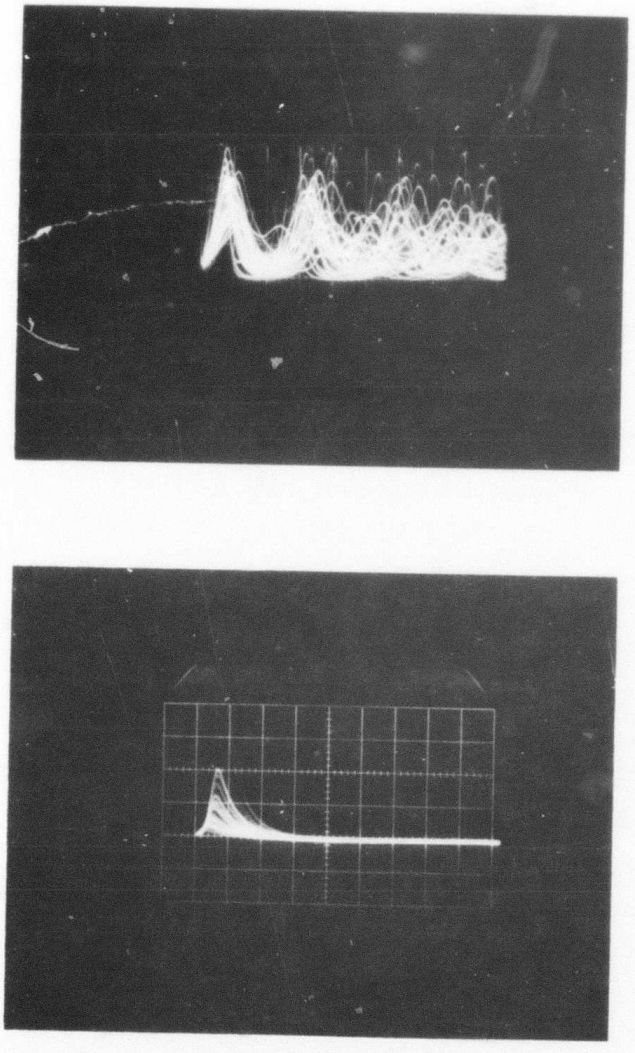

Fig. 37. Transition from free-running to Q-switched output when pulsed RF power is applied to Tl_3AsS_4 intracavity acousto-optic modulator.
Sweep speeds: Upper trace, 50 μs/cm. Free running.
Lower trace, 500 μs/cm. Q-switched.

not open fast enough, the laser pulse will develop slowly and not completely; the population inversion will not be depleted, and enough gain will remain for a small "after pulse" to develop. Mechanical noise, for instance from turbulent flow of the coolant, can cause pulse fluctuations. Acoustic power reflected back from an edge of the crystal into the interaction region can cause time dependent losses which affect the gain and energy output per pulse. This can be reduced somewhat by applying sound absorbent materials to the non-optical crystal surfaces, but we were unable to find a completely suitable material for this.

In Fig. 38 is shown a superposition of several successive Q-switched output pulses with the switching at a 600 Hz rate. Average output power was 80 milliwatts, and pulse peak power was about 650 watts.

Plots of average power vs. pulse repetition frequency and peak power vs. pulse repetition frequency are shown in Figs. 39 and 40. Theoretically, average output power should increase roughly exponentially to a saturation value close to the maximum cw power as the PRF is increased. Instead, we see the beginning of this increase, then a distinct drop at PRF's in excess of about 300 Hz. The peak power per pulse should exhibit an exponential decrease with increasing PRF. We see instead of this exponential behavior a sudden drop at about 300 Hz. Similar dramatic changes have been observed in Ho:YAG lasers Q-switched at high PRF's by a rotating mirror system; it is not clear what the mechanism for this might be. Operation at power levels closer to threshold in some cases yields output characteristics more like those expected, as shown in Figs. 41 and 42. Here, average power and pulse peak power vs. PRF are plotted for conditions in which the laser input pump power is 124 watts, just 10% above the threshold value of 112 w. The acoustic power applied to the transducer is 110 mw, with an estimated 22 mw/mm^2 power density in the modulator crystal.

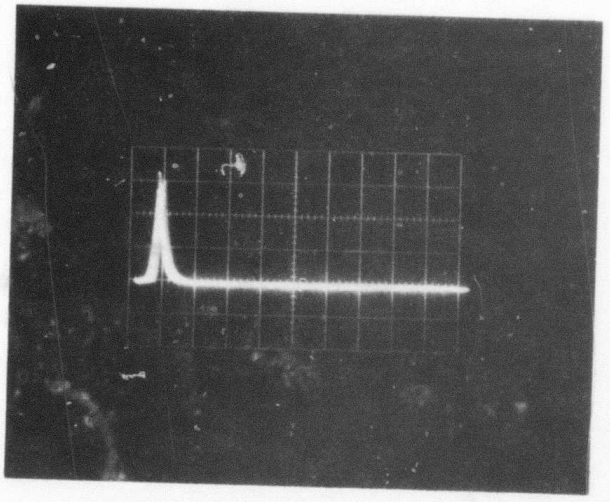

Fig. 38. Output pulses from a Ho:YAG laser internally Q-switched by a Tl_3AsS_4 acousto-optic modulator. Several pulses are superimposed. Laser operating 30% above threshold. PRF 600 Hz. Sweep speed 10 μs/cm. Peak power about 0.1 → 1 kw.

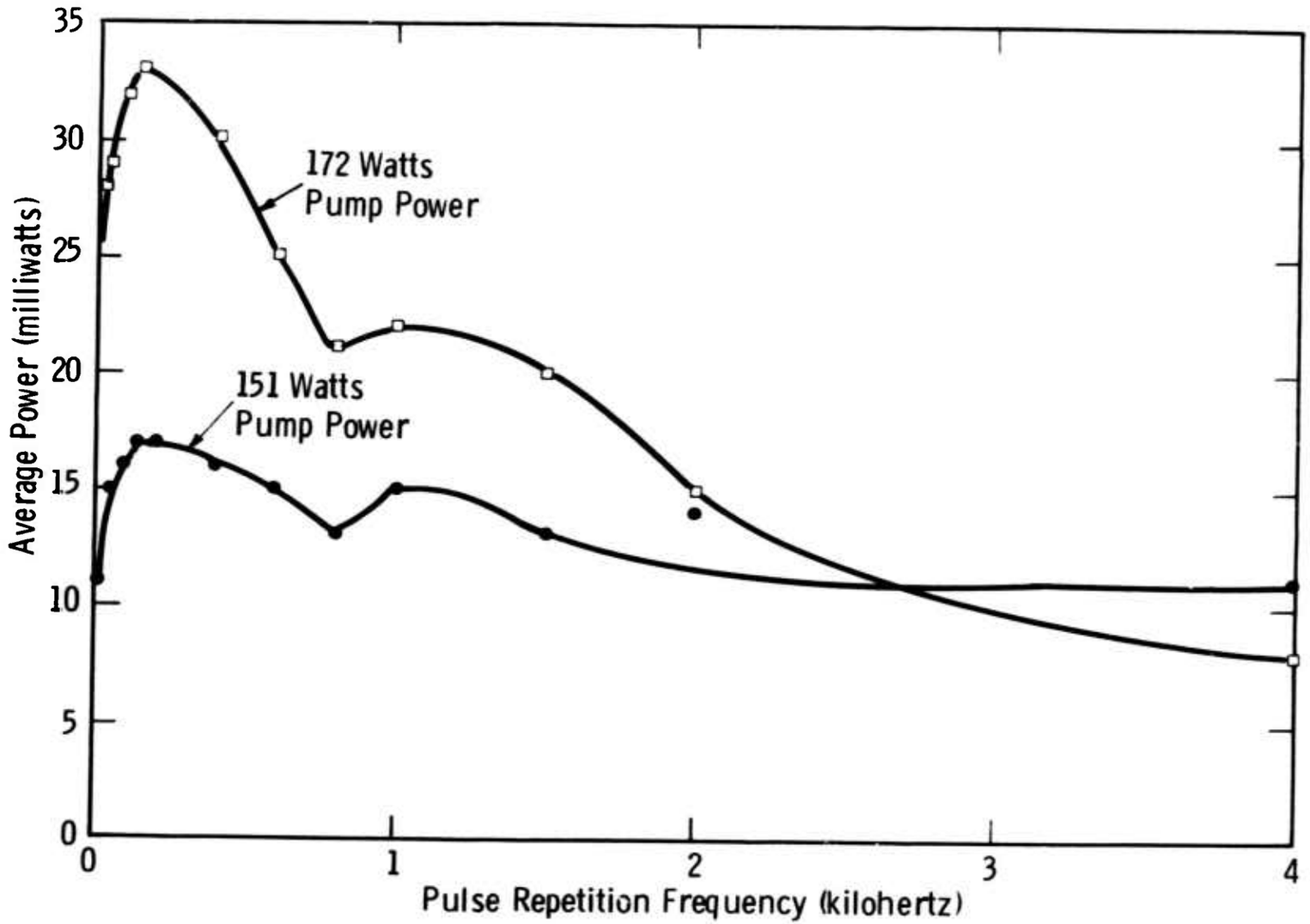

Fig. 39-Average output power vs PRF for a Ho: YAG laser Q-switched acousto-optically by Tl_3AsS_4

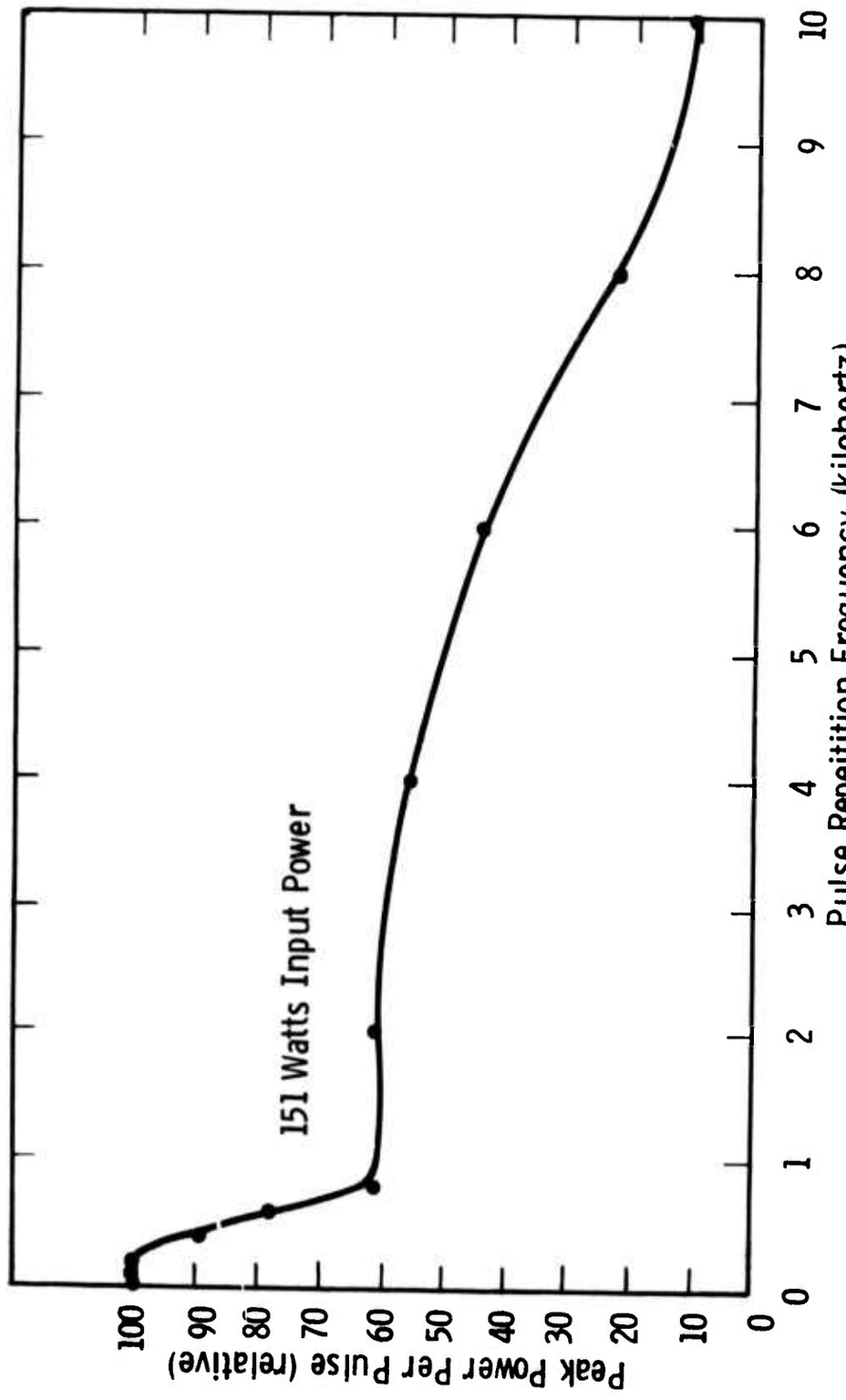

Fig. 40. Peak power per pulse vs PRF for Ho:YAG laser Q-switched acousto-optically by Tl_3AsS_4.

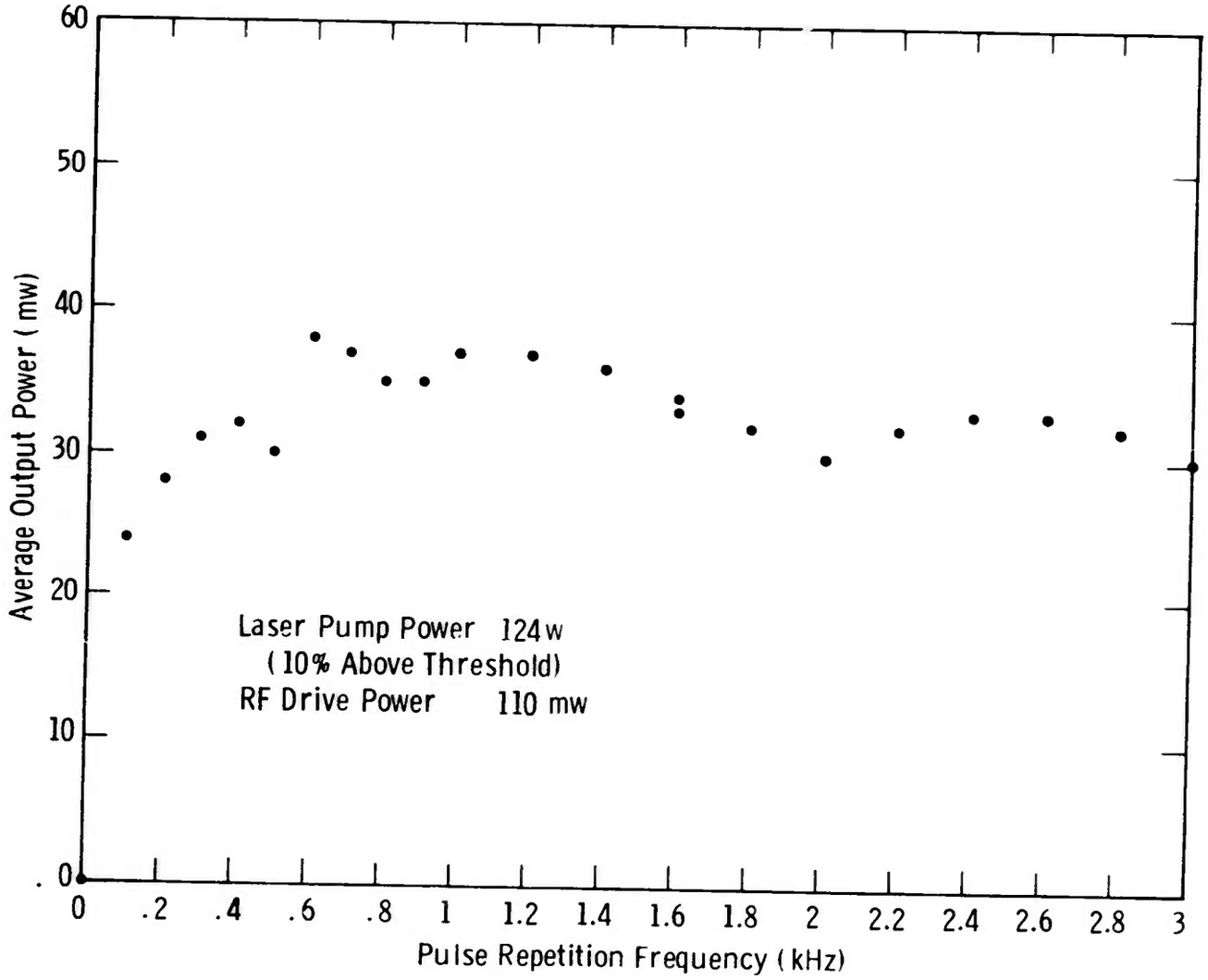

Fig. 41—Average output power vs PRF for Ho: YAG laser acoustooptically Q-switched by Tl_3AsS_4

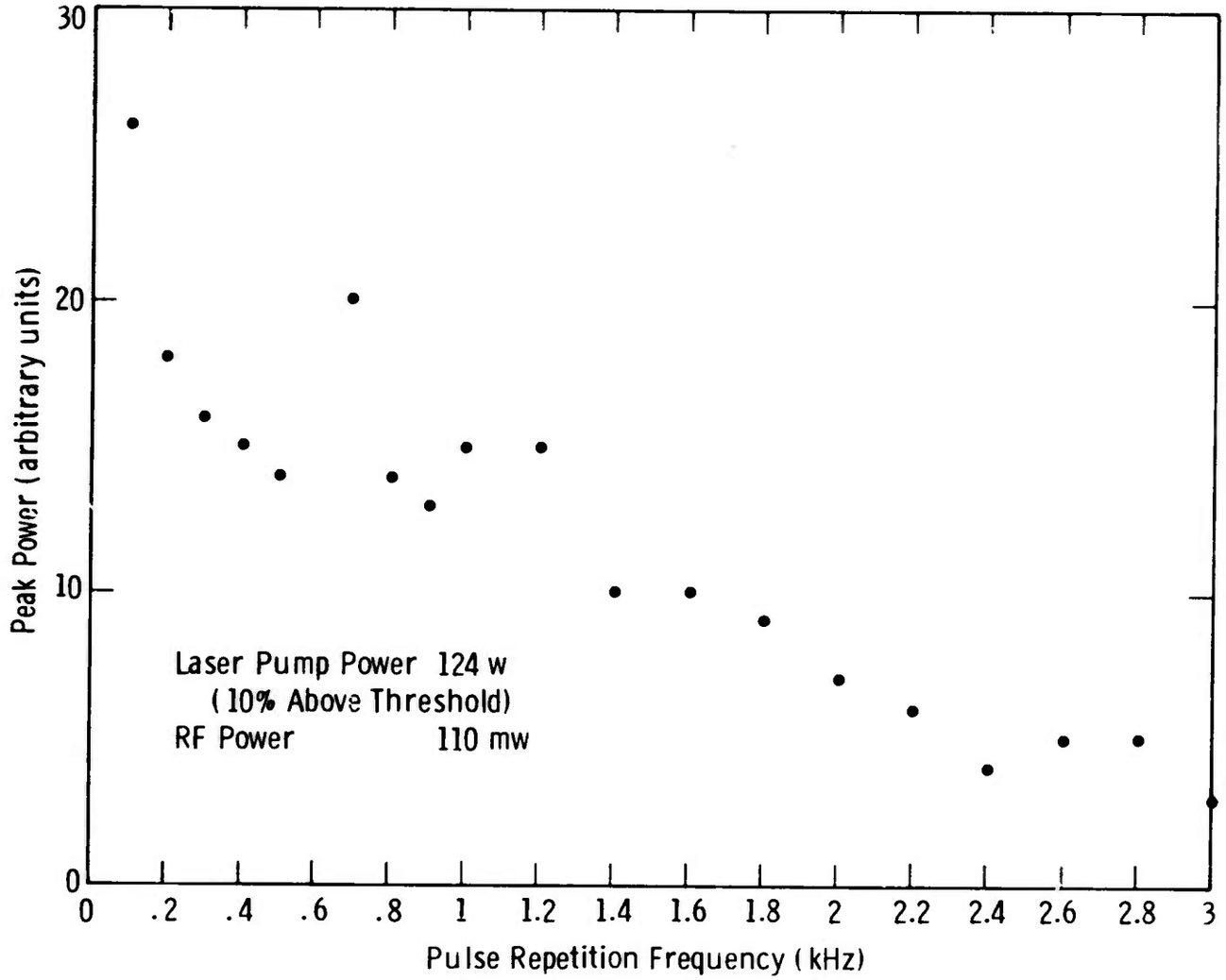

Fig. 42—Pulse peak power vs PRF for Ho: YAG laser acoustooptically Q-switched by Tl_3AsS_4

7.3 Acoustic and Piezoelectric Properties of New Sulfosalt Materials

7.3.1 Tl_3AsSe_3, Tl_3AsS_3

The piezoelectric coupling coefficient k_{15} and elastic constants, measured on the basis of resonant and anti-resonant frequencies of oriented plates of Tl_3AsSe_3, were given in a previous final report.[7] More accurate acoustic velocity measurements were subsequently made, with the results shows below for the appropriate elastic constants.

For longitudinal velocities:

$$C_{33} = \rho V_z^2 = (7.83\ gm/cm^3)(2.18 \times 10^5\ cm/sec)^2 = 3.72 \times 10^{10}\ Nt/M^2$$

$$C_{11} = (7.83)(2.08 \times 10^5)^2\ dyne/cm^2 = 3.39 \times 10^{10}\ Nt/M^2$$

For shear velocities:

$$C_{44} = (7.83\ gm/cm^3)(1.02 \times 10^5\ cm/sec)^2 = 0.815 \times 10^{10}\ Nt/M^2$$

$$C_{66} = 0.815 \times 10^{10}\ Nt/M^2\ .$$

Since Tl_3AsS_3 was not available as oriented single crystals of large enough size, accurate acoustic velocity and oriented plate resonance measurements could not be made. A previously reported measurement on resonance frequency of a unoriented plate implies shear velocities of about 1.2×10^5 cm/sec, or C_{44} and C_{66} elastic constants of about (1×10^{10} Nt/M^2) for Tl_3AsS_3.

7.3.2 Tl_3PS_4, Tl_3PSe_4, Tl_3AsSe_4

No indication of piezoelectric behavior was found in tests on Tl_3PS_4 or Tl_3PSe_4, so if these materials are piezoelectric the effect is very small. Tl_3AsSe_4 was not tested, but it is not likely to be piezoelectric since it appears to be isostructural with Tl_3AsS_4, in which no piezoelectric behavior has been observed.

The results of acoustic velocity measurements on Tl_3AsSe_4 are shown in Table 8 below. The velocities are characteristically low. Of special interest is the very large acoustic birefringence exhibited for the orthogonal shear mode polarizations for propagation in the a and c directions.

TABLE 8. ACOUSTIC VELOCITIES IN Tl_3AsSe_4

Mode	Propagation Direction	Polarization Direction	Velocity (cm/sec)
longitudinal	c	-	2.05×10^5
longitudinal	b	-	2.08×10^5
longitudinal	a	-	2.22×10^5
shear	c	a	6.00×10^4
shear	c	b	1.22×10^5
shear	b	a	1.15×10^5
shear	b	c	1.21×10^5
shear	a	c	6.24×10^4
shear	a	b	1.12×10^5

8. OPTICAL PROPERTIES OF NEW SULFOSALT SINGLE CRYSTAL MATERIALS

8.1 Tl_3PS_4

The optical transmission of Tl_3PS_4 is shown in Fig. 43. Transmission extends from about 0.52 μm to 8.8 μm. The band edge is not as well defined as in other sulfosalt materials, indicating the possibility of residual scattering or absorption loss due to inclusions. The transmission of this sulfosalt compound extends the furthest into the visible of any which we have synthesized so far.

Tl_3PS_4 samples of even better quality have just resulted from the phase diagram studies described in this report. Refractive index measurements will be made when oriented prisms can be prepared, but the results will be obtained too late to be included in this report.

8.2 Tl_3PSe_4

Information of the optical properties of Tl_3PSe_4 and some of the other materials studied in this program has been published recently.[34]

8.3 Tl_3AsSe_4

The optical transmission of Tl_3AsSe_4 is shown in Fig. 44. The transmission range is from 1.15 μm to 17 μm, with two-phonon absorption peaks at 11.6 μm and 12.8 μm.

The refractive indices, measured by the method of normal incidence on oriented prisms of the material, are given in Table 9 below.

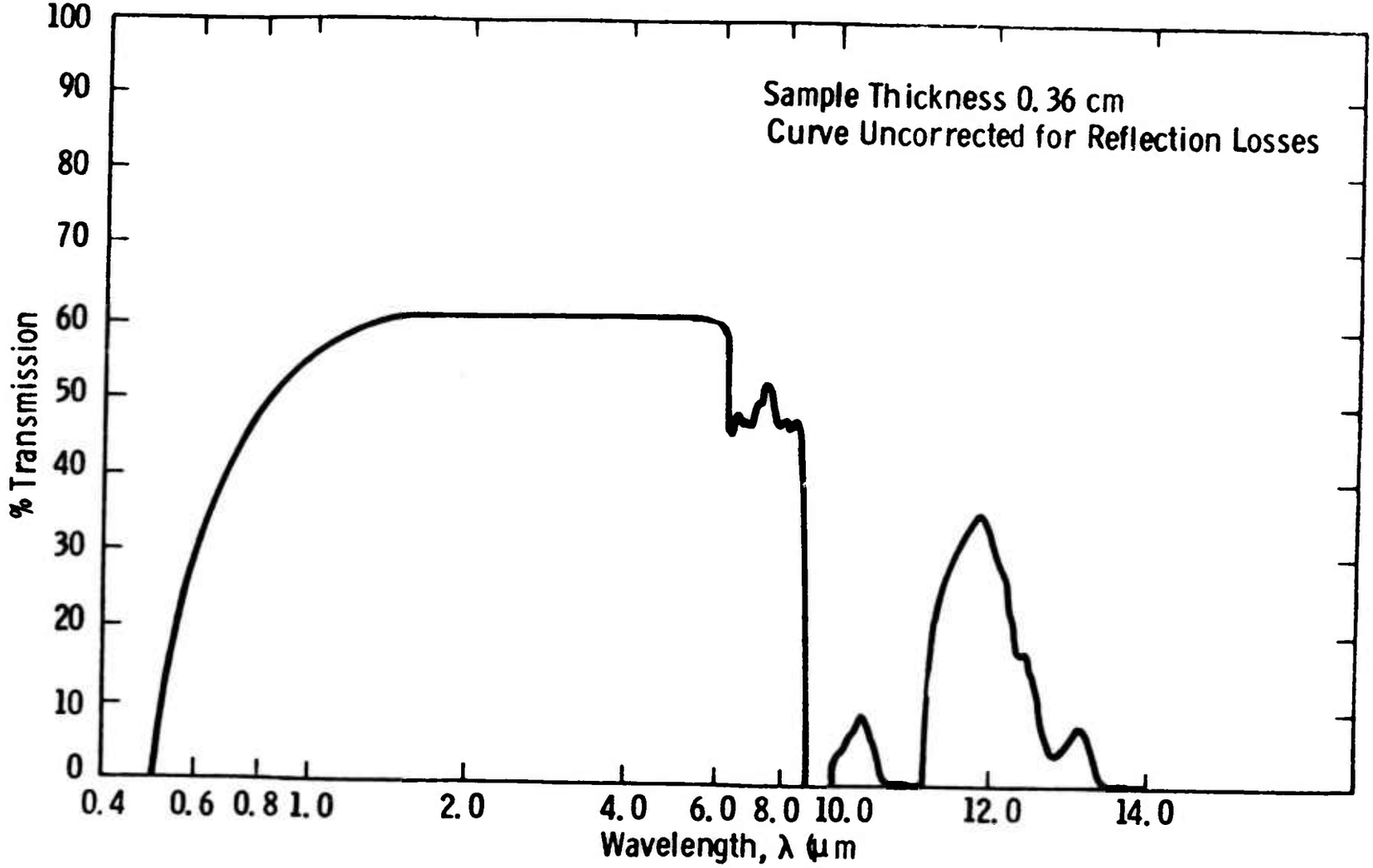

Fig. 43 -- Optical transmission of Tl_3PS_4.

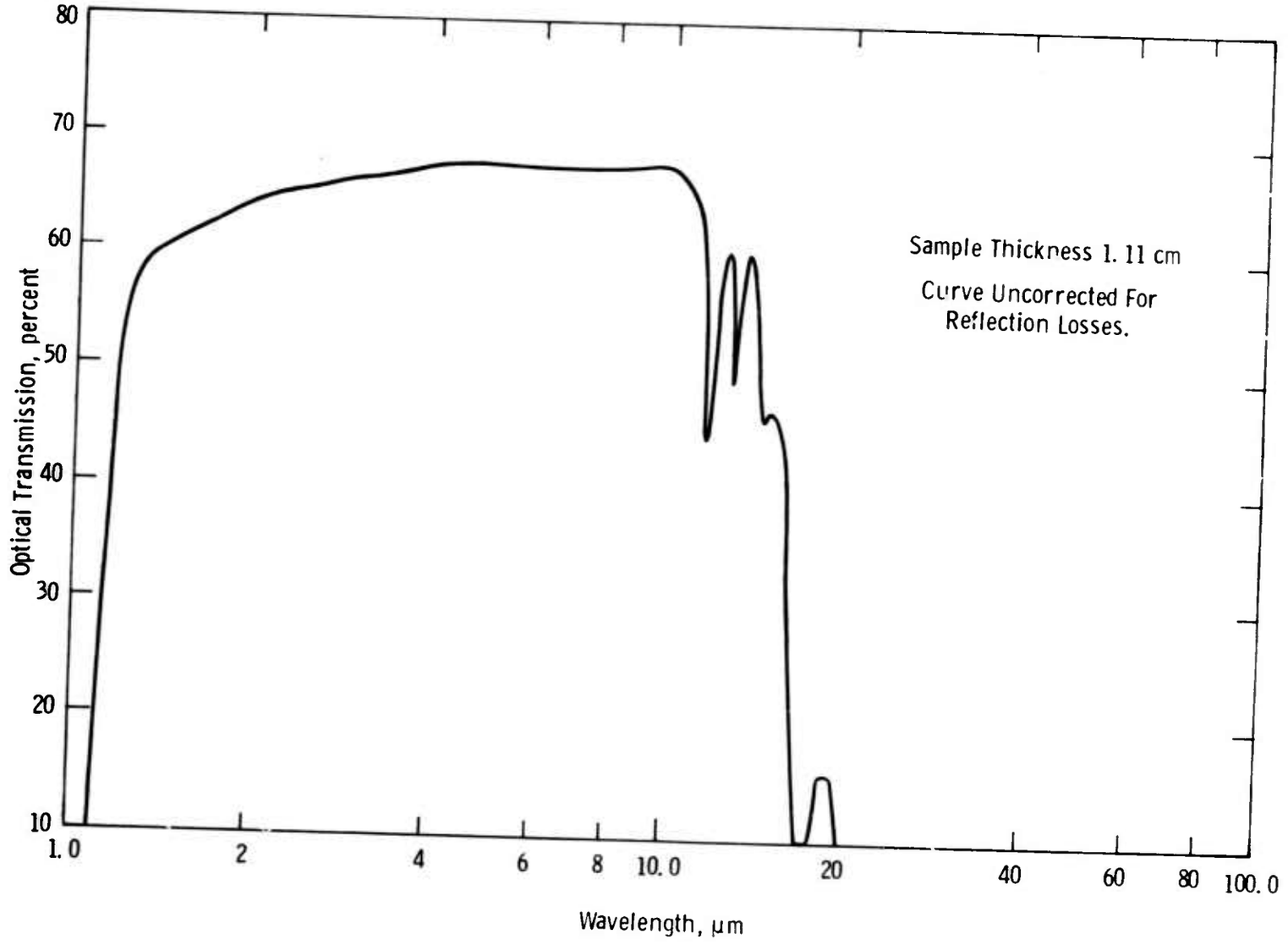

Fig. 44–Optical transmission of Tl_3AsSe_4.

TABLE 9. MEASURED REFRACTIVE INDICES OF Tl_3AsSe_4

Wavelength (μm)	Refractive Index*		
	n_a	n_b	n_c
1.06	3.068	3.151	2.995
1.15	3.029	3.134	2.965
1.553	2.996	3.067	2.949
2.66	2.957	3.033	2.903
3.29	2.947	3.016	2.888
3.365	2.939	3.015	2.888
3.38	2.939	3.016	2.876
4.35	2.939	3.015	2.895
4.44	2.930	2.998	2.876
5.26	2.922	2.998	2.872
5.30	2.922	2.981	2.872

REFERENCES

1. K. F. Hulme, O. Jones, P. H. Davies and M. V. Hobden, Appl. Phys. Lett. 10, 133 (1967).

2. W. Bardsley, P. H. Davies, M. V. Hobden, K. F. Hulme, O. Jones, W. Pomeroy, and J. Warner, Opto-Elect. 1, 29 (1969).

3. W. B. Gandrud, G. D. Boyd, J. H. McFee, and F. H. Wehmeier, Appl. Phys. Lett. 16, 59 (1970).

4. G. W. Roland and R. G. Seidensticker, J. Cryst. Growth 10, 213 (1971).

5. G. W. Roland and J. D. Feichtner, unpubiished work.

6. T. J. Isaacs, M. Gottlieb, and J. D. Feichtner, Appl. Phys. Lett. 24, 107 (1974).

7. G. W. Roland, J. D. Feichtner, and J. P. McHugh, Final Technical Report for ARPA Contract F33615-76-C-1976, AFML-TR-74-6 (1974).

8. G. W. Roland, J. P. McHugh, and J. D. Feichtner, J. Electronic Materials 3, 829 (1974).

9. M. Hansen and K. Anderkc, "Constitution of Binary Alloys," McGraw Hill Book Company, 1305 pp. (1958).

10. R. P. Elliott, "Constitution of Binary Alloys, First Supplement," McGraw Hill Book Company, 877 pp. (1965).

11. F. A. Shunk, "Constitution of Binary Alloys, Second Supplement," McGraw Hill Book Company, New York, 720 pp. (1969).

12. H. Y-P Hong, J. C. Mikkelsen, Jr., and G. W. Roland, Mat. Res. Bull. 9, 365 (1974).

13. G. W. Roland, M. Gottlieb, and J. D. Feichtner, Appl. Phys. Lett. 21, 52 (1972).

14. T. J. Isaacs, M. Gottlieb, and J. D. Feichtner, Appl. Phys. Lett. 24, 107 (1974).

15. S. E. Harris, Proc. IEEE 57, 2096 (1969).

16. R. L. Byer, Stanford Microwave Laboratory Report 2140, January 1973. To be published in "Treatise in Quantum Electronics," H. L. Rabin and C. L. Tang, eds., Academic Press (1973).

17. G. D. Boyd and D. A. Kleinman, J. Appl. Phys. 39, 3597 (1968).

18. J. E. Midwinter and J. Warner, Brit. J. Appl. Phys. 16, 1135 (1965).

19. D. S. Chemla, P. Kupecek, and C. A. Schwartz, Opt. Comm. 7, 225 (1973).

20. J. E. Pearson, U. Ganiel, and A. Yariv, IEEE J. of Quant. Elect., QE-8, 433 (1972).

21. M. V. Hobden, Opto-Electronics 1, 159 (1969).

22. E. R. Nichols, J. C. Corbin, Jr., and V. L. Donlan, Air Force Avionics Laboratory Technical Report AFAL-TR-74-161, July 1974.

23. R. H. Hopkins, N. T. Melamed, T. Henningsen, and G. W. Roland, Technical Report AFAL-TR-71-110 on Contract #F33615-70-C-1051, May 1971.

24. J. Giordmaine and R. C. Miller, in "Physics of Quantum Electronics," Kelley, Lax and Tannenwald, eds., McGraw-Hill, New York, pp. 31-42 (1966).

25. H. Kogelnik and T. Li, Proc. IEEE 54, 1312 (1966).

26. R. W. Dixon, IEEE J. Of Quant. Elect., QE-3, 85 (1967).

27. S. E. Harris and R. W. Wallace, JOSA 59, 744 (1969).

28. S. E. Harris, S. T. K. Nieh, and K. D. Winslow, Appl. Phys. Lett. 15, 325 (1969).

29. S. E. Harris, S. T. K. Nieh, and R. S. Feigelson, Appl. Phys. Lett. 17, 223 (1970).

30. J. A. Kusters, D. A. Wilson, and D. L. Hammond, JOSA 64, 434 (1974).

31. T. M. Smith and A. Korpel, IEEE J. of Quant. Elect., QE-1, 283 (1965).

32. R. W. Dixon and M. G. Cohen, Appl. Phys. Lett. 8, 205 (1966).

33. R. B. Chesler, M. A. Karr, and J. E. Geusic, Proc. IEEE 58, 1899 (1970).

34. M. Gottlieb, T. J. Isaacs, J. D. Feichtner, and G. W. Roland, J. Appl. Phys. 45, 5145 (1974).

APPENDIX I

Paper published in Journal of Electronic Materials 3, 829 (1974).

THE PHASE RELATIONS IN THE SYSTEM Tl_2Se-As_2Se_3 AND THE CRYSTAL GROWTH OF Tl_3AsSe_3*

G.W. Roland, J.P. McHugh and J.D. Feichtner
Westinghouse Research Laboratories
Pittsburgh, Pennsylvania 15235

ABSTRACT

The phase diagram for the system Tl_2Se-As_2Se_3 was studied by quenching and thermal analysis experiments, with emphasis on the composition range 15-35 mol % As_2Se_3, so as to determine the melting relations of Tl_3AsSe_3, a useful compound for optical and acousto-optical devices. Tl_3AsSe_3 melts congruently at 311 $\pm$ 2°C, and the only other pseudobinary compound, $TlAsSe_2$, melts congruently at 272 $\pm$ 2°C. Eutectics lie between Tl_2Se and Tl_3AsSe_3 ($\sim$ 21 mol %, 302 $\pm$ 2°C) between Tl_3AsSe_3 and $TlAsSe_2$ ($\sim$ 32 mol %, 238 $\pm$ 3°C), and between $TlAsSe_2$ and As_2Se_3 ($\sim$ 72 mol % As_2Se_3, 249 $\pm$ 3°C). The maximum-melting Tl_3AsSe_3 composition lies at 24.62 $\pm$ 0.13 mol % As_2Se_3. Crystals of Tl_3AsSe_3 were grown from three pseudobinary compositions with the best crystals obtained from melts containing 24.625 mol % As_2Se_3.

---

*This research was sponsored by the Advanced Research Projects Agency of the Department of Defense and was monitored by the Air Force Materials Laboratory, LP, under Contract No. F33615-72-C-1976.

INTRODUCTION

Sulfide-type or chalcogenide compounds have received considerable attention for nonlinear optical applications such as harmonic generation and up-conversion in the infrared wavelength region.[1-11] Furthermore, many are characterized by high refractive indices and low acoustic velocities and are thus useful for acousto-optical modulation and deflection[12,13] and, depending on their symmetry class, in acousto-optic filters.[14,15] In a survey of sulfide-type compounds for such applications, we identified Tl_3AsSe_3 as a useful material and reported its optical and nonlinear optical properties.[16] It is acentric with space group R3m, has the expected wide transmission range (1.23 - 18 μm), high refractive indices (indicating a large figure of merit for nonlinear applications), and the birefringence is such as to allow phase matching for second-harmonic generation at 10.6 μm. It should be useful as a parametric oscillator pumped from 1.25 to beyond 10 μm, and especially so for a 2 μm-pumped oscillator operating with outputs in the 3-5 μm region. In addition, the acousto-optic figure of merit at λ = 3.39 μm, measured by direct comparison to fused silica, is 955,[17] about twice as large as the figure of merit for Ge, the material presently used in acousto-optic devices in the infrared region of the spectrum.

The present study of phase relations in the system Tl_2Se-As_2Se_3 was undertaken primarily to understand the melting relations of Tl_3AsSe_3 (3 $Tl_2Se \cdot As_2Se_3$) so as to optimize Tl_3AsSe_3 crystal growth for device applications. In addition, we wis'ed to see whether there were any other pseudobinary compounds of practical interest for devices. Our most detailed experimentation was therefore conducted in the composition range around Tl_3AsSe_3, 15-35 mol % As_2Se_3, but sufficient additional experiments were done along the Tl_2Se-As_2Se_3 join to determine the stable phases and establish their general melting relations.

In this paper we describe our phase diagram study, compare our data to data in the literature, and discuss the crystal growth and optical quality of Tl_3AsSe_3 crystals.

PREVIOUS DATA FOR THE PHASE RELATIONS

The only previous systematic study of the Tl_2Se-As_2Se_3 phase diagram known to us was reported by Dembovskii, Kirilenko and Khvorostenko,[18] who studied the system primarily by differential thermal analysis. They found that there is significant solid solution of Tl_2Se and As_2Se_3 along the pseudobinary join, both Tl_2Se solid solution and As_2Se_3 solid solution extending about 10 mol % toward the opposite end-component. Two pseudobinary compounds were observed, Tl_3AsSe_3 (25 mol % As_2Se_3) and $TlAsSe_2$ (50 mol % As_2Se_3). They reported the compound Tl_3AsSe_3 melted incongruently to Tl_2Se (solid solution) + liquid (L) at 280°C; $TlAsSe_2$ was found to melt congruently at 265°C. Eutectics between Tl_3AsSe_3 and $TlAsSe_2$ were observed at 210°C and 60 mol % Tl_2Se, and between $TlAsSe_2$ and As_2Se_3 at 235°C and 28 mol % Tl_2Se. The x-ray powder data for Tl_3AsSe_3 are sufficiently similar to the data that we reported[16] that there is no doubt that the two phases are the same, although our phase diagram as concerns the melting relations of Tl_3AsSe_3 differs considerably.

EXPERIMENTAL METHODS

Two techniques were used for phase diagram study: 1) quench-type and 2) thermal analysis experiments. Both were conducted in sealed, initially-evacuated silica glass containers using elemental Tl, As and Se (ASARCO > 99.999 wt % pure) or presynthesized compounds as reactants. The Tl was boiled in deionized water and the As heated in the reducing portion of a Bunsen burner flame to remove oxide coatings.

For quench-type experiments, reactant materials (typically 100-200 mg total weight) were carefully weighed in desired proportions, sealed in the silica tubes, heated for desired lengths of time and chilled to room temperature in ice water. For melting point determinations, a portion of presynthesized compound (e.g. Tl_3AsSe_3), or a mixture of compounds (e.g. $Tl_2Se + Tl_3AsSe_3$) was heated at successively higher temperatures until melting occurred. Liquids were clearly visible through the glass walls of the sample tubes.

The experimental system used for thermal analysis consisted of a vertical furnace, a temperature control system and a Leeds and Northrup AZAR strip chart recorder which produced a direct plot of sample temperature as a function of time (cooling curve). The temperatures involved in this system are sufficiently low so that satisfactory

cooling rates (1 to 1.5°C/min) were obtained by simply turning off the furnace and letting it cool at its natural rate. The quartz sample containers included a thermocouple well which permitted the chromel-alumel thermocouple bead to be positioned so that it was surrounded by the sample, but isolated from it. A typical run proceeded as follows. The sample tube was prepared, loaded with the reactants, sealed, and the temperature raised over a period of several hours to 750°C to 800°C. The tube was shaken several times, heated at the high temperature overnight to ensure homogenization, and cooled to room temperature in the furnace. The thermocouple was positioned in the thermocouple well, the charge reheated to a temperature at least 50°C above the estimated liquidus temperature, and then allowed to cool while the temperature was recorded. Samples were usually heated and cooled with continuous temperature monitoring several times to verify the temperature and shape of thermal arrests.

Crystals were grown using the Stockbarger technique as previously reported.[16] The band edge of Tl_3AsSe_3 is in the near infrared and it was therefore impossible to inspect or measure the optical quality of single crystals using visible radiation. A scanning technique for profiling the optical loss in single sulfosalt crystals was therefore set up, as shown in Fig.A1. An infrared laser beam is incident onto a Tl_3AsSe_3 boule on which plane parallel inspection faces have been ground and polished. The power transmitted through the beam, and the total optical loss, is thus characterized as a function

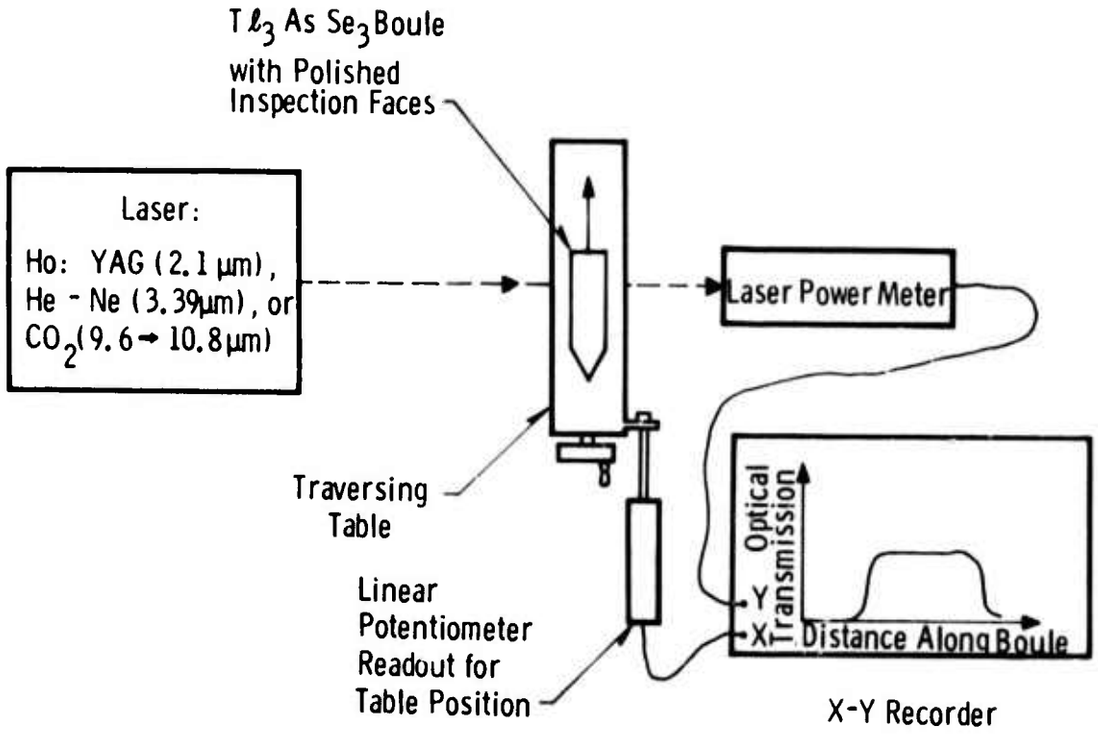

Fig.A1 -- Schematic diagram of optical scanning system for Tl_3AsSe_3 crystals.

of crystal position. It should be noted that this measurement technique gives only the total loss through the crystal. To account accurately for reflection losses, the crystal refractive indices and its orientation relative to the polarization of the incident beam must be aken into account. In addition, low-angle scattering losses are not accounted for, because the power meter acceptance solid angle is relatively large, about 2×10^{-3} steradians. Nevertheless, the system was very useful for routine crystal examination and evaluation, particularly for determining the best section of a boule.

PHASE RELATIONS

Melting Relations of Tl_3AsSe_3

The results of our thermal analysis experiments conducted to determine Tl_3AsSe_3 melting relations (Fig.A2) show that Tl_3AsSe_3 melts congruently at 311 $\pm$ 2°C, rather than incongruently at lower temperature as reported by Dembovskii *et al.*[18] The discord is surprising, especially in view of the general correspondence between the other features of their diagram and that which we have determined. Additional support for our interpretation of the thermal data is provided, however, by quench experiments and crystal growth runs. We cannot detect any melting when pieces of Tl_3AsSe_3 are heated below 311° in sealed tubes, although liquids are usually clearly visible through the tube walls. Thus, we cannot verify the existence of a Tl_2Se + L phase field between 280° and 311°C at Tl_3AsSe_3 composition. In addition, quenched charges of Tl_3AsSe_3 liquid appear to be essentially homogeneous Tl_3AsSe_3 when polished surfaces are examined by microscope. Incongruently-melting compounds are usually evidenced by polyphase products when liquids are quenched. If Tl_3AsSe_3 melted incongruently, then slowly-cooled melts such as we use for crystal growth should initially crystallize to Tl_2Se, i.e., large single crystals of Tl_3AsSe_3 would be an unlikely

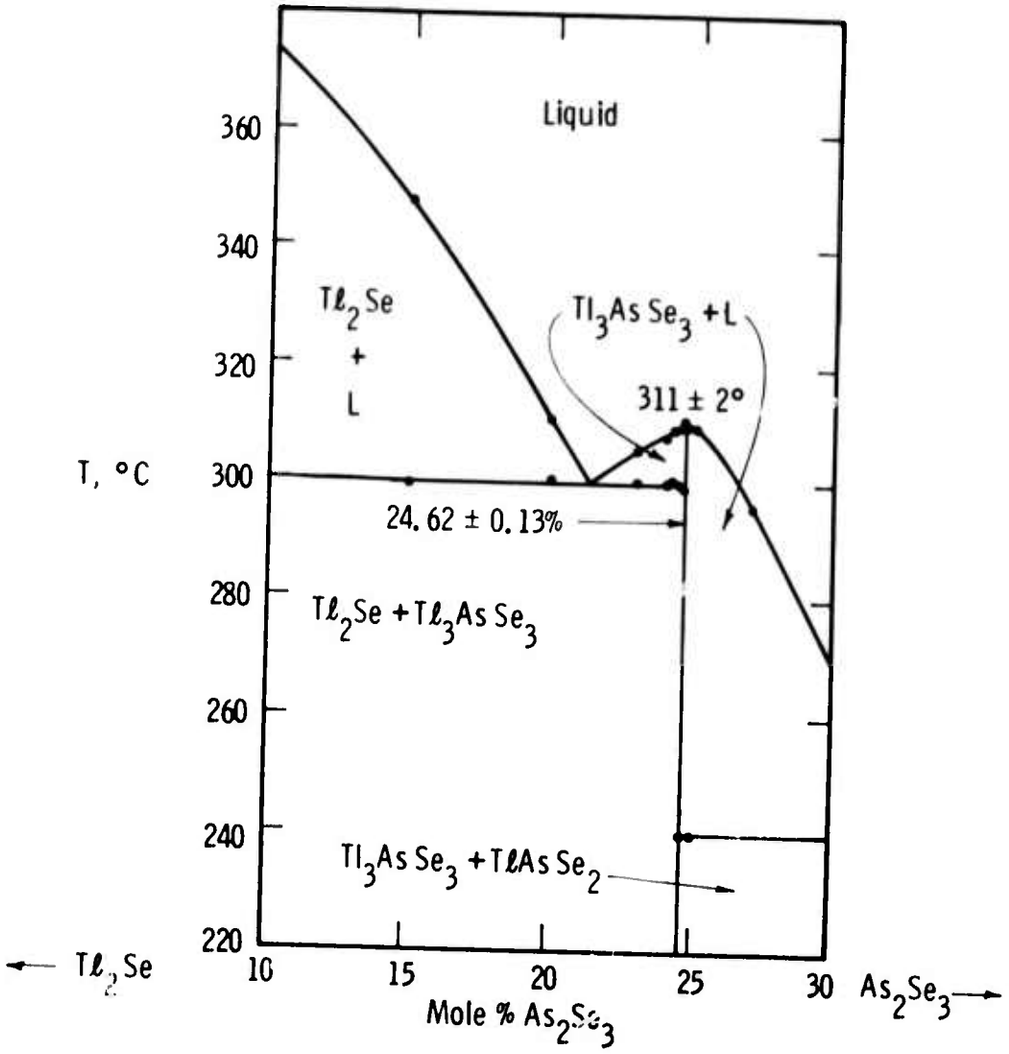

Fig.A2 -- Partial phase diagram for the Tl_2Se-As_2Se_3 system. The points represent thermal arrests. A vapor phase is present with all assemblages.

product. This is contrary to our finding that large single crystals of Tl_3AsSe_3 can easily be grown from the melt. We therefore believe that the weight of evidence supports our contention that Tl_3AsSe_3 melts congruently.

We have also deduced from the thermal data that the maximum melting Tl_3AsSe_3 composition does not lie at the stoichiometric composition, but at a point slightly toward Tl_2Se from ideal, at 24.62 ± 0.13 mol % As_2Se_3. Freezing temperatures obtained from cooling curves were not sufficient in themselves to locate the maximum-melting composition with precision; instead, it was the presence or absence of eutectic arrests at 300°C and 240°C which permitted the maximum to be defined with more precision than the freezing temperatures taken alone. Runs at 24.75 and 25.00 mol % As_2Se_3 showed arrests at 238 ± 3°C for the eutectic between Tl_3AsSe_3 and $TlAsSe_2$ indicating that they lie to the As_2Se_3 side of maximum melting. A 24.5 mol % As_2Se_3 run showed only the eutectic at 302 ± 2°C, indicating that this composition lies to the Tl_2Se-rich side of the maximum, i.e., the maximum-melting Tl_3AsSe_3 composition lies between 24.50 and 24.75 mol % As_2Se_3. We have not determined whether this compound is non-stoichiometric at all temperatures, or whether it attains stoichiometry at low temperature, as is the case for many sulfide-type compounds. Clearly, the maximum-melting composition is not described by the formula Tl_3AsSe_3, but we opt to continue to use that formula until more data on the compositional variation become available.

The Tl_2Se-As_2Se_3 Pseudobinary Diagram

Our pseudobinary phase diagram, based on both thermal and quenching experiments, is shown in Fig.A3. The general form of the diagram, other than the melting relations of Tl_3AsSe_3, is the same as that reported by Dembovskii *et al.*, except that our melting temperatures are somewhat higher. The only pseudobinary compound at liquidus temperatures, in addition to Tl_3AsSe_3, is $TlAsSe_2$. Liquids of $TlAsSe_2$ composition quench as glasses which crystallize when annealed below the melting point (the crystallization time can vary between a few hours and a few days, depending on how finely the glass is crushed). The x-ray powder data indicate a low symmetry structure, not surprising since the sulfur analog $TlAsS_2$, lorandite, is monoclinic. Because of the low symmetry, we did not pursue $TlAsSe_2$ crystal growth for optical uses. Eutectics at 238 $\pm$ 3° and 249 $\pm$ 3° separate $TlAsSe_2$ from Tl_3AsSe_3 and As_2Se_3 respectively. Because our interests primarily concerned the pseudobinary compounds, we did not redetermine the solid-solution limits of Tl_2Se and As_2Se_3; the limits in Fig.A3 are taken from Dembovskii *et al.*

Long-term annealing experiments (1-2 months) were conducted at 150° and 200°C to see whether there were any additional intermediate phases in this system. To aid the attainment of equilibrium, reactant material was either melted prior to use, or consisted of previously-synthesized compounds which were pressed into pellets. The only products identified by x-ray diffraction were Tl_2Se, Tl_3AsSe_3, $TlAsSe_2$ and As_2Se_3.

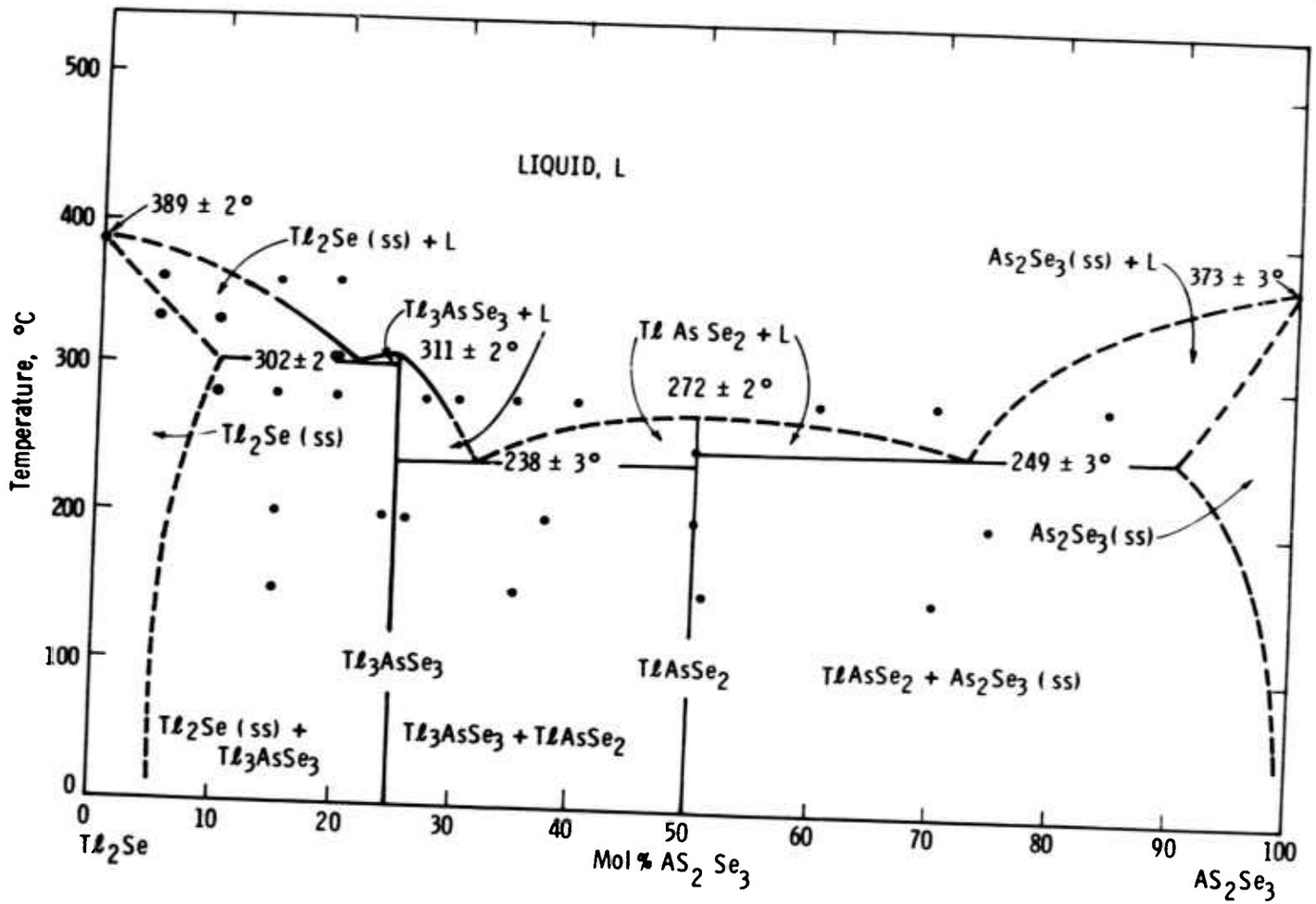

Fig. 3—Pseudobinary phase diagram for the system Tl_2Se-AS_2Se_3. The points represent quenching experiments. All assemblages contain a vapor phase.

CRYSTAL GROWTH

Crystals of Tl_3AsSe_3 were grown at three compositions to determine the optimum growth composition: 1) stoichiometric Tl_3AsSe_3, which contains 25 mol % As_2Se_3; 2) a composition $(Tl_2Se)_{0.75375} \cdot (As_2Se_3)_{0.24625}$; and 3) a composition $(Tl_2Se)_{0.7525}(As_2Se_3)_{0.2475}$. The latter two compositions lie on the Tl_2Se-As_2Se_3 composition join but slightly more Tl_2Se-rich than stoichiometric Tl_3AsSe_3; composition 2) corresponds about to the maximum-melting composition as determined by the phase-diagram study. Seven crystal-growth experiments are described in Table A1.

The crystals were examined using the scanning technique. With the total optical losses approaching only a few percent, it was very difficult to obtain accurate measurements of losses and to compare effects of stoichiometry and growth rate on crystal quality. The results indicate that generally satisfactory crystals can be grown from all three of the compositions cited above, but also that $x = 0.75375$ to 0.7525 (24.75 - 24.625 mol % As_2Se_3) and a growth rate of the order of 15 mm/day are optimum growth conditions for high quality Tl_3AsSe_3, as is to be expected from the position of the maximum-melting Tl_3AsSe_3 composition. This is dramatically illustrated by a comparison of crystals TASE-BR-3 and TASE-BR-6 (Figs. A4a and A4b).

TABLE A1

Optical Loss Measurements on Tl_3AsSe_3 Boules

Boule No.	Composition $(Tl_2Se)_x(As_2Se_3)_{1-x}$	Growth Rate (mm/day)	Length of Best Section (cm)	Optical Loss in Best Section (cm^{-1})
BR-1	(0.75375)(0.24625)	12.2	1.2	0.05 → 0.08
BR-2	(0.75250)(0.24750)	10.5	0.8	0.05 → 0.08
BR-3	(0.75375)(0.24625)	15.3	1.6	$\tilde{<}$ 0.01
BR-4	(0.75250)(0.24750)	15.0	1.0	0.02 → 0.04
BR-5	(0.75375)(0.24625)	15.8	2.2	0.03 → 0.06
BR-6	(0.75000)(0.25000)	15.0	2.2	0.03 → 0.06
BR-8	(0.75375)(0.24625)	15.4	1.2	0.02 → 0.04

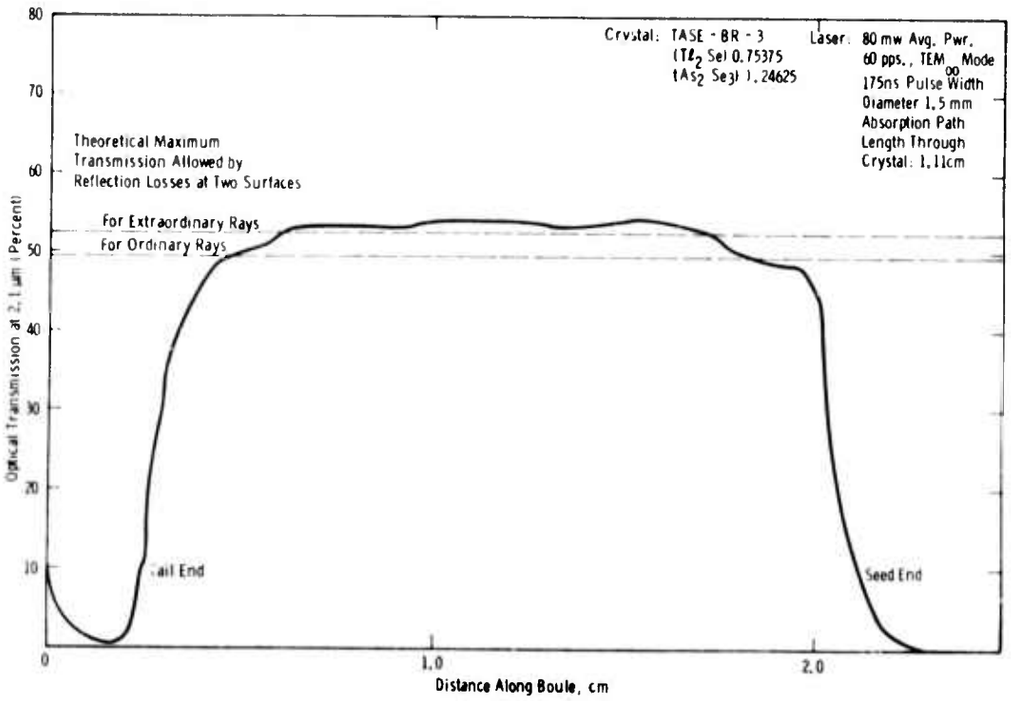

Fig.A4a -- Optical transmission at 2.1 μm along an as-grown boule of Tl_3AsSe_3, Crystal TASE-BR-3.

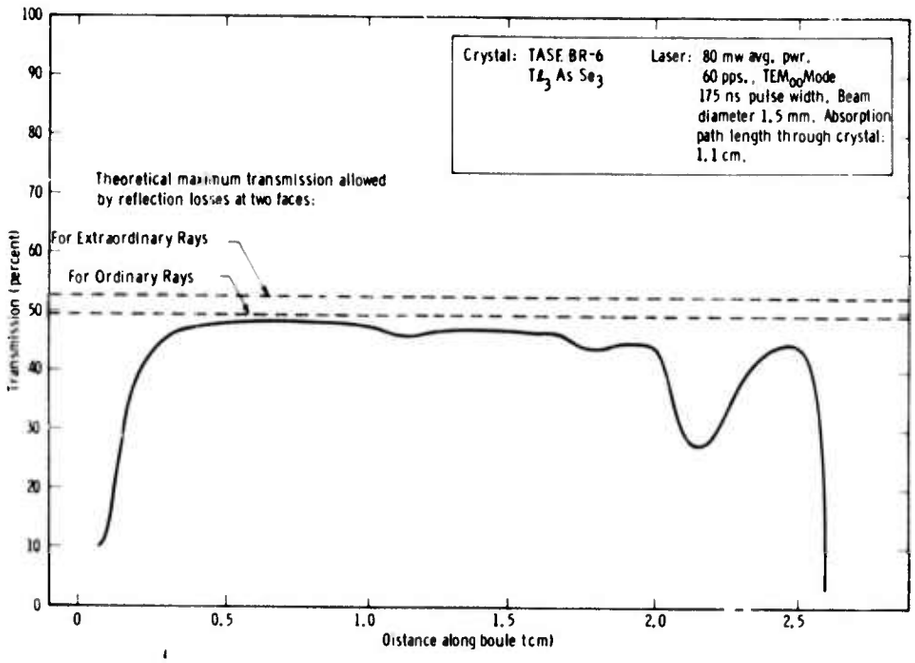

Fig.A4b -- Optical transmission at 2.1 μm along an as-grown boule of Tl_3AsSe_3 (Crystal TASE-BR-6).

Crystal TASE-BR-3 was grown from the maximum-melting composition; it exhibits large clear regions with bulk losses of nearly zero, at least within the accuracy of our measurement technique. The transmission of BR-3 actually appears to exceed the theoretical maximum by a small amount; this is probably due to a slow fluctuation in the probe laser average power, which is continually monitored but fluctuates by about $\pm$ 2%. The actual losses in BR-3 appear to be approaching 0.01 cm^{-1} or less.

Crystals grown from stoichiometric Tl_3AsSe_3 melts (e.g. TASE-BR-6), on the other hand, have optical transmissions that do not attain theoretical maximum values (Fig.A4b). Often such crystals have variable transmission along the length of the crystal and are also prone to have high-absorption bands, probably impurity bands. The differences are striking considering that only a few tenths of a mol % change in melt composition is involved, but not surprising since two pseudobinary eutectics lie in close proximity to Tl_3AsSe_3 at about 21 mol % and at about 31 mol % As_2Se_3. Thus, off-composition melts will reach the eutectic compositions relatively quickly, at which point particles of second phase will be included and/or single-crystal growth will cease. These results clearly emphasize the need for phase diagram data when growing ternary crystals such as Tl_3AsSe_3 for optical applications when especially high optical quality is desired.

SUMMARY

The phase diagram determined here for the Tl_2Se-As_2Se_3 system shows that Tl_3AsSe_3 melts congruently at 311° ± 2°C and is amenable to crystal growth by the Stockbarger technique. The best crystals are obtained from melts having compositions of 24.62 ± 0.13 mol % As_2Se_3, the composition of the maximum melting point of Tl_3AsSe_3. The only other compound, $TlAsSe_2$, melts congruently at 272° ± 2°C. Crystals having good optical quality can be grown from pseudobinary compositions between 24.50 and 25.00 mol % As_2Se_3, although the best crystals obtained so far were grown from melts having 24.625 mol % As_2Se_3 composition, i.e., the maximum melting composition.

ACKNOWLEDGMENTS

We thank P. Piotrowski and R. P. Storrick for their assistance in the phase diagram study and crystal growth, and A. Mego for his assistance in the optical measurements.

REFERENCES

1. K. F. Hulme, O. Jones, P. H. Davies, and M. V. Hobden, "Synthetic Proustite (Ag_3AsS_3): A New Crystal for Optical Mixing," Appl. Phys. Lett. 10, 133 (1967).
2. W. Bardsley and O. Jones, "On the Crystal Growth o Optical Quality Proustite and Pyrargyrite," J. of Crystal Growth 3/4, 268 (1968).
3. A. L. Gentile and O. M. Stafsudd, "Czochralski-Grown Proustite and Related Compounds," J. Crystal Growth 3,4, 272 (1968).
4. F. H. Wehmeier, R. A. Laudise, and J. W. Schiever, "The System Ag_2S-As_2S_3 and the Growth of Crystals of Proustite, Smithite, and Pyrargyrite," Mat. Res. Bull. 3, 767 (1968).
5. P. H. Davies, M. V. Hobden, K. F. Hulme, O. Jones, W. Pomeroy and F. Warner, "Synthetic Proustite (Ag_3AsS_3): Nonlinear Optical Properties and Upconversion of Infrared," Paper 22-J-2, International Quantum Electronics Conference, Miami, May 14-17 (1968).
6. A. L. Gentile and O. M. Stafsudd, "Melt Growth of Ternary Chalcogenides," Mat. Res. Bull. 4, 869 (1969).
7. J. Warner, "Photomultiplier Detection of 10.6 Micron Radiation Using Optical Up-Conversion in Proustite," Appl. Phys. Lett. 12, 222 (1968).
8. D. Boggett and A. F. Gibson, "Second Harmonic Generation in Proustite," Phys. Lett. 28A, 33 (1968).

9. W. B. Gandrud and G. D. Boyd, "Photomultiplier Detection of 10.6 μ Radiation Using CW Sum-Mixing in Ag_3SbS_3," Optics Communications 1, 187 (1969).

10. W. B. Gandrud, G. D. Boyd, J. H. McFee and F. H. Wehmeier, "Nonlinear Optical Properties of Ag_3SbS_3," Appl. Phys. Lett. 16, 59 (1970).

11. E. O. Ammann and J. M. Yarborough, "Optical Parametric Oscillation in Proustite," Appl. Phys. Lett. 17, 233 (1970).

12. G. W. Roland, M. Gottlieb and J. D. Feichtner, Properties of Thallium Arsenic Sulphide, Tl_3AsS_4," Appl. Phys. Lett. 21, 52 (1972).

13. T. J. Isaacs, M. Gottlieb and J. D. Feichtner, Properties of Thallium Phosphorous Selenide, Tl_3PSe_4," in press Appl. Phys. Lett. (Feb. 1974).

14. S. E. Harris and R. W. Wallace, "Acousto-Optic Tunable Filter," J. Opt. Soc. Am. 59, 744 (1969).

15. S. E. Harris, S. T. K. Nieh, and D. K. Winslow, "Electronically Tunable Acousto-Optic Filter," Appl. Phys. Lett. 15, 325 (1969).

16. J. D. Feichtner and G. W. Roland, "Optical Properties of a New Nonlinear Optical Material: Tl_3AsSe_3," Appl. Optics 11, 993 (1972).

17. M. Gottlieb and J. D. Feichtner, unpublished data.

18. S. A. Dembovskii, V. V. Kirilenko and A. S. Khvorostenko, "The As_2Se_3-Tl_2Se System," Russian Journal of Inorganic Chemistry 14, 1346 (1969).

☆ U. S. GOVERNMENT PRINTING OFFICE: 1976 — 657-630/498